Doctoral Thesis

Analytic and numerical study of interactions between charged particles and electromagnetic waves in the classical regime

Teyoun Kang

Department of Physics

Graduate School of UNIST

2019

Analytic and numerical study of interactions
between charged particles and electromagnetic waves
in the classical regime

Teyoun Kang

Department of Physics

Graduate School of UNIST

Analytic and numerical study of interactions between charged particles and electromagnetic waves in the classical regime

A thesis/dissertation
submitted to the Graduate School of UNIST
in partial fulfillment of the
requirements for the degree of
Doctor of Philosophy

Teyoun Kang

6. 19. 2019.
Approved by

_____

Advisor
Min Sup Hur

Analytic and numerical study of interactions between charged particles and electromagnetic waves in the classical regime

Teyoun Kang

This certifies that the thesis/dissertation of Teyoun Kang is approved.

6. 19. 2019.

signature

_____

Advisor: Min Sup Hur

signature

_____

Kyujin Kwak

signature

_____

Moses Chung

signature

_____

Kitae Lee

signature

_____

Chul Min Kim

Abstract

Although the Maxwell equation and Lorentz force is classical, still many phenomena of several areas can be explained just by solving the two equations. As the general solution for the both equation has not been obtained yet, particular and numerical solutions are being used as the only tools to analyze physical data. A particular solution might explain a specific phenomenon only, but the solution makes it understandable completely. On the other hand, a numerical solution is not only opposite, but also dependent on computer resources. Since the computational technologies were developed rapidly, now the both solution have equal importance and complement each other. In this thesis, I suggest some useful skills to derive the particular and numerical solutions for several interesting interactions between charged particles and electromagnetic waves: microwave reflectometry, radiation pressure acceleration, and radiation reaction. Moreover, how the both solution can interpret those interactions and complement each other's lack of theories will be presented. At last, some mathematical and physical discoveries are written with their derivation.

Contents

List of Figures

I Introduction

The classical electrodynamics (CED) is a theory model which takes account of Maxwell equation and Lorentz force as its axioms. Even though an half century has passed since the quantum electrodynamics (QED) was published, still CED is preferentially applied to analyze experimental data of several physics areas such as plasma physics, astrophysics, and optical physics. It is because CED is not only easy to utilize, but also remarkably compatible with macroscopic phenomena. Accordingly, most of theoretical studies for those areas eventually become equivalent to solving both Maxwell equation and Lorentz force.

An interesting point is that over a century the general solution of the both equation has never been obtained since they were developed, and there are several reasons for this. Basically, Maxwell equation requires continuous charge distributions (ρ, $\mathbf{J}$), while Lorentz force only provides motions of point-charges ($\mathbf{r}$, $\mathbf{v}$). This information gap makes solving the both equation extremely difficult, because a continuous distribution cannot be induced from discretized distributions of point particles. It could be easily verified by a Dirac-delta function which describes a point-particle's density, whose linear combination never yields a continuous one. In fact, to solve this problem, Vlasov has suggested an equation which modifies Liouvile's and Boltzmann's equations;

$$\frac{\partial f}{\partial t} + \boldsymbol{\nabla} \cdot (f\mathbf{v}) + \boldsymbol{\nabla}_v \cdot (f\mathbf{a}) \;\; = \;\; 0. \tag{1}$$

At least so far, it has been the best equation to describe the distribution of point-particles continuously, but it is still insufficient to explain some well-known phenomena such as particle collision and ionization. Moreover, even if those phenomena are negligible, Vlasov equation itself is almost impossible to solve as the function $f(\mathbf{r}, \mathbf{v}, t)$ is defined in the six-dimensional space. Hence, for now, particular and numerical solutions of both Maxwell's and Vlasov's equations would be the only appropriate tools to analyze the experiment data theoretically. Therefore, as the each solution has completely different advantages, present theoretical physicists are required to be capable of dealing with the both solution. Unfortunately, however, the mathematical skills to calculate the both are so incompatible, and it makes the requirement very unreachable.

Normally, the particular solutions in CED are obtained by Eulerian and Lagrangian descriptions. Eulerian description usually assumes Vlasov equation to be Euler equation, which changes the distribution function $f(\mathbf{r}, \mathbf{v}, t)$ to the density function $n(\mathbf{r}, t)$ in three-dimensional space;

$$\frac{\partial \mathbf{p}}{\partial t} + (\mathbf{v} \cdot \boldsymbol{\nabla})\, \mathbf{p} \;\; = \;\; \mathbf{F} - \frac{\boldsymbol{\nabla} P}{n}. \tag{2}$$

The solutions of this equation very well explain a lot of motions that particles represent, except for kinetically dominant motions. Meanwhile, a motion of one particle obtained by Lorentz force is sometimes applied to interpret the kinetic effect, and this approach is called Lagrangian description. Historically, the both description always requires understanding the *analysis* deeply.

On the other hand, in case of deriving the numerical solution, the main issue is which finite differential method (FDM) would be appropriate for assuming Maxwell's and Vlasov's equations. Of course there are many well-established (and stable) methods indeed, but it does not mean that they are the best always. The best FDM might be changed depending on physical problems or computer resources that researchers have. Furthermore, as each methods lead to each different types of numerical errors, the ways to verify the validity of numerical solutions become diverse unavoidably. In this case, only a lot of experiences with the *numerical analysis* (not the analysis) could alleviate these difficulties.

In this thesis, three big studies to analyze problems of CED with particular and numerical solutions mentioned above are presented. In the section II, a new FDM for the microwave imaging reflectometry (MIR) (which is one of diagnostic techniques to observe tokamak plasmas) will be suggested with its calculation result, compared to other well-known FDMs' one. In the section III, an unexpected instability during the radiation pressure acceleration (RPA) with circularly polarized laser pulses is predicted by analytic calculations, and this prediction is verified by several numerical simulations. In the section IV, an analytic solution for the radiation reaction (RR) of a constantly accelerating charged particle is derived rigorously, and the physical interpretation for RR is suggested based on the solution. Other simple calculations that I have obtained are briefly written in the remaining sections. At last, the final conclusion and discussion will be presented.

II   Envelope-PIC hybrid method for the simulation of microwave reflectometry

2.1   Introduction

It is generally useful in control of a plasma system to obtain the information of plasma density fluctuation, since they are usually linked with development of instability or turbulence. Microwave reflectometry is one of the most widely used techniques to detect the density fluctuation in general plasma systems. In this diagnostic method, a probe microwave pulse propagates through the plasma, until it reaches the position of cut-off density, being reflected from that. By comparing the phases of the incident and reflected waves, the position of the cut-off can be determined. As the cut-off is closely related with the plasma density for a given frequency of the microwave via the dispersion relation, combined with optical theory, the phase data obtained from the reflectometry can be used to reconstruct the density fluctuation level [1]. Especially in a complicated plasma equipment like Tokamak, the reflectometry is extensively used to measure the density fluctuation, which is typically a symptom of beginning of the instability [2,3]. While the reflectometry is basically a point-detection method, recently the microwave imaging reflectometry (MIR) has also been suggested [4], where a curvature-matched, large-spot microwave is irradiated on the cut-off layer, from which the density fluctuation level of the cut-off layer can be imaged by measuring the phase fluctuation of the reflected wave.

For the reconstruction of the density fluctuation from the reflectometry or MIR data, it is essential to know the degree of correlation between the phase fluctuation of the reflected wave and the actual density fluctuation. To find that, numerical simulations on variously assumed density distribution can be employed. The first such method was solving a one-dimensional (1D) wave equation with Born approximation [5]. However, some issues which is beyond the coverage of the 1D model, such as rapid variation and Doppler effect of the reflected signal, led to advancement of two-dimensional (2D) method [6, 7]. In the FWR2D (full-wave-reflectometry 2D) code, they numerically solve the wave equation along with the plasma modeled by a dielectric with a certain refractive index determined from the dispersion formula. Since the dynamics of the plasma is not followed, the calculation is fast enough for the systematic parameter scanning. Though such a stationary plasma model is usually valid for the Tokamak plasma, where the time scale of the plasma dynamics is much slower than that of the microwave reflection, it is still hard to represent the general kinetic states of plasma such as the turbulence. Furthermore the inherent uncertainty of the refractive index for turbulent states make it difficult to have a confidence on the accuracy of the simulation results.

Particle-In-Cell (PIC) code, unlike the full-wave code, is free from the restriction of the stationary plasma model. Any plasma distribution can be realized and furthermore it doesn't require the refractive index for simulations at all. However, despite all these merits, there are few tries to apply the PIC method to reflectometry or MIR study, because it is not suitable for

the parametric study of the system due to its extremely slow computation compared with the stationary plasma model.

Motivated to compromise the self-consistency of the PIC and the fast calculation of the stationary model, we introduce a two-dimensional hybrid method. In this new novel scheme, we divide the simulation domain into two sub-groups, one is for low density region, and the other for near-cut-off. In the low density region, the kinetic effect is just weak, so the simulation time can be saved by solving paraxial wave equation along with the fluid model of the plasma. This part is similar to the full-wave code, but we added additional ability to set more various density states. The second group for a high density region including the cut-off layer, where strong kinetic effect can be influential in determining the phase change of the microwave, the PIC method is used. The novelty of our hybrid method is in interfacing those two fundamentally different models, which is substantially described in the next section. We succeeded in minimizing any numerical reflection of the wave and discontinuity of the plasma current on the interface of two sub-domains. Consequently, we obtained significantly improved overall calculation speed from pure PIC method, keeping almost the same accuracy of the original PIC calculation. We note that a similar combination of PIC and FWR2D has been pursued independently by Shi et al. [8]

In Sec. 2.2 the theoretical models for the paraxial part and the interfacing is described. In Sec. 2.3, the comparison of the intensity and phase data for three different methods, i.e. pure PIC, hybrid, and FWR2D, is presented, along with the description on the computational efficiency of the new method depending on the position of the interface. The summary is given in Sec. 2.4. Note that this study was published in 2018 [9].

2.2 Numerical Models

Figure 1 represents the schematic of the two-dimensional hybrid numerical scheme for MIR simulations. The probe microwave is launched from the left boundary of the simulation domain. The domain is divided into the envelope domain in the left and the pure-PIC domain in the right. Those two sub-domains are interfaced over a narrow section where the field and current data are shared by those two domains. Details of each domain and the interfacing are described as follows.

2.2.1 Envelope domain

In the envelope domain, the electromagnetic wave is modeled by envelope equations obtained from the paraxial approximation, and a linearized, quasi-steady-state fluid equation of an electron plasma is employed. At the starting point of the envelope equations, it is assumed that the electric field and current density have a slowly varying amplitude (envelope) and fast oscillation
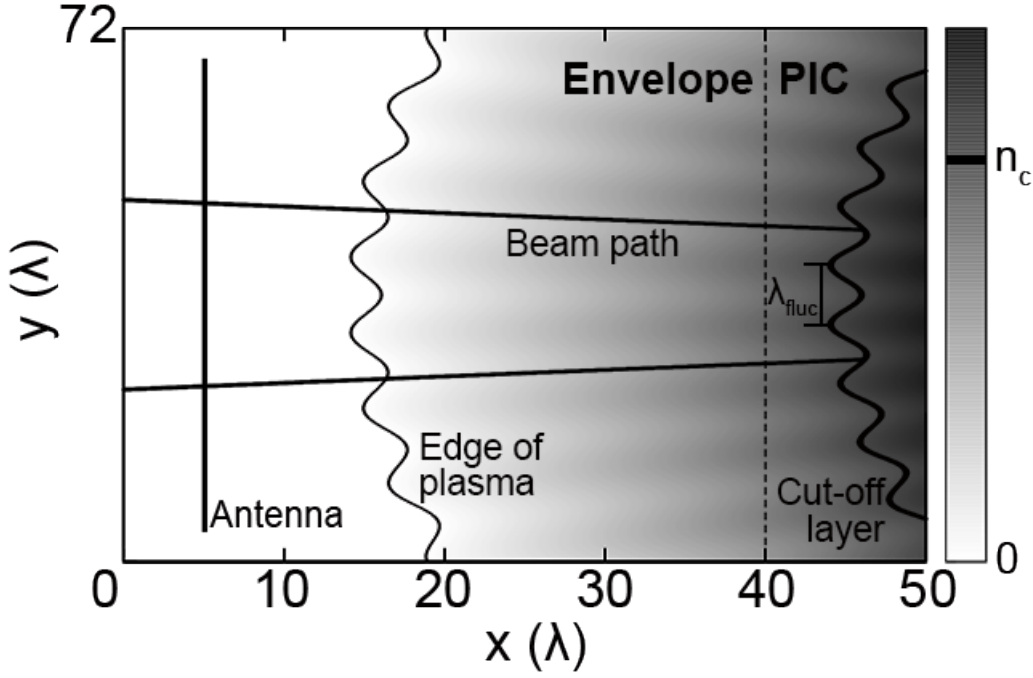
Figure 1: A schematic of the hybrid simulation of MIR. Simulation setting for $L_{ramp}=30\lambda$. The plasma density starts from x=15λ and increases linearly. The antenna for the reflected signal is located at x=5λ. The vertical dashed line represents the position of the domain interface.

term.

$$\mathbf{E} \simeq \frac{1}{2}\mathbf{E_0}e^{i(kx-\omega t)} + \text{c.c.} \tag{3}$$

$$\mathbf{J} \simeq \frac{1}{2}\mathbf{J_0}e^{i(kx-\omega t)} + \text{c.c.} \tag{4}$$

In addition, an external, static magnetic field $\mathbf{B}_{\text{Ext}}$ is also considered. The envelope model is useful in analyzing the phases of the reflected waves, as the phase information is directly reconstructed from the complex envelopes.

To get the equation of the electric field envelope $\mathbf{E_0}$, we use the wave equation of the electric field obtained from the time-dependent Maxwell equations.

$$\nabla^2\mathbf{E} - \nabla\left(\nabla \cdot \mathbf{E}\right) = \mu_0\frac{\partial \mathbf{J}}{\partial t} + \frac{1}{c^2}\frac{\partial^2 \mathbf{E}}{\partial t^2}. \tag{5}$$

For a paraxial wave with transversely-slowly-varying envelope, we assume that the longitudinal component of the electric field is irrotational ($\nabla \times E_{\parallel} = 0$), while the transverse component is solenoidal ($\nabla \cdot E_{\perp} = 0$). This is an exact relation for a completely-plain one-dimensional wave, and approximately correct for a paraxial wave. From this assumption, the wave equation (5) can be decomposed into the transverse and longitudinal components as follows.

$$\nabla^2 E_{\perp} = \mu_0\frac{\partial J_{\perp}}{\partial t} + \frac{1}{c^2}\frac{\partial^2 E_{\perp}}{\partial t^2} \tag{6}$$

$$0 = \mu_0 J_{\parallel} + \frac{1}{c^2}\frac{\partial E_{\parallel}}{\partial t}, \tag{7}$$

5

where $E_\parallel$ is E_x, and $E_\perp$ is E_y or E_z (and similarly, $J_\parallel$ is J_x, and $J_\perp$ is J_y or J_z). Substituting E and J in Eqs. (6) and (7) by (3) and (4), respectively, and canceling out the fast oscillation terms after multiplying $e^{-ikx+i\omega t}$, the envelope equations can be obtained as follows.

$$\frac{\partial E_{0\parallel}}{\partial t} - i\omega E_{0\parallel} = -c^2 \mu_0 J_{0\parallel} \tag{8}$$

$$\frac{\partial^2 E_{0\perp}}{\partial t^2} - 2i\omega \frac{\partial E_{0\perp}}{\partial t} = c^2 \left[\nabla^2 E_{0\perp} + 2ik \frac{\partial E_{0\perp}}{\partial x} - \mu_0 \frac{\partial J_{0\perp}}{\partial t} + i\omega\mu_0 J_{0\perp} \right]. \tag{9}$$

Differently from conventional envelope equations, where the second derivatives of the envelopes are usually neglected from the slowly varying assumption, we kept them to consistently calculate both right- and left-going waves by a single envelope: though Eqs. (3) and (4) represent a right-going envelope by $e^{ikz-i\omega t}$, the left-going one with $e^{-ikx-i\omega t}$ can still be calculated by allowing a fast varying phase of the envelopes E_0 and J_0, where the envelopes' phases compensate for the phase difference between the right- and left-going waves, i.e. $2ikx$.

To solve Eqs. (8) - (9) numerically, they are discretized in time and space as follows.

$$\frac{E_{0\parallel}^{n+1} - E_{0\parallel}^n}{dt} - i\omega \frac{E_{0\parallel}^{n+1} + E_{0\parallel}^n}{2} = -c^2 \mu_0 J_{0\parallel}^{n+\frac{1}{2}}. \tag{10}$$

longitudinally, and

$$\frac{E_{0\perp}^{n+1} - 2E_{0\perp}^n + E_{0\perp}^{n-1}}{dt^2} - 2i\omega \frac{E_{0\perp}^{n+1} - E_{0\perp}^{n-1}}{2dt}$$
$$= c^2 \left[\nabla^2 E_{0\perp}^n + 2ik \frac{\partial E_{0\perp}^n}{\partial x} - \mu_0 \frac{J_{0\perp}^{n+\frac{1}{2}} - J_{0\perp}^{n-\frac{1}{2}}}{dt} + i\omega\mu_0 \frac{J_{0\perp}^{n+\frac{1}{2}} + J_{0\perp}^{n-\frac{1}{2}}}{2} \right]. \tag{11}$$

transversely. Note that the discretized E_{0j}^n and $J_{0j}^{n+1/2}$ are defined at the same position in space, and temporarily separated by a half time step to secure the second order accuracy in time (leap-frog method). Accordingly, the electric field update in longitudinal direction is, from Eq. (10),

$$E_{0\parallel}^{n+1} = \left[\left(1 + i\frac{\omega dt}{2} \right)^2 E_{0\parallel}^n - c^2 dt \mu_0 J_{0\parallel}^{n+\frac{1}{2}} \right] \bigg/ \left(1 + \frac{\omega^2 dt^2}{4} \right). \tag{12}$$

The updating equation for transverse electric field envelope is

$$E_{0\perp}^{n+1} = \beta \left(1 + 2i\omega dt \right) / \left(1 + 4\omega^2 dt^2 \right) \tag{13}$$

with

$$\beta = \alpha + 2E_{0\perp}^n - (1 + 2i\omega dt) E_{0\perp}^{n-1} \tag{14}$$

and

$$\alpha = c^2 dt^2 \left[\frac{\partial^2 E_{0\perp}^n}{\partial x^2} + \frac{\partial^2 E_{0\perp}^n}{\partial y^2} + 2ik \frac{\partial E_{0\perp}^n}{\partial x} \right.$$
$$\left. - \mu_0 \left\{ \left(1 - i\frac{\omega dt}{2} \right) \frac{\partial J_{0\perp}}{\partial t} \bigg|^n - i\omega J_{0\perp}^{n-\frac{1}{2}} \right\} \right]. \tag{15}$$

6

Throughout the equations (12) and (13), the $(n+1)$'th value is derived from the known quantity E_0^n and $J_0^{n+1/2}$. To get the current term at $(n+1/2)$'th step, we use

$$\mathbf{J}_0^{n+\frac{1}{2}} = \mathbf{J}_0^{n-\frac{1}{2}} + \left.\frac{\partial \mathbf{J}_0}{\partial t}\right|^n dt, \tag{16}$$

The partial differential term in the right-hand-side can be induced from a linearized fluid equation of an electron plasma driven by the Lorentz's force:

$$\frac{\partial \mathbf{J}}{\partial t} \simeq \frac{q_e}{m_e}\left[\rho\mathbf{E} + \mathbf{J} \times \mathbf{B}_{\text{Ext}}\right]. \tag{17}$$

For Eq. (16) we neglected the convectional term of the fluid equation, assuming a small amplitude of the probe wave. With the paraxial approximation for the current density [Eq. (4)], the stationary fluid equation can be represented in a matrix form as follows.

$$\frac{\partial \mathbf{J}_0}{\partial t}^n = \left[\overset{\leftrightarrow}{\mathbf{T}}^2 + \frac{\omega^2 dt^2}{4}\overset{\leftrightarrow}{\mathbf{I}}\right]^{-1} \cdot \mathbf{W} \tag{18}$$

$$\mathbf{W} = \left[\overset{\leftrightarrow}{\mathbf{T}} + i\frac{\omega dt}{2}\overset{\leftrightarrow}{\mathbf{I}}\right] \cdot \mathbf{V}$$

$$\mathbf{V} = \frac{q_e}{m_e}\left[\rho\mathbf{E}_0^n + \mathbf{J}_0^{n-\frac{1}{2}} \times \mathbf{B}_{\text{Ext}}\right] + i\omega\mathbf{J}_0^{n-\frac{1}{2}}$$

$$\overset{\leftrightarrow}{\mathbf{T}} = \overset{\leftrightarrow}{\mathbf{I}} + \frac{dt}{2}\frac{q_e}{m_e}\begin{pmatrix} 0 & -B_z & B_y \\ B_z & 0 & -B_x \\ -B_y & B_x & 0 \end{pmatrix}.$$

Here $\overset{\leftrightarrow}{\mathbf{I}}$ is a unit matrix and $B_{x,y,z}$ in the matrix $\overset{\leftrightarrow}{\mathbf{T}}$ are the components of $\mathbf{B}_{\text{Ext}}$ in each direction.

Generally the longitudinal mesh size dx in the envelope domain can be larger than the probe beam wavelength, since the equations contains the spatially slowly-varying amplitude terms only. However, in this paper, we use the same finely-resolving mesh in the envelope domain as in the PIC to enable the calculation of both the right- and left-going waves by a single envelope. This makes the interfacing of the PIC and envelope domains easier.

2.2.2   PIC domain

In the PIC domain, the temporally evolving Maxwell's equations are solved by the regular finite-difference-time-domain (FDTD) method on the Yee mesh [10]. In this mesh structure, $\mathbf{E}$ and $\mathbf{J}$ are defined at the center of the mesh side, and $\mathbf{B}$ at the center of the mesh surface. Temporally $\mathbf{B}$ and $\mathbf{J}$ are at the same time step, and $\mathbf{E}$ is off from them by a half time step to secure the second order accuracy in time. The current density is interpolated from the simulation particles following Villasenor-Buneman's scheme [11].

To separately match the real and imaginary parts of the envelope fields to those from PIC simulations at the domain interface, imaginary counter-parts of the wave and current density are calculated simultaneously in the PIC domain. This may possibly reduce overall computation efficiency of the hybrid method. However, we expect there is another way to emiliorate this
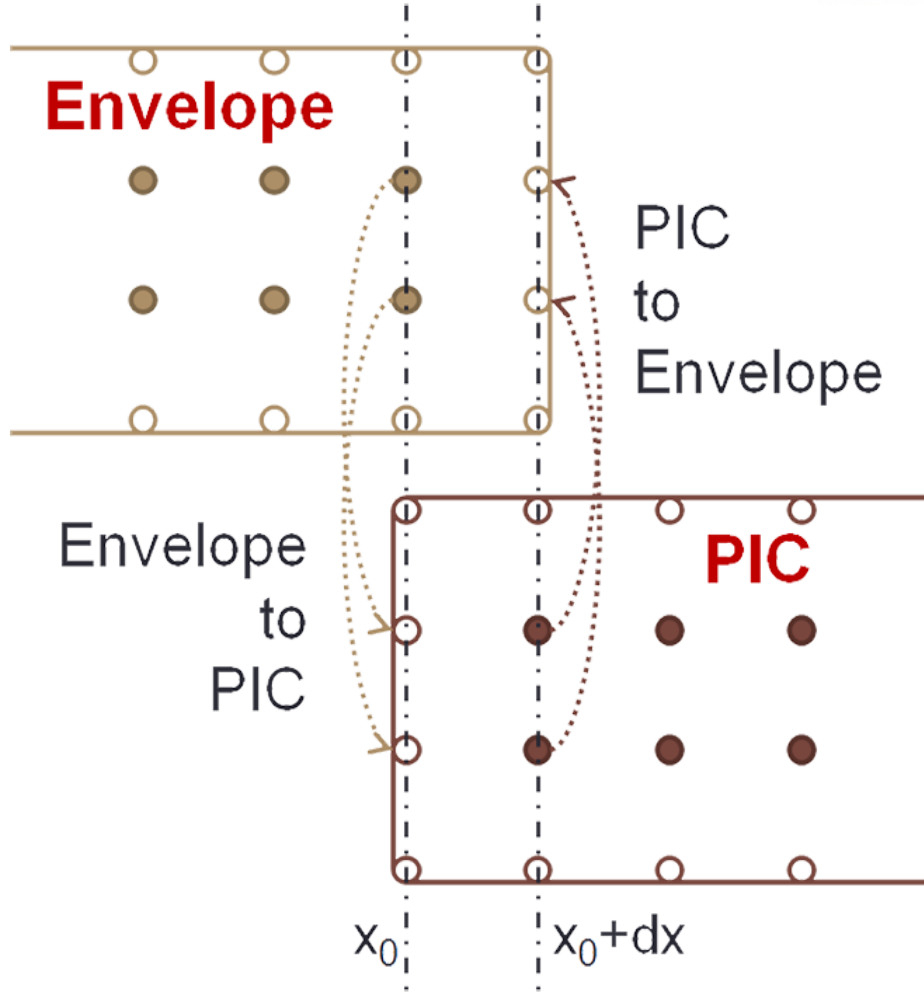
Figure 2: Field data from the PIC domain are transmitted to the Envelope domain for every time step and vice versa. For data transmission from the envelope to PIC, Eqs. (19) and (20) are used and for the opposite case, Eqs. (21) and (22) are used.

deficiency. The approach to determine $\Im(E)$ of the wave in the PIC domain by analyzing the phase of the real part field is under development.

2.2.3 Domain Interface

Each domain determines the electric field by using different numerical methods, so the difference should be translated appropriately at the interface. In order to do that, we made both domains overlap over one mesh as in Fig. 2.

Supposing that x_0 is the left-end coordination of the PIC domain, the right boundary of the envelope domain is set on $x_0 + \mathrm{d}x$, where $\mathrm{d}x$ is the mesh size. As the envelope solver is second-order in space, boundary conditions both at left and right-ends are required. The left-boundary value of the envelope comes from the wave launching condition, which is determined from the paraxial equations of the Gaussian wave. The right-end value is equated to the PIC data at

8

$x_0 + dx$. Meanwhile, the left boundary value of the PIC domain is provided with by the data from the envelope domain at x_0. Though the right-hand boundary condition is not well-defined in the PIC part, it is not necessary since the derivatives of Maxwell's equation is first-order in space. This process can be written by equations as

$$\Re\{\mathbf{E}(x_0, y)\} = \Re\{\mathbf{E}_0(x_0, y)\}\cos(kx_0 - \omega t) - \Im\{\mathbf{E}_0(x_0, y)\}\sin(kx_0 - \omega t) \tag{19}$$

$$\Im\{\mathbf{E}(x_0, y)\} = \Im\{\mathbf{E}_0(x_0, y)\}\cos(kx_0 - \omega t) + \Re\{\mathbf{E}_0(x_0, y)\}\sin(kx_0 - \omega t) \tag{20}$$

$$\begin{aligned} \Re\{\mathbf{E}_0(x_0 + dx, y)\} &= \Re\{\mathbf{E}(x_0 + dx, y)\}\cos\{k(x_0 + dx) - \omega t\} \\ &\quad + \Im\{\mathbf{E}(x_0 + dx, y)\}\sin\{k(x_0 + dx) - \omega t\} \end{aligned} \tag{21}$$

$$\begin{aligned} \Im\{\mathbf{E}_0(x_0 + dx, y)\} &= \Im\{\mathbf{E}(x_0 + dx, y)\}\cos\{k(x_0 + dx) - \omega t\} \\ &\quad - \Re\{\mathbf{E}(x_0 + dx, y)\}\sin\{k(x_0 + dx) - \omega t\} \end{aligned} \tag{22}$$

Above equation is applied before the calculation of each domain for the wave transmission through the interface.

The advantage of such an overlapped interface is that matching of the current density from each domain is not necessary. As long as the Villasenor-Buneman scheme is employed in the current calculation in the PIC, the charged particle motion in the left side of x_0 does not contribute to the current density in $x > x_0$. Therefore the electron current can be determined just by the field calculated in PIC domain only. As the matching of the current data is waived, the numerical algorithm can be significantly simplified. Note that we used the same mesh size for both envelope and PIC regions, leading to the minimized numerical reflection of the waves at the interface. Because the mesh size is small ($< k^{-1}$) in the envelope region, the reduction of the computation time in envelope region would not be significant compared to full wave solvers. Improvement of our scheme for interfacing much larger mesh in the envelope region with the small mesh of the PIC region, without harming the minimized numerical reflection at the interface, is under progress.

2.3 Simulation Results

Benchmark of the hybrid numerical model was conducted for a two-dimensional MIR system. Specifically we measured the transverse distribution of intensity and phase of reflected waves from cut-off layers in plasmas. In this section, we present the comparisons of three different codes, the hybrid, pure PIC, and FWR2D, in terms of accuracy and calculation speed for various different plasma conditions.

The two dimensional simulation settings for the MIR simulations are presented in Fig. 1. The frequency of the probe microwave is 86 GHz, corresponding to λ=3.486 mm, and the focal waist is 12 mm. The plasma is assumed to be locally circular-shaped with radius of the cut-off layer ρ_0=361 mm. Then the focal position of the incident probe wave is determined by the curvature matching condition: the local radius of the phase front of the probe wave is matched
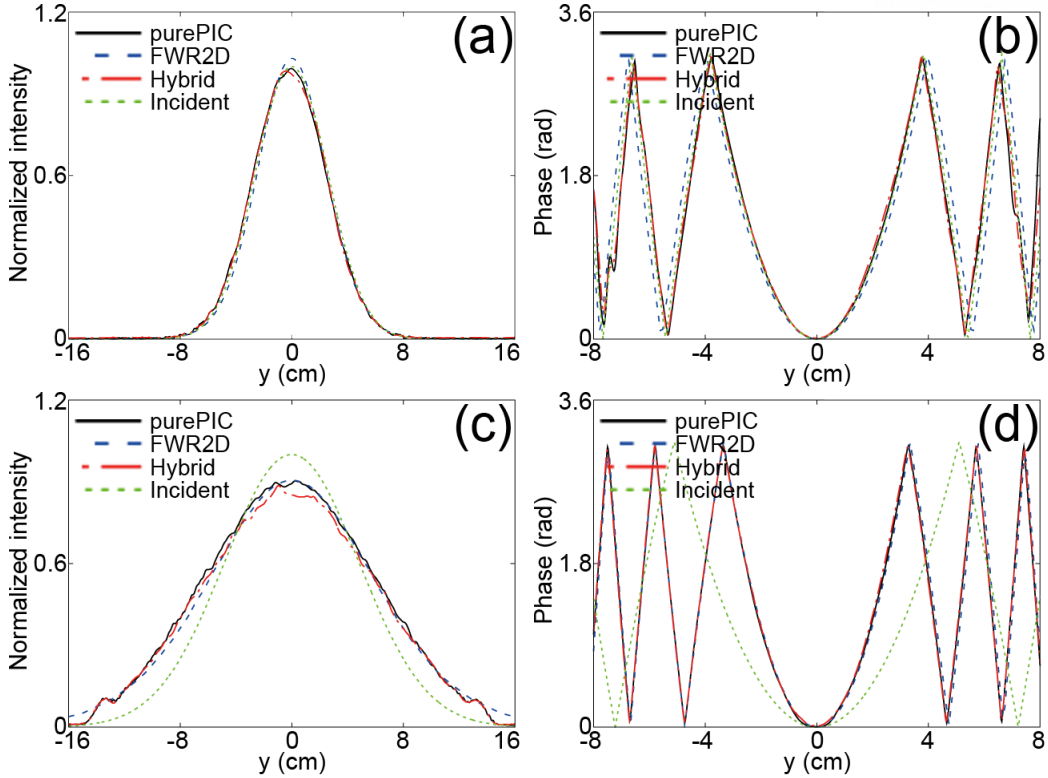
Figure 3: Comparisons of incident and reflected waves from three different codes for L_{ramp}=10λ plasma without fluctuation. (a)-(b) transverse distribution of the intensities and phases for curvature-matched case, and (c)-(d) for non-matched case.

to the radius of the cutoff layer. We varied the length of the linear density ramp from the edge of plasma to the cutoff layer L_{ramp} as 10λ, 30λ and 50λ. The wavelength (λ_{fluc}) of the stationary, sinusoidal density fluctuation was also changed for a given fluctuation amplitude A_{fluc}=1λ. In particular, the location of the cut-off layer is given by

$$\rho_{\mathrm{cut}} = \rho_0 - A_{\mathrm{fluc}} \cos\left(\frac{2\pi\rho_0}{\lambda_{\mathrm{fluc}}}\theta\right), \tag{23}$$

where ρ_0 is the radius of the circularly-shaped cut-off layer without fluctuation, and θ is the angle from the propagation axis. Subsequently the density in other region varies in at the same way. The external magnetic field is 2.618 T in z direction, so that the critical density is 1.355×10^{19} 1/m^2 for the X-mode propagation of the probe wave.

2.3.1 The case with no density fluctuation

First, we compared the simulation results when there is no fluctuation in the plasma density. Two cases are conducted: one is for the curvature-matched case, and the other is non-matched case (Fig. 3). For the latter, the probe wave is set to focus at 100λ beyond the focal position for the curvature matched case. The density ramp is 10λ, and the domain interface is located at 5λ from the cut-off. In the curvature-matched case, three different codes consistently yield the

10

matching of incident and reflected waves both in intensity and phase. In the non-matched case, the reflected wave shows slightly divergent intensity distribution, while the phase is narrowed down. The three results from different codes are in good agreement with each other. Some fluctuation in the reflected intensity can be found for pure PIC and the hybrid simulations, which can be further reduced by increasing the number of super-particles per cell. For this particular cases, we used 30 particles per cell (near the cut-off) both for PIC and hybrid simulations.

2.3.2 The case with density fluctuation

Second, we performed the simulations with three different fluctuation wavelengths at the cut-off layer: 8λ, 12λ, and 16λ (Fig. 4). The amplitude of the fluctuation is fixed to 1λ and the density ramp $L_{\mathrm{ramp}}=30\lambda$. The domain interface is located at $x=40\lambda$, which corresponds to 5λ from the cut-off layer. This means that the PIC domain occupy 20 percent of the total domain area, and 50 percent of plasma. For those cases, the agreement between three different codes is good enough so that the deviation between codes is much smaller than the fluctuation level itself induced by the density fluctuation.

2.3.3 Position of Interface and Calculation Speed

The third simulations show the difference of the results from three different codes depending on the position of the domain interface. In these simulations, we used a longer density ramp than the previous cases, i.e. $L_{ramp} = 50\lambda$. The fluctuation level is $\lambda_{fluc}=8\lambda$. As the domain interface moves toward the cut-off layer, the portion occupied by the PIC part decreases, which may result in increased calculation speed. We found that in these simulations, the portion taken by the envelope part is negligibly small compared to that of the PIC part. Hence the overall calculation speed is dominantly determined by the PIC part only.

Figure 5 represents the speed-up of the hybrid calculation relative to the pure PIC (corresponding to the case where the domain interface is located at $x = 0$.) When the interface is located at 7λ from the cut-off layer, we obtained three-times speed-up of the calculation. For this case where the interface is closest to the cut-off layer, the numerical difference between the three codes are still minor compared to the actual fluctuation induced by the density ripple (Fig. 6).

2.4 Conclusion

We introduced two-dimensional hybrid method for the fast and accurate simulations of microwave reflectometry. Specifically the PIC algorithm is used for the calculation of high density region near cut-off, while the low density region is calculated by conventional steady-state dielectric model of the plasma. Using the technique of overlapping the boundaries of those heterogeneous domains over one mesh length, the numerical reflection of the wave at the interface could be minimized below one percent. The benchmarks against a pure PIC and the
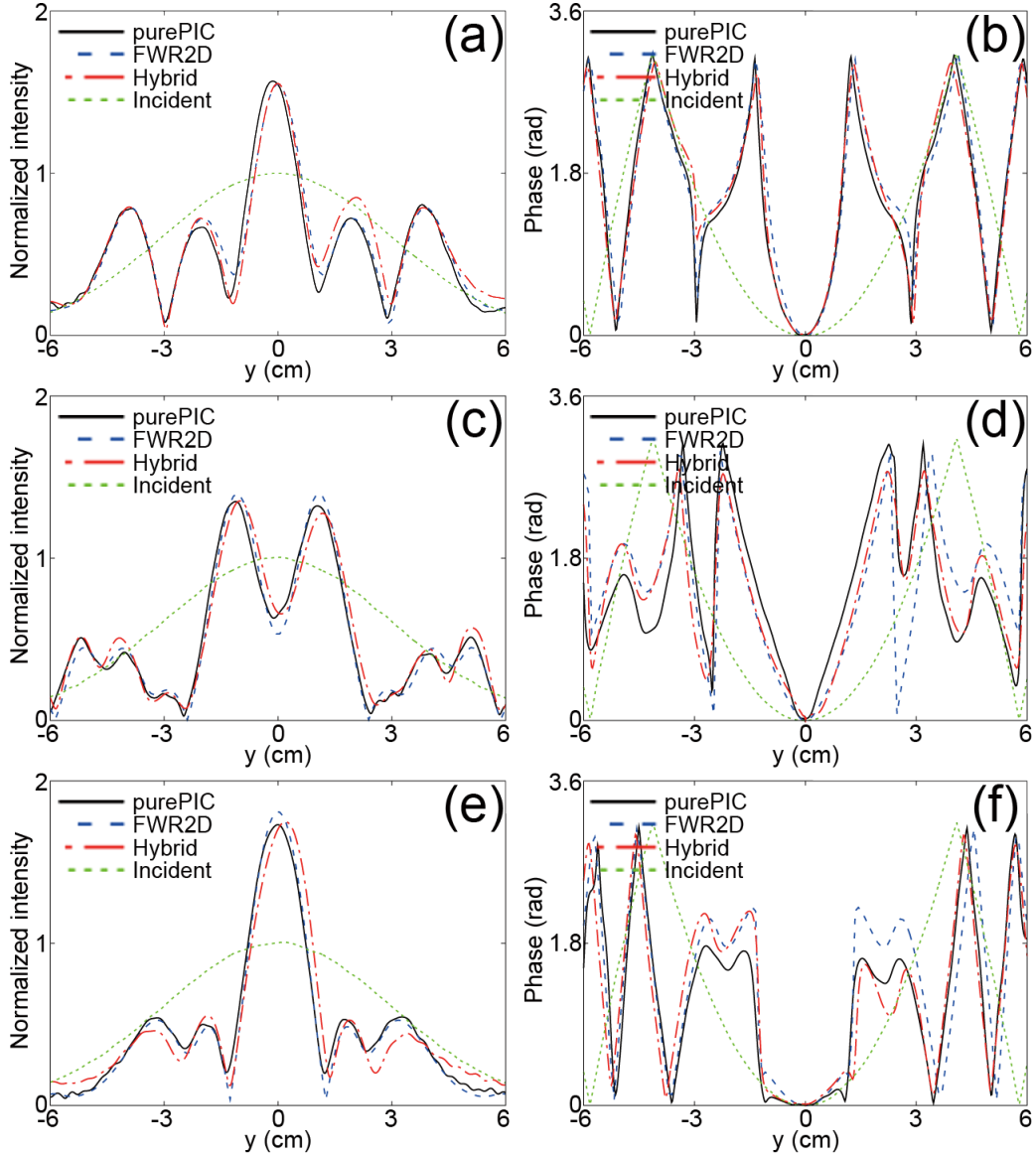
Figure 4: Comparison of the reflected waves from three different codes for the fluctuated plasma with $A_{\text{fluc}}=1\lambda$ and $L_{ramp}=30\lambda$. The interface is located at 5λ from the cut-off layer. (a)-(b) transverse distribution of the intensities and phases for $\lambda_{\text{fluc}}=8\lambda$ case, (c)-(d) for $\lambda_{\text{fluc}}=12\lambda$, and (e)-(f) for $\lambda_{\text{fluc}}=16\lambda$.
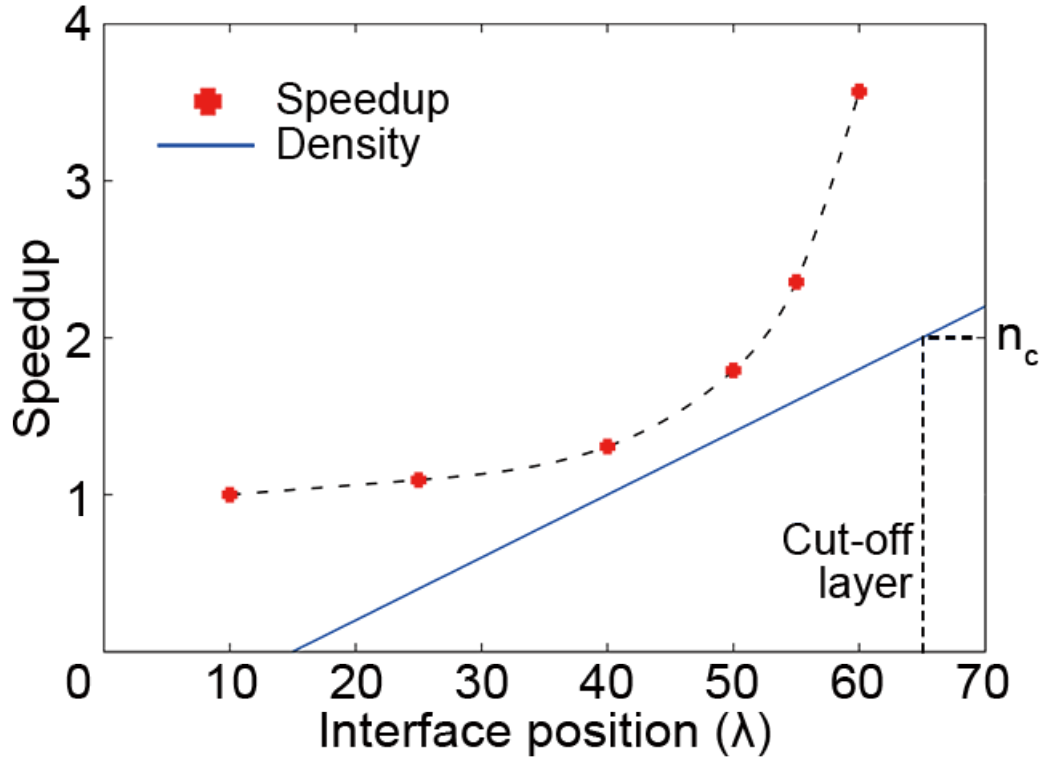
Figure 5: Speedup of the hybrid code depending on positions of the interface. The total longitudinal domain length is 70λ. The plasma density increases linearly from $x=15\lambda$ and the cut-off layer is located at $x=65\lambda$.
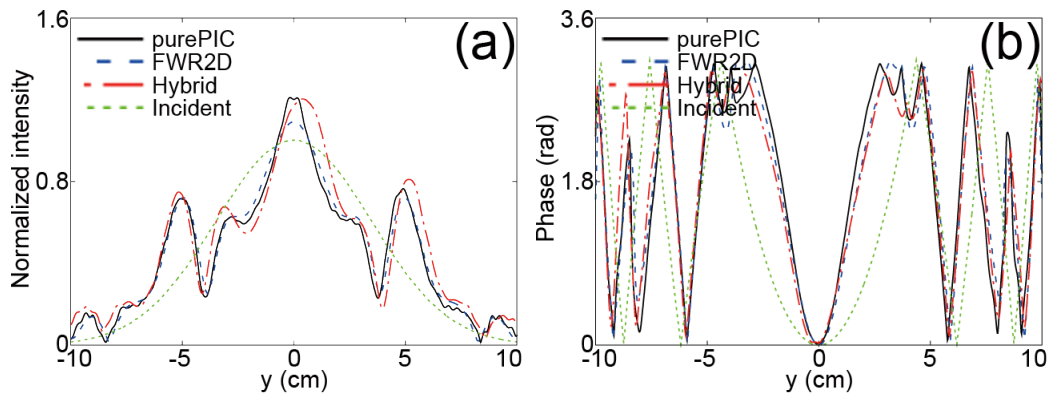
Figure 6: Comparison of the reflected waves from three different codes for the fluctuating plasma with $\lambda_{\text{fluc}}=8\lambda$, $A_{\text{fluc}}=1\lambda$, and $L_{\text{ramp}}=50\lambda$. The interface position is located at 7λ from the cut-off layer. (a), (b) transverse distribution of the intensities and phases.

FWR2D show excellent agreement both in phase and intensity of the probe wave for the cases of stationary density ripple, while at least three-times speed-up of the calculation is obtained compared to the pure PIC. We expect that the speed-up factor can be even enhanced as the size of the plasma increases.

In this paper, just the stationary plasma was used to demonstrate the accuracy and the speed-up of the new method. From such a good benchmark results, the hybrid method is expected to show an effectiveness in the simulation of complex state with highly dynamic fluctuation or turbulence, where the hybrid code (or pure PIC) and the FWR2D can potentially yield different results. Finding actually such situations remains as a future study.

III Unstable expansion of plasma foils accelerated by circularly-polarized laser pulses in non-transparent regimes

3.1 Introduction

For decades the system of thin plasma foils irradiated by ultra-intense laser pulses has been considered to be a compact source of highly energetic ion beams [12] or ultrashort electromagnetic (EM) pulses in ultra-intense, high-frequency regimes [13]. Interest in those outcomes is growing rapidly owing to their novel applications [14, 15]; the ion beams generated from the laser-foils might enable table-top nuclear and particle physics [16, 17], proton radiography [18, 19], and hadron therapy [20]. Furthermore, the ultrashort X-ray pulses from the laser-foil interaction are suitable for studying the dynamics of ultrafast ionization [21], attosecond spectroscopy [22], and the diagnostics of warm dense matters [23].

Recently the rapid development of laser technologies [24–26], where the intensity has reached 10^{22} W/cm^2 recently [27] and more than $I = 10^{24}$ W/cm^2 is being approached by new facilities under construction [28, 29], are making the applications mentioned above more feasible. In such a high intensity regime, the irradiated foil is accelerated rapidly to reach the relativistic speed and is compressed to a substantially high density such that it acts like a mirror moving at a relativistic speed [30, 31].

One essential recipe to generate a relativistic plasma mirror efficiently is the circular polarization (CP) of the laser pulses. The non-oscillatory, slow-varying ponderomotive forces of the CP-pulse suppresses the surface heating of the foil, which helps raise the transparency threshold [32, 33], possibly enabling a higher momentum transfer from the laser pulse to the foil. According to the previous theories, for stable compression and acceleration of the foil, the amplitude of CP lasers should satisfy

$$a_I \quad \leq \quad \zeta_e, \tag{24}$$

where a_I $(= eE_I/m_e c\omega_L)$ is the normalized amplitude of incident lasers, ζ_e $(= \pi n_e l_e/n_c \lambda_L)$ is the normalized surface density of electrons, l_e is the thickness of electrons, and ω_L and λ_L are the angular frequency and the wavelength of lasers. Equation (24) was derived to meet the two different conditions necessary for stable acceleration: balancing the radiation pressure to the restoring force [34, 35] and keeping the foil opaque [36]. Specifically Eq. (24) indicates that the electron layer directly driven by the ponderomotive force of the laser pulse should not be detached completely from the ion layer, which is dragged by the electrostatic force, and the plasma density should be high enough to prevent the relativistic transparency.

Here it is important to note that a_I and ζ_e in Eq. (24) are the ones measured in the quasi-inertial frame co-moving with the foil (in contrast, we use the primed variables to represent the quantities in the laboratory frame). Even when the system starts with the initial conditions of the laser and foil not satisfying Eq. (24), the system can enter a stable regime quickly as

the foil is compressed and a_I/ζ_e decreases in the accelerating foil frame. As the two different conditions for the opacity and the balance between the ponderomotive and electrostatic forces are associated with a single equation (24), this equation has been considered to be a primary condition for stable interactions of CP-lasers and foils [37, 38].

Despite its usefulness, Eq. (24) is known to be just a rough criterion for stable acceleration of the foil, as it is based on the assumption of negligible ion motion [34, 35] or thickness of the foil [36]. Interestingly, in our one-dimensional (1D) particle-in-cell (PIC) simulations, we observed some cases, where the foils expand suddenly even when $a_I \leq \zeta_e$. Similar expansion had been reported previously [39–45], mostly by the Weibel instability or breakout afterburner in the relativistically transparent regime. In contrast, we observed the unstable expansion in the non-transparent regime. In Fig. 7, for the cases where $a'_{I\max} \geq 1.8\zeta'_e$ [but still satisfying Eq. (24) in the foil frame as indicated in Fig. 7(a)], the thicknesses of the foil starts to increase considerably from around $t' \approx 60$ fs. Figure 7(b) strongly implies that there is a threshold of the foil expansion between the cases of $a'_{I\max} = 1.5\zeta'_e$ and $a'_{I\max} = 2.0\zeta'_e$; more precise measurement of the simulation data in Fig. 7(b) indicates that the derivative $\partial l_e/\partial a'_{I\max}|_{t'=\mathrm{const}}$ becomes discontinuous at $a'_{I\max} \approx 1.8\zeta'_e$, which implies that the expansion is a threshold behavior rather than a smooth transition. This unstable expansion could be fatal, as it would decrease the energy density of the foils, and possibly lead to the destruction of the relativistic plasma mirror. Furthermore, the observed instability is contradictory to the general perception about the CP-pulses, which usually snow-ploughs the electron layer smoothly until the restoring electrostatic force generated by the charge separation balances the ponderomotive force [34, 35]. A modified theory model is necessary for proper interpretation of this novel instability. The unstable expansion has been observed consistently with a decreasing mesh size and time step and simultaneously, with an increasing number of simulation particles in our PIC simulations. Hence it strongly indicates that the observation does not originate from numerical artifact of the simulations, but is a physical effect.

In this paper we theoretically prove that there is indeed a new expansion instability of the foil accelerated by a CP-pulse. Scrutinizing the equation of Akhiezer-Polovin (AP) [46–48] for CP-pulse propagation in a plasma, we find a more elaborate condition for the stable acceleration of the foil, which modifies the previous condition (24). While Eq. (24) is valid only for a very thin foil or fixed ion distributions, our new equation holds for a foil with finite thickness (but still thin enough to make the assumption of a uniform slab reasonable.) and includes the self-consistent calculation of number of ions inside the accelerating foils [49, 50]. Furthermore, based on the data from a series of 1D PIC simulations, we suggest universal initial parameters of the laser and the foil in the laboratory frame for the system to meet the new stability conditions (note that the new and old stability conditions (24) are all described in the foil frame, rather than in the laboratory frame). It is also shown that the thresholds for the unstable expansion and the transparency, whose threshold has not been published as well, do not necessarily coincide with each other, contrasting with the feature implied by Eq. (24). The solutions of the AP
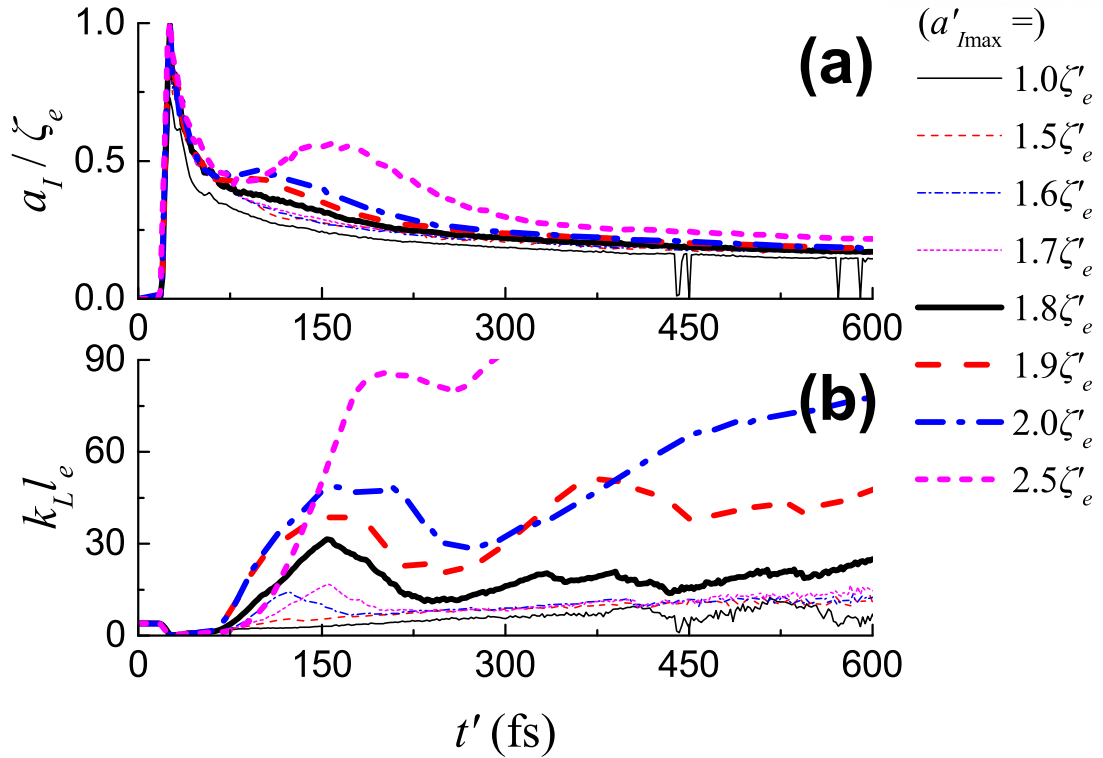
Figure 7: 1D PIC results for various $a'_{I\max}$ values where $\zeta'_e = 100$. The results represent (a) the amplitude-to-density ratio a_I/ζ_e at the foil position x_0, and (b) the normalized thickness $k_L l_e$. The incident lasers satisfied Eq. (35) and the thickness values were equal to $2\sqrt{3}\sigma_x$, where $\tau' = 6$ fs and σ_x is the standard deviations of the electron densities $n_e(x)$. For the simulation, the grid size $\Delta x'$ and the time step $\Delta t'$ were defined as 0.8 nm and 2.0 as. Note that $\lambda'_L = 0.8$ μm, and $\Delta x' = \lambda'_L/1000$.

equation presented here are completely different from previous ones. For instances, in Ref. [47], a propagating mode in a completely *transparent* regime was derived, while our solution is for a completely *non-transparent* regime. In Ref. [48], a *semi-infinite* plasma was considered with *fixed* ions, while our solutions are for a thin foil, and include the change in number of ions by the foil acceleration. Note that this study was submitted [51].

3.2   Stability condition of slab-like plasmas

In the laser-foil interaction, the shape of the plasma foil is controlled primarily by the motion of the electrons. Hence, the dynamics of the foil can be understood by investigating the force exerting on the electrons. Here it is important to consider the distribution of the force on the electrons inside the foil with finite thickness. With $\partial_y = \partial_z = 0$ in 1D in $\hat{\mathbf{x}}$-direction, we consider the ponderomotive and the electrostatic forces exerting on the electrons ($F_x = F_{\mathrm{pm}} + F_{\mathrm{st}}$). The ponderomotive force F_{pm} is caused by the electromagnetic fields of the laser pulse. Assuming the quasi-static state every moment of interaction between the CP laser pulse and the foil (which

is a reasonable assumption, as there is no fast-oscillating component of the ponderomotive force in CP), Akhiezer and Polovin [46–48] derived wave equation of the CP-pulse satisfies the relativistic wave equation in a plasma;

$$
\frac{1}{k_L^2}\frac{\partial^2 \mathbf{a}_\perp}{\partial x^2} + \left(1 - \frac{n_e/n_c}{\sqrt{1+a_\perp^2}}\right)\mathbf{a}_\perp = 0, \tag{25}
$$

where $\mathbf{a}_\perp = a_y\hat{\mathbf{y}} + a_z\hat{\mathbf{z}}$, and $k_L = 2\pi/\lambda_L = \omega_L/c$. It is well-known that for an overcritical plasma density if the change in the ion density n_i is not considered (i.e. immobile ions), Eq. (25) can be rewritten by a first-order differential equation [48, 52–55] which is given by

$$
\frac{1}{2k_L^2\left(1+a_\perp^2\right)}\left(\frac{\partial a_\perp}{\partial x}\right)^2 + \frac{a_\perp^2}{2} - \frac{n_i}{n_c}\left(\sqrt{1+a_\perp^2} - 1\right) = 0, \tag{26}
$$

Its solution is known to be

$$
\sqrt{1+a_\perp^2} - 1 = \frac{2\left(n_i - n_c\right)}{n_i\sinh^2\left(k_L x\sqrt{n_i/n_c - 1} + C\right) + n_c}, \tag{27}
$$

where C is an arbitrary constant. This solution shows how the pondromotive potential (and also the electron density n_e) is determined for a given, constant n_i, and it could be valid for the hole-boring process, where the ion density remains relatively invariable during that process. However, the assumption of the immobile ions for Eq. (27) is not sufficient to explain the next stage (i.e. such as light sail of a thin foil) shown in the Fig. 5(b) of Ref. [49], because the ion density inside the accelerating foil is not arbitrary, but should be determined self-consistently by the inertial and ponderomotive force.

Here we find the analytic solution of Eq. (25) for an accelerating thin foil. In contrast to Eq. (27), the electron density n_e is assumed to be given, and the ion density n_i and the distribution of the ponderomotive force inside the foil is calculated. To make the calculation simple, we suppose the electron density n_e is uniform over $x_0 \leq x \leq x_0 + l_e$ during the light-sail. The assumption of the constant density n_e is a little crude, but is eventually found to be valid for a thin enough foil ($k_L l_e \ll 1$), as verified later by good comparison of our solution against the simulation data as in Fig. 8. We also assume that the electron density is high enough so that the laser pulse is reflected entirely. With these assumptions, Eq. (25) can be expressed by

$$
\frac{1}{2k_L^2}\left(\frac{\partial a_\perp}{\partial x}\right)^2 + \frac{a_\perp^2}{2} - \frac{n_e}{n_c}\left(\sqrt{1+a_\perp^2} - 1\right) = 0, \tag{28}
$$

which gives an asymptotic solution (see the appendix)

$$
\sqrt{1+a_\perp^2} - 1 = \frac{2n_e}{n_c}\sin^2\left(k_L\frac{x_0 + d - x}{2}\right) \tag{29}
$$
$$
\left(x_0 \leq x \leq x_0 + d\right),
$$

where d is the skindepth given by

$$
d = \frac{2}{k_L}\sin^{-1}\left(\frac{a_I}{n_e/n_c}\right). \tag{30}
$$

18

As can be expected, the ponderomotive potential (29) is independent from the ion density n_i, in contrast to the solution of Eq. (27) considered in Refs. [48, 52–55].

The electrostatic force $F_{\rm st}$ is caused by the charge distribution and is obtained from Gauss' law; $\partial_x a_x = k_L (n_i - n_e)/n_c$. Assuming the ion density n_i is constant over the electron layer (but is not necessarily constant outside) and $a_x = 0$ where $x > x_0 + l_e$ (i.e. negligible transparent field in the rear side of the foil), we obtain

$$a_x = \frac{n_e - n_i}{n_c} k_L (x_0 + l_e - x) \tag{31}$$
$$(x_0 \leq x \leq x_0 + l_e).$$

which represents the normalized electrostatic field inside the foil.

It is possible to see how the distribution of the force $F_x(x)$ exerting on the electron layer affects the expansion or compression of the foil. Simply, the expansion (or compression) of the foil is determined by the difference between the forces on the front ($F_x(x_0)$) and the rear ($F_x(x_0 + l_e)$) sides of the foil. From Eqs. (29) and (31), the difference of the force ΔF_x is written as

$$
\begin{aligned}
\Delta F_x &\equiv F_x(x_0 + l_e) - F_x(x_0) \\
&= \frac{e^2 n_e l_e}{\epsilon_0} \left(1 - \frac{\zeta_i}{\zeta_e} - \frac{a_I}{\zeta_e} \sqrt{1 - \frac{a_I^2}{\zeta_e^2} \frac{k_L^2 l_e^2}{4}} \right),
\end{aligned} \tag{32}
$$

where ζ_i is the normalized surface density of the ions within the electron layer ($\zeta_i = \pi n_i l_e / n_c \lambda_L$). $\Delta F_x > 0$ means that the foil would expand and vice versa. Equation (32) shows that $\Delta F_x \leq 0$ when $\zeta_i \approx \zeta_e$ implying that the foil does not expand as long as it stays neutral. Practically, however, the foil cannot remain neutral, because the accelerating electrons usually leave the ions behind. According to Refs. [49, 50], the ions rearrange themselves so that the electrostatic and inertial forces are balanced. The force balance leads to

$$\frac{\zeta_i}{\zeta_e} \approx 1 - \frac{a_I^2}{\zeta_e^2}. \tag{33}$$

Note that Eq. (33) could not be deduced from Eq. (27), as it neglects the ion density variation. Equation (33) indicates that $a_I \to \zeta_e$ leads to $\zeta_i \ll \zeta_e$ and $\Delta F_x \propto 1 - \sqrt{1 - k_L^2 l_e^2/4} > 0$, which means the conventionally allowed maximum amplitude ($a_I = \zeta_e$) causes an expansion of the foil. In other words, in the foil frame, the actual threshold for the amplitude of CP laser pulses should be smaller than the conventional threshold for the stable compression of the slab.

The new condition for the stable compression and acceleration of the foil is, by substituting Eq. (33) into Eq. (32), given by

$$\frac{a_I}{\zeta_e} \leq \frac{1}{\sqrt{1 + k_L^2 l_e^2/4}}. \tag{34}$$

The solid curve in Fig. 8(a) shows the border of the stable regime in the space of a_I/ζ_e vs. $k_L l_e$, represented by Eq. (34). Here it is worthwhile to recall our observation of the unstable foil
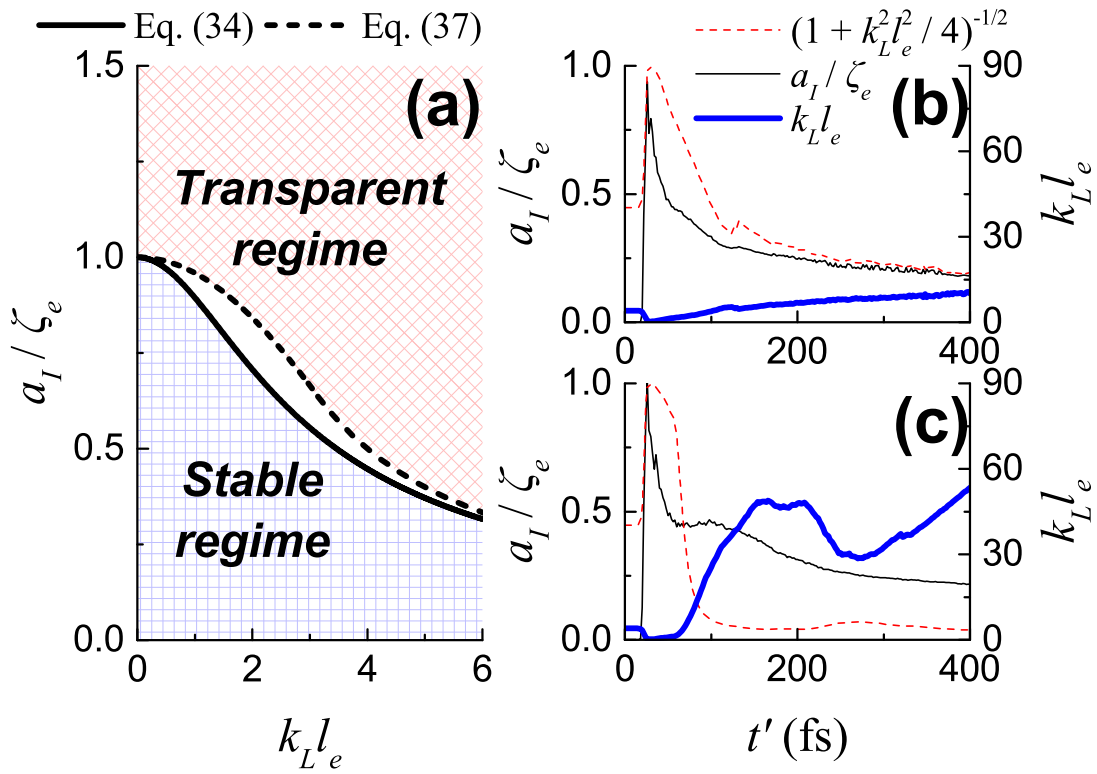
Figure 8: (a) A slab-like foil's stable and transparent conditions which satisfy Eqs. (34) and (37), and comparisons of Eq. (34) in the both cases when (b) $a'_{I\max} = 1.5\zeta'_e$ and (c) $a'_{I\max} = 2.0\zeta'_e$ of Fig. 7.

expansion described in Fig. 7(b), where the expansion rate of the foil changes discontinuously between $a'_{I\max} = 1.5\zeta'_e$ and $a'_{I\max} = 2.0\zeta'_e$. Figures 8(b) and 8(c) strongly imply that such a sudden change in the expansion rate is related to the instability threshold determined by Eq. (34); Figs. 8(b) and 8(c) represent the evolution of the foil thickness $(k_L l_e)$ and the comparison of a_I/ζ_e and $(1 + k_L^2 l_e^2/4)^{-1/2}$, measured from simulations for those two cases. It is found that for $a'_{I\max} = 1.5\zeta'_e$, Eq. (34) holds throughout the simulation and the expansion of the foil remains very slow (the slow expansion is thought to be thermal expansion, which is not considered in this paper). In contrast, for the other case, the thickness of the foil starts to increase rapidly, as soon as the condition (34) breaks. All the considerations hitherto strongly indicate that the instability is a physical phenomenon rather than a numerical noise and Eq. (34) describes the instability threshold well.

3.3   Initial parameters for stable compression of the foil

In the previous section, we derived the stability condition in a foil frame. Now we discuss the initial parameters of the laser and the foil in a laboratory frame, for which the system can be driven into the stable regime, where Eq. (34) is satisfied. Unfortunately, it is very difficult to deductively find the relationship between the initial parameters and Eq. (34), because l_e in Eq. (34) is a dynamically evolving parameter. Actually, in order to predict l_e precisely, the thermal pressure $\boldsymbol{\nabla} p_e$ caused by electron heating should be counted in $F_x(x)$ as well as F_{pm} and F_{st}. However, as far as we know, the research has yet to clarify the mechanism of relativistic electron heating by CP lasers [32,56]. In the absence of a known theory to predict $\boldsymbol{\nabla} p_e$, we find an appropriate connection between the initial parameters and Eq. (34) via a series of 1D PIC simulations. In particular, we measured the time t'_{end} at which the new stability condition (34) breaks due to the thermal expansion of the foil. Once the foil expands beyond the threshold given by Eq. (34), unless a_I/ζ_e decreases very quickly, the parameters of the pulse and the foil, i.e. a_I/ζ_e and $k_L l_e$ go further away from the stable region, leading to the disruption of the foil. Hence the pulse energy incident on the foil beyond t'_{end} no longer contributes to the foil compression and acceleration. This information is useful to determine the maximum pulse length and to eventually avoid the unnecessary use of the pulse energy. In our simulations we considered a CP pulse with Gaussian-ramping-up and infinitely long flat-top beyond that. The pulse profile was given by

$$a'_I(\xi') = \begin{cases} 0 & (\xi' = -3\tau'), \\ a'_{I\max} e^{-(\xi'/\tau')^2} & (-3\tau' < \xi' < 0), \\ a'_{I\max} & (\xi' \geq 0), \end{cases} \tag{35}$$

where $\xi' = t' - x'/c - 3\tau'$. Note that ξ' is defined so that a'_I becomes zero at $t' = x' = 0$. We define $\xi'_{\mathrm{end}} \equiv t'_{\mathrm{end}} - x'_0|_{t'=t'_{\mathrm{end}}}/c - 3\tau'$, where x'_0 means the front of the electron layer in the lab-frame. From the definition of ξ'_{end} (and t'_{end}), the pulse energy beyond $\xi' \geq \xi'_{\mathrm{end}}$ is practically useless in the foil compression.
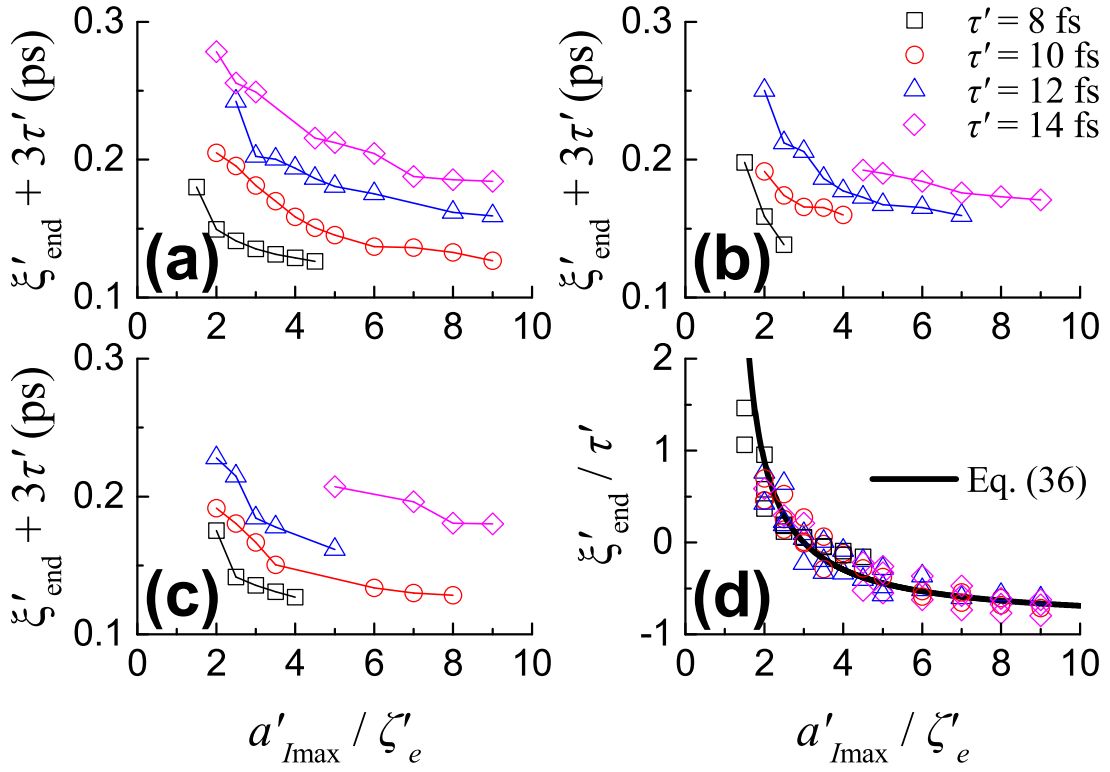
Figure 9: Measurements of ξ'_{end} for various $a'_{I\mathrm{max}}$, ζ'_e, and τ' from 1D PIC simulations. (a) $\zeta'_e = 100$, (b) $\zeta'_e = 50$, and (c) $\zeta'_e = 150$. (d) $\xi'_{\mathrm{end}}/\tau'$ for all the cases of τ' and ζ'_e from (a–c) as a function of $a'_{I\mathrm{max}}/\zeta'_e$ and the comparison with Eq. (36). The simulation parameters are the same as in Fig. 7, except τ' and ζ'_e.

Figure 9 shows the measurements of $\xi'_{\rm end}$ for various τ', the peak amplitude of the laser pulse ($a'_{I\rm max}$), and the initial surface density of the foil (ζ'_e). In Fig. 9(d), it is noticeable that the values of normalized $\xi'_{\rm end}$, i.e. $\xi'_{\rm end}/\tau'$ lie on nearly a single line regardless of τ' or ζ'_e, at least for 8 fs $\leq \tau' \leq$ 14 fs and $\zeta'_e < a'_{I\rm max} < 10\zeta'_e$. We found that the following curve fits the simulation data in Fig. 9(d) very well;

$$\frac{\xi'_{\rm end}}{\tau'} \approx \frac{\sqrt{\pi}}{2}\left(\frac{2}{a'_{I\rm max}/\zeta'_e - 1} - 1\right) \tag{36}$$
$$\left(a'_{I\rm max} > \zeta'_e\right).$$

Equation (36) can be used as a good phenomenological guide for the optimized parameters of the laser and foil, to accomplish the maximum compression for the given energy of the pulse. Note that $\xi'_{\rm end}$ becoming negative for $a'_{I\rm max} > 3\zeta'_e$ in Eq. (36) means that the foil compression ends before the pulse reaches its peak. Equation (36) indicates the foil can be stable when $a'_{I\rm max} > \zeta'_e$, unless the duration is infinite. As practical pulse duration is finite, the peak amplitude should satisfy $a'_{I\rm max} > \zeta'_e$ to maximize the efficiency. This is an interesting point as it is exactly opposite to the previous criterion, Eq. (24), which is commonly misunderstood to be the lab-frame parameter condition. More elaborate three dimensional simulations might suggest modification of Eq. (36), but it is beyond the scope of this paper.

3.4 Relativistic transparency of slab-like plasmas

Finally we would like to remark on the transparency of the foil to the CP laser pulses. The previous stability condition (24) gives the thresholds of the transparency and the stable acceleration simultaneously. However, in our modified theory, we discovered that the breaking of the new stability condition (34) does not necessarily lead to the transparency. As one reasonable definition of the transparency of the foil, it can be defined by the skindepth reaching the rear side of the electron layer. From Eqs. (25) and (29), the skindepth d can be found to be Eq. (30) (see the appendix for the derivation). Then requiring $d > l_e$ yields

$$\frac{a_I}{\zeta_e} > \begin{cases} \dfrac{2}{k_L l_e}\sin\left(\dfrac{k_L l_e}{2}\right) & (k_L l_e < \pi), \\[2mm] \dfrac{2}{k_L l_e} & (k_L l_e \geq \pi). \end{cases} \tag{37}$$

The threshold curve for the transparency from Eq. (37) is located slightly higher than the stability curve from Eq. (34) as seen in Fig. 8(a). The different thresholds indicate that the instability occurs when the transparency was induced, while the opposite does not hold: as the foil expands, it can possibly go through the unstable but still opaque regime for a short time. The difference is minute, but it can be important in particular applications, for instances, the CP-shock [32] or breakout afterburner instablility [40–42] where the transparency has a key role. In this regard, the newly derived Eqs. (34) and (37) can be related to the relativistic electron heating and the self-induced transparency by the CP-pulses, which is yet to have been studied completely.

3.5 Summary

In summary, the unstable expansion of plasma foils, driven by CP laser pulses, were observed in 1D PIC simulations, even with the system parameters subject to the conventional stability condition, Eq. (24). From the analysis of the Akhiezer-Polovin equation, we found a new stability condition, Eq. (34), to explain the simulation results. While the previous and new stability conditions are defined in the foil frame, the semi-analytic equation (36) indicates the stability condition in the lab-frame. One important conclusion of this equation is that the foils can be stable even when $a'_{I\max} > \zeta'_e$. Furthermore, we also discovered that the opaqueness-transparency boundary in the foil-laser parameter space does not necessarily coincide with the boundary for stable compression.

3.6 Solution for the equation of Akhiezer and Polovin

In steady-state interaction between electrons and a circularly polarized laser, the normalized laser amplitude $\mathbf{a}_\perp$ satisfies the equation of Akhiezer-Polovin, which is given by Eq. (25). The solution of this equation can be assumed to be

$$
\begin{aligned}
a_y(x,t) &= a_\perp(x)\cos(\psi(x) - \omega_L t), \\
a_z(x,t) &= a_\perp(x)\sin(\psi(x) - \omega_L t),
\end{aligned}
\tag{38}
$$

where $\psi(x)$ is an arbitrary function for the phase. By substituting the assumed solution for $\mathbf{a}_\perp$ in Eq. (25), we obtain

$$
\frac{1}{k_L^2}\frac{\partial^2 a_\perp}{\partial x^2} + \left[1 - \frac{n_e/n_c}{\sqrt{1+a_\perp^2}} - \frac{1}{k_L^2}\left(\frac{\partial\psi}{\partial x}\right)^2\right]a_\perp = 0,
\tag{39}
$$

$$
\frac{a_\perp^2}{k_L}\frac{\partial\psi}{\partial x} = S_1,
\tag{40}
$$

where S_1 is a constant. The above two equations yield

$$
\frac{1}{k_L^2}\frac{\partial^2 a_\perp}{\partial x^2} + \left(1 - \frac{n_e/n_c}{\sqrt{1+a_\perp^2}} - \frac{S_1^2}{a_\perp^4}\right)a_\perp = 0,
\tag{41}
$$

which can be rewritten as

$$
\frac{1}{2k_L^2}\left(\frac{\partial a_\perp}{\partial x}\right)^2 + \frac{a_\perp^2}{2} + \int_x^\infty \frac{n_e(x')}{n_c}\frac{\partial\sqrt{1+a_\perp(x')^2}}{\partial x'}\,\mathrm{d}x' + \frac{S_1^2}{2a_\perp^2} - S_2 = 0,
\tag{42}
$$

where S_2 is another integration constant. If $n_e(x)$ is constant and large enough ($n_e \gg n_c$), it is reasonable to write that $a_\perp = \partial_x a_\perp = S_1 = 0$ when $x \to \infty$. Also, $S_1^2/a_\perp^2$ becomes zero from Eq. (40). Eventually, Eq. (25) will be represented as

$$
\frac{1}{2k_L^2}\left(\frac{\partial a_\perp}{\partial x}\right)^2 + \frac{a_\perp^2}{2} - \frac{n_e}{n_c}\left(\sqrt{1+a_\perp^2} - 1\right) = 0.
\tag{43}
$$

The solution of this equation is

$$k_L x + C = 2\tan^{-1}\left[\sqrt{\frac{2n_e}{n_c}\left(\sqrt{1+a_\perp^2}-1\right)\Big/a_\perp^2-1}\right]$$

$$+ \tanh^{-1}\left[\frac{\sqrt{2n_e\left(\sqrt{1+a_\perp^2}-1\right)\Big/a_\perp^2}-n_c}{\sqrt{n_e-n_c}}\right]\Bigg/\sqrt{\frac{n_e}{n_c}-1}, \qquad (44)$$

when $0 \le a_\perp < 2\sqrt{n_e^2/n_c^2 - n_e/n_c}$. The constant C is determined by the amplitude a_I of the incident laser.

3.6.1 Fields of right-going and left-going waves

Electric fields of a laser propagating in $\pm\hat{\mathbf{x}}$-direction can be represented as

$$\mathbf{E}_\pm = \frac{\mathbf{E}_\perp \pm c\mathbf{B}_\perp \times \hat{\mathbf{x}}}{2}. \qquad (45)$$

By substituting $\mathbf{E}_\pm$ into Maxwell's equation, we obtain

$$\frac{1}{c}\frac{\partial}{\partial t}\left(E_+^2 - E_-^2\right) + \frac{\partial}{\partial x}\left(E_+^2 + E_-^2\right) + \frac{\mathbf{J}_\perp}{\epsilon_0}\cdot\frac{\partial\mathbf{A}_\perp}{\partial x} = 0. \qquad (46)$$

Because $\mathbf{J}_\perp \approx -en_e\mathbf{v}_\perp$ and $\gamma m_e\mathbf{v}_\perp \approx e\mathbf{A}_\perp$, Eq. (46) can be rewritten as

$$\frac{1}{c}\frac{\partial}{\partial t}\left(E_+^2 - E_-^2\right) + \frac{\partial}{\partial x}\left(E_+^2 + E_-^2\right) - \frac{n_e m_e c^2}{\epsilon_0}\frac{\partial}{\partial x}\sqrt{1 + \frac{e^2 A_\perp^2}{m_e^2 c^2}} = 0. \qquad (47)$$

If the plasma is assumed to be static ($\partial_t = 0$) and opaque ($E_+^2 = E_-^2$), the above equation yields

$$\frac{\partial}{\partial x}\left(2a_+^2\right) = \frac{n_e}{n_c}\frac{\partial}{\partial x}\sqrt{1 + a_\perp^2}, \qquad (48)$$

With constant n_e, this equation can be integrated to be

$$2a_+^2 = \frac{n_e}{n_c}\left(\sqrt{1+a_\perp^2}-1\right). \qquad (49)$$

3.6.2 Asymptotic solution

If $n_e \gg n_c$, Eq. (44) is approximated to be

$$k_L x + C \approx 2\tan^{-1}\left[\sqrt{\frac{2n_e}{n_c}\left(\sqrt{1+a_\perp^2}-1\right)\Big/a_\perp^2-1}\right]. \qquad (50)$$

The inverse of this equation is

$$\sqrt{1+a_\perp^2}+1 \approx \frac{2n_e}{n_c}\cos^2\left(\frac{k_L x + C}{2}\right). \qquad (51)$$

Because we assumed $n_e \gg n_c$, the equation can be rewritten as

$$\sqrt{1+a_\perp^2}-1 \approx \frac{2n_e}{n_c}\cos^2\left(\frac{k_L x + C}{2}\right), \qquad (52)$$

so that $a_\perp$ avoid an imaginary part. Note that Eq. (52) holds only for $0 \le k_L x + C < \pi$.

The constant C should satisfy Eq. (49). If $a_0 = a_\perp|_{x=x_0}$ and $a_I = a_+|_{x=x_0}$ where x_0 is the front of the electron layer, Eq. (52) leads to

$$
\begin{aligned}
\sqrt{1 + a_0^2} - 1 &\approx \frac{2n_e}{n_c} \cos^2 \left(\frac{k_L x_0 + C}{2} \right) \\
&\approx \frac{2a_I^2}{n_e/n_c},
\end{aligned}
\tag{53}
$$

and accordingly C is given by

$$
C \approx \pi - k_L x_0 - 2 \sin^{-1} \left(\frac{a_I}{n_e/n_c} \right).
\tag{54}
$$

If we substitute this equation for C in Eq. (52), we obtain Eq. (29);

$$
\sqrt{1 + a_\perp^2} - 1 \approx \frac{2n_e}{n_c} \sin^2 \left(k_L \frac{x_0 + d - x}{2} \right),
\tag{29}
$$

where $d \equiv (2/k_L) \sin^{-1}(a_I n_c/n_e)$. As mentioned, Eq. (29) holds only for $0 \le k_L x + C < \pi$, and this range can be represented by $x_0 + d - \pi/k_L \le x < x_0 + d$. Noting that x_0 is the position of the front, the range should be rewritten as $x_0 \le x < x_0 + d$. In this regard, d can be a skin (or penetration) depth because $a_\perp \approx 0$ when $x \ge x_0 + d$.

3.7 Self-induced transparency of slab-like plasma

Actually, the skin depth d is defined by

$$
d \equiv \begin{cases} \dfrac{2}{k_L} \sin^{-1} \left(\dfrac{a_I}{n_e/n_c} \right) & \left(a_I \le \dfrac{n_e}{n_c} \right), \\ \infty & \left(a_I > \dfrac{n_e}{n_c} \right). \end{cases}
\tag{55}
$$

It means the electrons become under-dense when $a_I > n_e/n_c$. Lasers in under-dense plasmas propagate continuously and the skin depth is infinite. Now we suppose l_e is the thickness of the electron slab. As d is the penetration depth, transparency will be induced if $d > l_e$.

When $a_I \le n_e/n_c$, the transparency condition is given by

$$
d > l_e \quad \rightarrow \quad \frac{a_I}{\zeta_e} > \frac{2}{k_L l_e} \sin \left(\frac{k_L l_e}{2} \right),
\tag{56}
$$

where ζ_e is the normalized surface density of the electrons, and $\zeta_e = n_e k_L l_e/2$. On the other hand, the condition $d > l_e$ always holds for $a_I > n_e/n_c$. Therefore, the condition can be represented by

$$
d > l_e \quad \rightarrow \quad \frac{a_I}{\zeta_e} > \frac{2}{k_L l_e}.
\tag{57}
$$

From that $k_L d = \pi$ when $a_I = n_e/n_c$, the condition for the transparency is obtained as Eq. (37);

$$
\frac{a_I}{\zeta_e} > \begin{cases} \dfrac{2}{k_L l_e} \sin \left(\dfrac{k_L l_e}{2} \right) & (k_L l_e \le \pi), \\ \dfrac{2}{k_L l_e} & (k_L l_e > \pi). \end{cases}
$$

3.8 The amount of protons in an electron layer

In the moving frame, whose speed is equal to that of the electron layer (v'_{xe}), protons feel the electric force given by

$$\frac{\mathrm{d}}{\mathrm{d}t}\left(m_p \gamma_p v_{xp}\right) = eE_x - \frac{\mathrm{d}}{\mathrm{d}t'}\left(\frac{m_p v'_{xe}}{\sqrt{1-(v'_{xe}/c)^2}}\right), \tag{58}$$

where the primed variables represent the quantities in the laboratory frame. The last term is the inertial force, and we assume the Coulomb and inertial forces will be balanced;

$$\begin{aligned}
eE_x &= \frac{\mathrm{d}}{\mathrm{d}t'}\left(\frac{m_p v'_{xe}}{\sqrt{1-(v'_{xe}/c)^2}}\right) \\
&= \frac{m_p}{\left[1-(v'_{xe}/c)^2\right]^{3/2}}\frac{\mathrm{d}v'_{xe}}{\mathrm{d}t'}.
\end{aligned} \tag{59}$$

In the lab frame, the acceleration of the electron layer is represented as

$$\frac{\mathrm{d}\mathbf{v}'_e}{\mathrm{d}t'} = -\frac{e}{\gamma'_e m_e}\left(\mathbf{E}' + \mathbf{v}'_e \times \mathbf{B}' - \frac{\mathbf{v}'_e}{c^2}\mathbf{v}'_e \cdot \mathbf{E}'\right). \tag{60}$$

If we assume the layer is thin and opaque, accoring to Eq. (46), we obtain

$$\begin{aligned}
E'_x + v'_{ye}B'_z - v'_{ze}B'_y &= E_x - \frac{2\epsilon_0 E_I^2}{e n_e l_e}, \\
\mathbf{E}' \cdot \mathbf{v}'_e &= v'_{xe}\left(E_x - \frac{2\epsilon_0 E_I^2}{e n_e l_e}\right).
\end{aligned} \tag{61}$$

From Eqs. (61) and (60),

$$\begin{aligned}
\frac{\mathrm{d}v'_{xe}}{\mathrm{d}t'} &= \frac{1-(v'_{xe}/c)^2}{\gamma'_e m_e}\left(-eE_x + \frac{2\epsilon_0 E_I^2}{n_e l_e}\right) \\
&= \frac{\left[1-(v'_{xe}/c)^2\right]^{3/2}}{\gamma_e m_e}\left(-eE_x + \frac{2\epsilon_0 E_I^2}{n_e l_e}\right).
\end{aligned} \tag{62}$$

From this equation, Eq. (59) can be rewritten as

$$eE_x\left(1 + \frac{m_p}{\gamma_e m_e}\right) = \frac{m_p}{\gamma_e m_e}\frac{2\epsilon_0 E_I^2}{n_e l_e}. \tag{63}$$

As we supposed a slab-like plasma, Gauss' law yields

$$E_x = (n_e - n_p)\frac{e l_e}{2\epsilon_0}, \tag{64}$$

from which eventually we obtain the amount of protons in the electron layer;

$$\frac{\zeta_p}{\zeta_e} = 1 - \frac{a_I^2/\zeta_e^2}{1 + \gamma_e m_e/m_p} \tag{65}$$

where $\zeta_p = n_p k_L l_e/2n_c$. Because $m_p \gg m_e$, this equation can be approximated to be Eq. (33);

$$\frac{\zeta_p}{\zeta_e} \approx 1 - \frac{a_I^2}{\zeta_e^2}.$$

IV Radiation reaction from a constantly accelerating point-like rigid conductor

4.1 Introduction

Although Maxwell equation is an old result published in 1861, it is still being taken into account significantly in the both general relativity and quantum mechanics which are two big branches of the modern physics. It is because this equation is not only well-verified by experiments, but also almost uncontroversial because of its mathematical beauty. Accordingly, the classical electrodynamics (CED) which is a theory model based on Maxwell equation has naturally been away the major issues for physicists. However, even though this classic theory looks perfect, actually it has an unacceptable and fatal problem that researchers might have been unconcerned about. The problem is that CED cannot explain the conservation of energy (or momentum) for a *charged point-particle*, which must be the most fundamental element of the CED system. As well-known, the charge of a point particle yields diverging electric energy, and it means the energy conservation equation for the particle is mathematically undefinable. In other words, as the conservation equation is equivalent to the equation of motion, *ironically* the classical electrodynamics is unable to describe the 'dynamics' of point charges [57].

Of course, since the quantum mechanics was developed successfully, it might have become nonsense to consider the shape of a particle as a point. Despite this, however, there are two big reasons that it is still worth trying to deeply investigate 'the problem of point particle (PPP)' in CED. First, in the macroscopic world the real particles are extremely small, and its cause is still unclear. Owing to this, for theoretical physicists, the best way to describe these materials mathematically is just approximating them by ideal point-particles. It is not because the theorists actually believe the shape of the particle should be a point, but because the approximation is the strongest research method that they try preferentially. One successful example of this approach would be the Lorentz's equation of motion, normally called 'Lorentz force.' This equation not only has supposed the ideal point-particles, but also has been derived in a quite unrigorous way; as mentioned, describing the motion of a point charge is impossible in a strict sense because of PPP in CED. However, in spite of this suspicious derivation, this equation remarkably well-explain almost every observed motions of the real particles. Therefore, unless it is just a coincidence, it implies that approximating the real particle by a point charge is acceptable at least in the macroscopy. In this moment, PPP casts very interesting doubts: what additional phenomena will be involved in the modified equation of motion which is derived much more rigorously, and whether they will be observable or just delusional. Further, these doubts lead to the second reason which indicates the importance of PPP.

In fact, over a half century ago Dirac already had derived an equation of motion quite rigorously, called 'Lorentz-Abraham-Dirac equation.' Unfortunately, even this equation was insufficient to solve PPP, because of its causality violation and contradiction (whose details will

be presented later). However, the notable point is that the concepts of renormalization and radiation reaction were already involved in this equation, a decade before the quantum electrodynamics (QED) was published [58]. These concepts cannot be exactly interpreted even by the latest field theories, and its implication is very meaningful; possibly, the unsolved problems of the classical and quantum mechanics might be connected. Therefore, as the connection between the both mechanics is still unclear, the importance of PPP is never negligible.

Thankfully, great interests in this old problem (PPP) are emerging again due to the recent constructions of ultra-intense laser facilities, which can generate a laser pulse with 10^{24} W/cm^2 intensity. In this intensive regime, the additional phenomena that Lorentz force does not involve are expected to be observed experimentally. Actually, since Dirac suggested his equation of motion, a lot of theorists have suggested the modified equations to prepare this future experiment, but none of them could not avoid their contradictions and errors [59]. Hence, as actual operation of the facilities are imminent, a consistent and uncontradictory theory model to explain PPP and experiment data is now required desperately.

In this section I present a very special charge distribution which is not only *rigid* in a constantly accelerating non-inertial frame, but also *conductive* so that the inside fields are vanished. Moreover, the most important characteristic of this distribution is that its outside fields are completely equal to the fields of *a point charge*. Therefore, I would like to define a material named 'point-like rigid conductor (PRC)' whose charge distribution satisfies the above conditions that we mentioned. PRC can not be distinguished from the actual point charge even by extremely precise measurements (unless the inside can be observed). It means PRC would be the best alternative to investigate the dynamics of the ideal point charge. Note that in this document I am only interested in a constantly accelerating PRC.

4.1.1 Rigid body

The classical equation of motion for many-body systems is given by

$$\frac{\mathrm{d}}{\mathrm{d}t} \sum_i m_i \mathbf{v}_i \quad = \quad \sum_i \mathbf{F}_i. \tag{66}$$

A non-rotating rigid body can be defined as a group of particles whose momentums satisfy $m_i \mathbf{v}_i = m_i \mathbf{v}_0$, where $\mathbf{v}_0$ is the velocity of the rigid body.

In relativity, the rigid bodies are not *rigid* anymore. For example, the shape of a constantly accelerating sphere shell [60] would be represented as

$$x^2 + y^2 + \left(z - \sqrt{z_0^2 + c^2 t^2} \right)^2 \quad = \quad R_0^2, \tag{67}$$

where R_0 is the radius of the shell. This equation seems to imply the shell is a moving rigid

body. However, if we suppose another inertial frame whose coordinates is given by

$$
\begin{aligned}
c\bar{t} &= \Gamma\left(ct - \frac{V}{c}z\right), \\
\bar{x} &= x, \\
\bar{y} &= y, \\
\bar{z} &= \Gamma\left(z - \frac{V}{c}ct\right),
\end{aligned}
\tag{68}
$$

where V is the velocity of the frame and $\Gamma = \left(1 - V^2/c^2\right)^{-1/2}$. In this frame, the shape will be rewritten as

$$
\bar{x}^2 + \bar{y}^2 + \left[\Gamma\left(\bar{z} + \frac{V}{c}c\bar{t}\right) - \sqrt{z_0^2 + \Gamma^2\left(c\bar{t} + \frac{V}{c}\bar{z}\right)^2}\right]^2 = R_0^2,
\tag{69}
$$

which can not indicate any sphere shells. It means the relativistic rigid body can remain *rigid* only when it is represented in a particular frame.

4.1.2 Conductor

The static energy of charge distributions is given by

$$
\frac{\epsilon_0}{2}\int \rho\left(\mathbf{r}\right)\Phi\left(\mathbf{r}\right)\mathrm{d}^3 r = U.
\tag{70}
$$

A conductor is defined as an ideal metal in which electric fields become zero. By definition, interestingly, a static conductor satisfies $\rho\left(\mathbf{r}\right)\Phi\left(\mathbf{r}\right) = \rho\left(\mathbf{r}\right)\Phi_0$ where Φ_0 is the scalar potential on the conductor (like a rigid body satisfies $m_i\mathbf{v}_i = m_i\mathbf{v}_0$).

In general electrodynamics, the vanished electric fields within conductors can not be induced from the constant scalar potential distribution as the fields are also consist of the vector potential, which makes the problem really difficult.

4.2 Non-inertial frame

The distribution of the PRC is almost impossible to be obtained in ordinary inertial frames. Hence, we need to define a constantly accelerating non-inertial frame which is also called Rindler frame [61]. Note that the derivation for this frame will be presented in the appendix 4.5.

Suppose an observer whose motion $\boldsymbol{\chi}$ in an inertial frame can be written as

$$
\boldsymbol{\chi}\left(t\right) = \sqrt{z_0^2 + c^2 t^2}\,\hat{\mathbf{z}},
\tag{71}
$$

which is same with the motion of a charged particle on constant electric fields. The boosted coordinates for this observer are represented as

$$
\begin{aligned}
c\bar{t} &= z_0 \tanh^{-1}\left(\frac{ct}{z}\right), \\
\bar{x} &= x, \\
\bar{y} &= y, \\
\bar{z} &= \sqrt{z^2 - c^2 t^2},
\end{aligned}
\tag{72}
$$
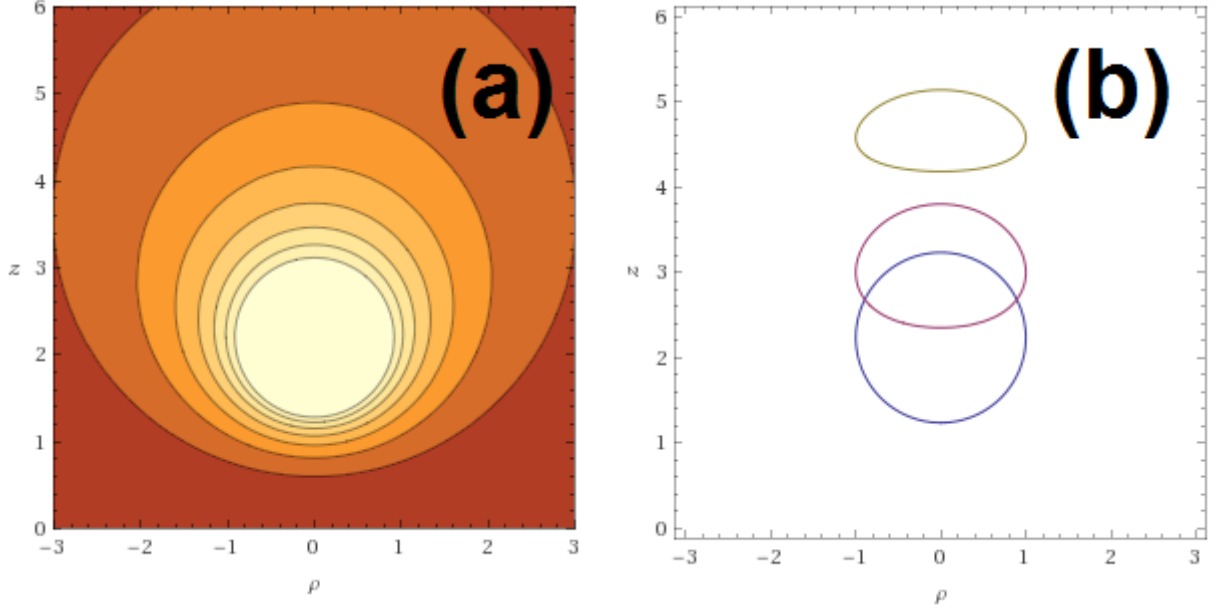
Figure 10: (a) The distribution for $\bar{\Phi}\left(\bar{\mathbf{r}}\right)$ in the non-inertial frame where $z_0 = 2$. (b) Transformations of the PRC in the inertial frame where $z_0 = 2$ and $d = 1$; the blue, magenta, and yellow lines show the shapes when $t = 0$, $t = 2$, and $t = 4$.

which imply the observer keeps standing at $\bar{\mathbf{r}} = z_0\hat{\mathbf{z}}$. Furthermore, the speed of the light measured by the observer would be changed to

$$\frac{\bar{c}}{c} = \frac{\bar{z}}{z_0}. \tag{73}$$

Interestingly $\bar{c}$ becomes zero when $\bar{z} = 0$, and it is strongly related to the event horizon of the general relativity.

In this non-inertial frame, Maxwell equation is given by

$$\bar{\boldsymbol{\nabla}} \cdot \left(\frac{\bar{\mathbf{E}}}{\bar{c}}\right) = \mu_0 c \bar{\rho},$$

$$\bar{\boldsymbol{\nabla}} \times \left(\bar{c}\bar{\mathbf{B}}\right) = \mu_0 c \bar{\mathbf{J}} + \frac{\partial}{\partial \bar{t}}\left(\frac{\bar{\mathbf{E}}}{\bar{c}}\right),$$

$$\bar{\mathbf{E}} = -\bar{\boldsymbol{\nabla}}\bar{\Phi} - \frac{\partial \bar{\mathbf{A}}}{\partial \bar{t}},$$

$$\bar{\mathbf{B}} = \bar{\boldsymbol{\nabla}} \times \bar{\mathbf{A}}, \tag{74}$$

which is completely different to the typical one since $\bar{c}$ is no longer constant. According to this equation, a particle, whose charge is q, at the observer's position ($\bar{\mathbf{r}} = z_0\hat{\mathbf{z}}$) induces the static field and potential as follows:

$$\frac{\bar{\mathbf{E}}\left(\bar{\mathbf{r}}\right)}{\bar{c}} = \frac{q}{4\pi\epsilon_0}\frac{4z_0^2}{c}\frac{2\bar{z}\left(\bar{x}\hat{\mathbf{x}} + \bar{y}\hat{\mathbf{y}}\right) + \left(2\bar{z}^2 - \bar{r}^2 - z_0^2\right)\hat{\mathbf{z}}}{\left[\left(\bar{r}^2 + z_0^2\right)^2 - 4z_0^2\bar{z}^2\right]^{3/2}},$$

$$\bar{\Phi}\left(\bar{\mathbf{r}}\right) = \frac{q}{4\pi\epsilon_0}\frac{1}{z_0}\frac{\bar{r}^2 + z_0^2}{\sqrt{\left(\bar{r}^2 + z_0^2\right)^2 - 4z_0^2\bar{z}^2}}. \tag{75}$$

Note that the derivation is explained in the appendix 4.5.2. Figure. 10(a) shows the equipotential surfaces are perfect spheres, and this relation can be represented as

$$\bar{x}^2 + \bar{y}^2 + \left(\bar{z} - \sqrt{z_0^2 + R_0^2} \right)^2 = R_0^2 \quad \Leftrightarrow \quad \bar{\Phi} = \frac{q}{4\pi\epsilon_0} \frac{\sqrt{z_0^2 + R_0^2}}{z_0 R_0}, \tag{76}$$

where R_0 is the radius of the equipotential surface. Now we are going to suppose an additional vector $\bar{\mathbf{R}}$ defined as

$$\bar{\mathbf{R}} \equiv \bar{x}\hat{\mathbf{x}} + \bar{y}\hat{\mathbf{y}} + \left(\bar{z} - \sqrt{z_0^2 + R_0^2} \right) \hat{\mathbf{z}}, \tag{77}$$

which yields a new spherical coordinate expressed as

$$\bar{\Theta} \equiv \cos^{-1}\left(\frac{\bar{\mathbf{R}}}{\bar{R}} \cdot \hat{\mathbf{z}} \right),$$
$$\bar{\mathbf{R}} = \bar{R} \left(\sin\bar{\Theta}\cos\bar{\phi}\hat{\mathbf{x}} + \sin\bar{\Theta}\sin\bar{\phi}\hat{\mathbf{y}} + \cos\bar{\Theta}\hat{\mathbf{z}} \right), \tag{78}$$

whose inverse transform also can be written as

$$\bar{x} = \bar{R}\sin\bar{\Theta}\cos\bar{\phi},$$
$$\bar{y} = \bar{R}\sin\bar{\Theta}\sin\bar{\phi},$$
$$\bar{z} = \bar{R}\cos\bar{\Theta} + \sqrt{z_0^2 + R_0^2}. \tag{79}$$

By substituting this coordinate for Eq. (75), the field $\bar{\mathbf{E}}$ at $\bar{R} = R_0$ becomes really simple to express;

$$\left.\frac{\bar{\mathbf{E}}}{\bar{c}}\right|_{\bar{R}=R_0} = \frac{\mu_0 c q}{4\pi} \frac{z_0^2}{R_0^2 \left(R_0\cos\bar{\Theta} + \sqrt{z_0^2 + R_0^2} \right)^2} \left.\frac{\bar{\mathbf{R}}}{\bar{R}}\right|_{\bar{R}=R_0}. \tag{80}$$

Furthermore, by definition, another electric field $\bar{\mathbf{E}}_{\mathrm{prc}}$ induced by the PRC can be given by

$$\bar{\mathbf{E}}_{\mathrm{prc}}(\bar{\mathbf{r}}) = \left(\frac{1}{2} + \frac{1}{2}\frac{\bar{R} - R_0}{\left|\bar{R} - R_0\right|} \right) \bar{\mathbf{E}}(\bar{\mathbf{r}}), \tag{81}$$

which indicates $\bar{\mathbf{E}}_{\mathrm{prc}}$ is vanished when $\bar{R} < R_0$ and equal to the point charge's field when $\bar{R} > R_0$ as we defined. Accordingly, we can easily obtain the distribution $\bar{\rho}_{\mathrm{prc}}$, as the Gauss law in Eq. (74) satisfies

$$\int \bar{\rho}_{\mathrm{prc}}\,\mathrm{d}^3\bar{r} = \frac{1}{\mu_0 c} \oint \frac{\bar{\mathbf{E}}_{\mathrm{prc}}}{\bar{c}} \cdot \mathrm{d}\bar{\mathbf{S}}$$
$$= \frac{1}{\mu_0 c} \oint \frac{\bar{\mathbf{E}}_{\mathrm{prc}}}{\bar{c}} \cdot \frac{\bar{\mathbf{R}}}{\bar{R}} \bar{R}^2 \sin\bar{\Theta}\,\mathrm{d}\bar{\Theta}\mathrm{d}\bar{\phi}$$
$$= \begin{cases} q & \left(\bar{R} > R_0 \right), \\ 0 & \left(\bar{R} < R_0 \right), \end{cases} \tag{82}$$

and Eqs. (80) and (81) lead to

$$\lim_{\bar{R}\to R_0+0} \left[\frac{1}{\mu_0 c}\frac{\bar{\mathbf{E}}_{\mathrm{prc}}}{\bar{c}} \cdot \frac{\bar{\mathbf{R}}}{\bar{R}}\bar{R}^2 \right] = \frac{q}{4\pi} \frac{z_0^2}{\left(R_0\cos\bar{\Theta} + \sqrt{z_0^2 + R_0^2} \right)^2},$$
$$\lim_{\bar{R}\to R_0-0} \left[\frac{1}{\mu_0 c}\frac{\bar{\mathbf{E}}_{\mathrm{prc}}}{\bar{c}} \cdot \frac{\bar{\mathbf{R}}}{\bar{R}}\bar{R}^2 \right] = 0. \tag{83}$$

Therefore, $\bar{\rho}_{\mathrm{prc}}$ should be represented as

$$\therefore \bar{\rho}_{\mathrm{prc}}\left(\bar{\mathbf{r}}\right) = \frac{q}{4\pi} \frac{z_0^2}{R_0^2 \left(R_0 \cos\bar{\Theta} + \sqrt{z_0^2 + R_0^2}\right)^2} \frac{\partial}{\partial\bar{R}} \left(\frac{1}{2} + \frac{1}{2} \frac{\bar{R} - R_0}{\left|\bar{R} - R_0\right|}\right)$$

$$= \frac{q}{4\pi} \frac{z_0^2}{R_0^2 \left(R_0 \cos\bar{\Theta} + \sqrt{z_0^2 + R_0^2}\right)^2} \delta\left(\bar{R} - R_0\right), \tag{84}$$

so that the Gauss law holds. This distribution completely satisfies the conditions for PRC that we mentioned; it is *rigid* as it is time-independent, and it is *conductive* and *point-like* as it induces $\bar{\mathbf{E}}_{\mathrm{prc}}$ of Eq. (81). Figure. 10(b) shows the shape of the PRC in the inertial frame, and the shape can be described by

$$x^2 + y^2 + \left(\sqrt{z^2 - c^2 t^2} - \sqrt{z_0^2 + R_0^2}\right)^2 = R_0^2, \tag{85}$$

derived from Eq. (76). Although the shape in the inertial frame is transforming continuously, we would like to remark that the PRC is rigid as $\bar{\rho}_{\mathrm{prc}}$ is static.

4.3 Dynamics of point-like rigid conductor

Lorentz force in an inertial frame is very well-known as

$$m_q \frac{\mathrm{d}\gamma\mathbf{v}}{\mathrm{d}t} = q\mathbf{E}_{\mathrm{ext}} + q\mathbf{v} \times \mathbf{B}_{\mathrm{ext}}. \tag{86}$$

In fact, however, the more accurate Lorentz force should be given by

$$M_q \frac{\mathrm{d}\gamma\mathbf{v}}{\mathrm{d}t} = q\mathbf{E} + q\mathbf{v} \times \mathbf{B}, \tag{87}$$

where M_q is the actual mass of a point charge without considering Dirac's mass renormalization; for example, $M_e \neq m_e$ where $m_e = 9.10938356 \times 10^{-31}$ kg. Note that the history and accuracy of this formula are briefly introduced in the appendix 4.6. Accordingly, Eq. (87) and Vlasov equation will yield

$$\frac{\partial}{\partial t}\left(f\gamma\mathbf{v}\right) + \boldsymbol{\nabla} \cdot \left(f\mathbf{v}\gamma\mathbf{v}\right) + \boldsymbol{\nabla}_v \cdot \left(f\mathbf{a}\gamma\mathbf{v}\right) = f\frac{\mathrm{d}\gamma\mathbf{v}}{\mathrm{d}t}$$

$$= f\left(\frac{q}{M_q}\mathbf{E} + \frac{q}{M_q}\mathbf{v} \times \mathbf{B}\right). \tag{88}$$

By integrating the both side, we can obtain

$$\int\left[\frac{\partial}{\partial t}\left(f\gamma\mathbf{v}\right) + \boldsymbol{\nabla} \cdot \left(f\mathbf{v}\gamma\mathbf{v}\right) + \boldsymbol{\nabla}_v \cdot \left(f\mathbf{a}\gamma\mathbf{v}\right)\right]\mathrm{d}^3v = \int f\left(\frac{q}{M_q}\mathbf{E} + \frac{q}{M_q}\mathbf{v} \times \mathbf{B}\right)\mathrm{d}^3v$$

$$\Rightarrow \frac{\partial}{\partial t}\left(n\left\langle\gamma\mathbf{v}\right\rangle\right) + \boldsymbol{\nabla} \cdot \left(n\left\langle\mathbf{v}\gamma\mathbf{v}\right\rangle\right) = \frac{q}{M_q}n\mathbf{E} + \frac{q}{M_q}n\left\langle\mathbf{v}\right\rangle \times \mathbf{B}. \tag{89}$$

Now we are going to assume that $\rho\left(\mathbf{r}, t\right) = qn\left(\mathbf{r}, t\right)$; it is valid only when ρ is consist of same particles. Therefore, in the similar way, the Vlasov equation will be changed to

$$\frac{M_q}{q}\frac{\partial}{\partial t}\int \rho\left\langle\gamma\mathbf{v}\right\rangle\mathrm{d}^3r = \int \rho\mathbf{E} + \mathbf{J} \times \mathbf{B}\,\mathrm{d}^3r, \tag{90}$$

which could be called 'Lorentz force for volume charges.' We will soon present that ρ_{prc} and $\mathbf{E}_{\mathrm{prc}}$, substituted for Eq. (90), lead to very interesting results.

4.3.1 Momentum of PRC

The total momentum of PRC would be defined as

$$
\mathbf{p}_{\text{prc}}(t) \equiv \frac{M_q}{q} \int \rho_{\text{prc}} \langle \gamma \mathbf{v} \rangle_{\text{prc}} \, d^3 r \big|_{t=\text{const}} .
\tag{91}
$$

Unfortunately, we can not calculate this integral directly, as it is difficult to describe ρ_{prc} in the inertial frame. Hence, based on Eq. (112) and the appendix 4.5.1, we will consider non-inertial Lorentz transform for the density and current as follows:

$$
\begin{aligned}
\rho_{\text{prc}} &= \Gamma \bar{\rho}_{\text{prc}} \\
&= q n_{\text{prc}}, \\
\mathbf{J}_{\text{prc}} &= \Gamma V \bar{\rho}_{\text{prc}} \hat{\mathbf{z}} \\
&= q n_{\text{prc}} \langle \mathbf{v} \rangle_{\text{prc}}, \\
\Rightarrow \langle \mathbf{v} \rangle_{\text{prc}} &= V \hat{\mathbf{z}} \\
&= \frac{c^2 t}{z} \hat{\mathbf{z}}.
\end{aligned}
\tag{92}
$$

As the PRC is rigid, the fluid velocity $\langle \mathbf{v} \rangle_{\text{prc}}$ satisfies

$$
\begin{aligned}
\langle \gamma \mathbf{v} \rangle_{\text{prc}} &= \frac{\langle \mathbf{v} \rangle_{\text{prc}}}{\sqrt{1 - \langle \mathbf{v} \rangle_{\text{prc}}^2 / c^2}} \\
&= \frac{c^2 t}{\sqrt{z^2 - c^2 t^2}} \hat{\mathbf{z}} \\
&= \frac{c^2 t}{\bar{z}} \hat{\mathbf{z}}.
\end{aligned}
\tag{93}
$$

Further, on the t-constant plane of the space-time, the infinitesimal variables (given by Eq. (108)) should be represented as

$$
\begin{aligned}
c dt |_{t=\text{const}} &= \Gamma \, \bar{c} d\bar{t} |_{t=\text{const}} + \Gamma \frac{V}{c} \, d\bar{z} |_{t=\text{const}} \\
&= 0, \\
dz |_{t=\text{const}} &= \Gamma \, d\bar{z} |_{t=\text{const}} + \Gamma \frac{V}{c} \, \bar{c} d\bar{t} |_{t=\text{const}} \\
&= \frac{1}{\Gamma} \, d\bar{z} |_{t=\text{const}}, \\
\Rightarrow \rho_{\text{prc}} \, d^3 r |_{t=\text{const}} &= \bar{\rho}_{\text{prc}} \, d^3 \bar{r} |_{t=\text{const}} .
\end{aligned}
\tag{94}
$$

Therefore, Eq. (91) can be integrated now;

$$
\begin{aligned}
\mathbf{p}_{\text{prc}}(t) &= \frac{M_q}{q} \int \bar{\rho}_{\text{prc}} \frac{c^2 t}{\bar{z}} \hat{\mathbf{z}} \, d^3 \bar{r} \big|_{t=\text{const}} \\
&= \frac{M_q c^2 t}{4\pi} \hat{\mathbf{z}} \int \frac{z_0^2}{R_0^2 \left(R_0 \cos \bar{\Theta} + \sqrt{z_0^2 + R_0^2} \right)^3} \delta \left(\bar{R} - R_0 \right) d^3 \bar{r} \\
&= \frac{M_q c^2 t}{z_0} \sqrt{1 + \frac{R_0^2}{z_0^2}} \hat{\mathbf{z}}.
\end{aligned}
\tag{95}
$$

34

If we suppose the velocity of the observer defined as $\mathbf{u} \equiv \mathrm{d}\boldsymbol{\chi}/\mathrm{d}\tau$ where τ is the proper time, $\mathbf{p}_{\mathrm{prc}}$ will be rewritten as

$$
\begin{aligned}
\mathbf{p}_{\mathrm{prc}} &= M_q \mathbf{u} \sqrt{1 + \left| \frac{\mathrm{d}\mathbf{u}}{\mathrm{d}t} \right|^2 \frac{R_0^2}{c^4}}, \\
\Rightarrow |\mathbf{p}_{\mathrm{prc}}| &> |M_q \mathbf{u}|.
\end{aligned}
\tag{96}
$$

As we mentioned, $\mathbf{p}_{\mathrm{prc}}$ is the momentum of the PRC which can not be distinguished from the point charge whose momentum is $M_q \mathbf{u}$. Then, what does it mean that $|\mathbf{p}_{\mathrm{prc}}|$ is higher than $|M_q \mathbf{u}|$? It means that some extra energy is required to generate the PRC which looks like the point charge. In the next section, it will be presented that this extra energy is strongly related to the radiation reaction for the PRC.

4.3.2 Self-force of PRC

The radiation reaction is predicted to be included in the self-force of a charged particle. The problem is that the fields induced by a point charge can not be defined at the charge's position. On the other hand, in the similar way to derive $\mathbf{p}_{\mathrm{prc}}$, the self-force of the PRC can be obtained from Eqs. (81) and (90) as follows:

$$
\begin{aligned}
\rho \frac{E_z}{c} + \frac{J_x}{c} B_y - \frac{J_y}{c} B_x &= \Gamma \bar{\rho} \frac{\bar{E}_z}{\bar{c}}, \\
\Rightarrow \int \left[\rho_{\mathrm{prc}} \mathbf{E}_{\mathrm{prc}} + \mathbf{J}_{\mathrm{prc}} \times \mathbf{B}_{\mathrm{prc}} \right]_z \mathrm{d}^3 r &= c \int \left[\bar{\rho}_{\mathrm{prc}} \frac{\bar{\mathbf{E}}_{\mathrm{prc}}}{\bar{c}} \right]_z \mathrm{d}^3 \bar{r} \\
&= \frac{qc}{8\pi} \int \frac{z_0^2}{R_0^2 \left(R_0 \cos\bar{\Theta} + \sqrt{z_0^2 + R_0^2} \right)^2} \frac{\bar{E}_z}{\bar{c}} \frac{\partial}{\partial \bar{R}} \left(\frac{1}{2} + \frac{1}{2} \frac{\bar{R} - R_0}{|\bar{R} - R_0|} \right)^2 \mathrm{d}^3 \bar{r}.
\end{aligned}
\tag{97}
$$

Fortunately, it is really easy to confirm that

$$
\int \frac{\partial}{\partial \bar{R}} \left(\frac{1}{2} + \frac{1}{2} \frac{\bar{R} - R_0}{|\bar{R} - R_0|} \right)^2 \mathrm{d}\bar{R} = \int \delta \left(\bar{R} - R_0 \right) \mathrm{d}\bar{R}.
\tag{98}
$$

Therefore, with Eq. (80), we can obtain

$$
\begin{aligned}
\int \rho_{\mathrm{prc}} \mathbf{E}_{\mathrm{prc}} + \mathbf{J}_{\mathrm{prc}} \times \mathbf{B}_{\mathrm{prc}} \, \mathrm{d}^3 r &= \frac{\mu_0 q^2 c^2}{32\pi^2} \hat{\mathbf{z}} \int \frac{z_0^4 \cos\bar{\Theta}}{R_0^4 \left(R_0 \cos\bar{\Theta} + \sqrt{z_0^2 + R_0^2} \right)^4} R_0^2 \sin\bar{\Theta} \, \mathrm{d}\bar{\Theta} \mathrm{d}\bar{\phi} \\
&= -\frac{\mu_0 q^2}{6\pi R_0} \frac{c^2}{z_0} \sqrt{1 + \frac{R_0^2}{z_0^2}} \hat{\mathbf{z}} \\
&= -\frac{\mu_0 q^2}{6\pi R_0} \frac{\mathrm{d}\mathbf{u}}{\mathrm{d}t} \sqrt{1 + \left| \frac{\mathrm{d}\mathbf{u}}{\mathrm{d}t} \right|^2 \frac{R_0^2}{c^4}},
\end{aligned}
\tag{99}
$$

which has the same square root term as Eq. (96) has. As far as we know, this force has not been published yet. Probably it is because, most of researchers previously supposed that $R_0 \to 0$,

before they calculate the self-force. In contrast, here we would like to suggest an interesting assumption, that R_0 might be quite longer than we thought;

$$\left|\frac{\mathrm{d}\mathbf{u}}{\mathrm{d}t}\right|\frac{R_0}{c^2} \quad \gg \quad 1,$$

$$\rightarrow \int \rho_{\mathrm{prc}}\mathbf{E}_{\mathrm{prc}} + \mathbf{J}_{\mathrm{prc}} \times \mathbf{B}_{\mathrm{prc}}\, \mathrm{d}^3 r \quad = \quad -\frac{\mu_0 q^2}{6\pi R_0}\frac{\mathrm{d}\mathbf{u}}{\mathrm{d}t}\left|\frac{\mathrm{d}\mathbf{u}}{\mathrm{d}t}\right|\frac{R_0}{c^2}$$

$$= \quad -\frac{\mu_0 q^2 \gamma^6 |\mathbf{a}|^2}{6\pi c^2}\hat{\mathbf{z}}, \tag{100}$$

where $\gamma^2 = 1 + u^2/c^2$, and $\mathbf{a} = \mathrm{d}^2\boldsymbol{\chi}/\mathrm{d}t^2$. Surprisingly, the force became equivalent to Larmor formula. (Actually, this result can be also induced even when R_0 is infinitesimal, if the acceleration is high enough.) Definitely it implies that *the self-force of Eq. (99) includes the radiation reaction*, and we believe that *it is why generating PRC requires more momentum* $|\mathbf{p}_{\mathrm{prc}}|$ *than point charges' one* $|M_q\mathbf{u}|$.

4.3.3 External electric field

Finally, it is time to face the fundamental question: what external field can drive the constantly accelerating PRC? In fact, it is very difficult to answer, because the charge distribution of PRC would not be given by ρ_{prc} any longer, as external fields affect the conductive condition. Despite this, however, we will assume that Eq. (90) could be (approximately) represented as

$$\frac{M_q}{q}\frac{\partial}{\partial t}\int \rho_{\mathrm{prc}}\langle\gamma\mathbf{v}\rangle_{\mathrm{prc}}\, \mathrm{d}^3 r \quad \simeq \quad \int \rho_{\mathrm{prc}}\mathbf{E}_{\mathrm{prc}} + \mathbf{J}_{\mathrm{prc}} \times \mathbf{B}_{\mathrm{prc}}\, \mathrm{d}^3 r + \int \rho_{\mathrm{prc}}\mathbf{E}_{\mathrm{ext}}\, \mathrm{d}^3 r. \tag{101}$$

At this moment, it is reasonable to suppose $\mathbf{E}_{\mathrm{ext}}$ is uniform and time-independent. Accordingly, with Eqs. (96) and (99), this equation will be changed to

$$M_q\frac{\mathrm{d}\mathbf{u}}{\mathrm{d}t}\sqrt{1 + \left|\frac{\mathrm{d}\mathbf{u}}{\mathrm{d}t}\right|^2\frac{R_0^2}{c^4}} \quad \simeq \quad -\frac{\mu_0 q^2}{6\pi R_0}\frac{\mathrm{d}\mathbf{u}}{\mathrm{d}t}\sqrt{1 + \left|\frac{\mathrm{d}\mathbf{u}}{\mathrm{d}t}\right|^2\frac{R_0^2}{c^4}} + q\mathbf{E}_{\mathrm{ext}}. \tag{102}$$

If we define a new effective mass as

$$m_{\mathrm{eff}} \quad \equiv \quad \left(M_q + \frac{\mu_0 q^2}{6\pi R_0}\right)\sqrt{1 + \left|\frac{\mathrm{d}\mathbf{u}}{\mathrm{d}t}\right|^2\frac{R_0^2}{c^4}}$$

$$= \quad m_q\sqrt{1 + \left|\frac{\mathrm{d}\mathbf{u}}{\mathrm{d}t}\right|^2\frac{R_0^2}{c^4}}, \tag{103}$$

we can finally obtain

$$\therefore m_{\mathrm{eff}}\frac{\mathrm{d}\mathbf{u}}{\mathrm{d}t} \quad \simeq \quad q\mathbf{E}_{\mathrm{ext}}, \tag{104}$$

which is the motion equation for the constantly accelerating PRC driven by constant electric fields. By definition, m_{eff} becomes heavier than m_q as the external field becomes stronger. Therefore, we conclude that this extra mass represents the radiation reaction in the constant acceleration. (Note that

$$\lim_{R_0 \to 0} m_{\mathrm{eff}} \quad = \quad \infty, \tag{105}$$

36

and it means none of fields can accelerate zero-radius PRC, which might be equivalent to ideal point charges.)

4.4 Discussion

If Eq. (104) is rigorous, it is possible to measure R_0 by the experiments, as Eq. (104) can be rewritten as

$$\frac{R_0^2}{c^4} \;=\; \left(\frac{|q\mathbf{E}_{\text{ext}}|^2}{|m_q \mathrm{d}\mathbf{u}/\mathrm{d}t|^2} - 1 \right) \Big/ \left| \frac{\mathrm{d}\mathbf{u}}{\mathrm{d}t} \right|^2. \tag{106}$$

All quantities in the right side can be determined. Once we obtain R_0, the actual kinetic mass M_q also can be found;

$$M_q \;=\; m_q - \frac{\mu_0 q^2}{6\pi R_0}. \tag{107}$$

Of course, this discussion is valid only when the real particle satisfies the PRC model.

4.5 Non-inertial frame

Understanding the non-inertial frame requires a lot of derivations and explanations. In this section we suppose that $\mathrm{d}\bar{r}^2 - \bar{c}^2 \mathrm{d}\bar{t}^2 = \mathrm{d}r^2 - c^2 \mathrm{d}t^2$ as an axiom-like condition (but it can be deductively induced from the chain rule). This supposition yields

$$\begin{bmatrix} \bar{c}\mathrm{d}\bar{t} \\ \mathrm{d}\bar{x} \\ \mathrm{d}\bar{y} \\ \mathrm{d}\bar{z} \end{bmatrix} = \begin{bmatrix} \Gamma & 0 & 0 & -\Gamma V/c \\ 0 & 1 & 0 & 0 \\ 0 & 0 & 1 & 0 \\ -\Gamma V/c & 0 & 0 & \Gamma \end{bmatrix} \begin{bmatrix} c\mathrm{d}t \\ \mathrm{d}x \\ \mathrm{d}y \\ \mathrm{d}z \end{bmatrix}, \tag{108}$$

which implies

$$\begin{aligned} \Gamma &= \frac{\partial \bar{z}}{\partial z} \\ &= \frac{\bar{c}}{c} \frac{\partial \bar{t}}{\partial t}, \\ \Gamma \frac{V}{c} &= -\frac{1}{c} \frac{\partial \bar{z}}{\partial t} \\ &= -\bar{c} \frac{\partial \bar{t}}{\partial z}. \end{aligned} \tag{109}$$

Accordingly, two differential equations for V and $\bar{c}$ can be obtained as

$$\begin{aligned} \frac{\partial^2 \bar{z}}{\partial z \partial t} &= \frac{\partial^2 \bar{z}}{\partial t \partial z}, \\ \Rightarrow \frac{V}{c^2} \frac{\partial V}{\partial t} + \frac{\partial V}{\partial z} &= 0, \end{aligned} \tag{110}$$

and

$$\begin{aligned} \frac{\partial^2 \bar{t}}{\partial z \partial t} &= \frac{\partial^2 \bar{t}}{\partial t \partial z}, \\ \Rightarrow \Gamma^2 \frac{\partial V}{\partial t} + \Gamma^2 V \frac{\partial V}{\partial z} &= \frac{V}{\bar{c}} \frac{\partial \bar{c}}{\partial t} + \frac{c^2}{\bar{c}} \frac{\partial \bar{c}}{\partial z}. \end{aligned} \tag{111}$$

37

The simplest solution of Eq. (110) is that

$$V(\mathbf{r}, t) = \frac{c^2 t}{z}, \tag{112}$$

which is the velocity of the constantly accelerating frame, as Eq. (71) satisfies $d\chi_z/dt = c^2 t/\chi_z$. By substituting Eq. (112) for Eq. (111), we also obtain

$$\frac{\bar{c}(\mathbf{r}, t)}{c} = \frac{\sqrt{z^2 - c^2 t^2}}{z_0}. \tag{113}$$

Therefore, from Eq. (109), the final results can be derived as Eqs. (72) and (73).

4.5.1 Other variables in non-inertial frames

In this section, we will just suggest some outcomes without derivations. First, based on Eq. (108), the transform for electromagnetic fields is given by

$$\frac{\bar{E}_x}{\bar{c}} = \Gamma \frac{E_x}{c} - \Gamma \frac{V}{c} B_y, \quad \frac{\bar{E}_y}{\bar{c}} = \Gamma \frac{E_y}{c} + \Gamma \frac{V}{c} B_x, \quad \frac{\bar{E}_z}{\bar{c}} = \frac{E_z}{c},$$
$$\bar{B}_x = \Gamma B_x + \Gamma \frac{V}{c} \frac{E_y}{c}, \quad \bar{B}_y = \Gamma B_y - \Gamma \frac{V}{c} \frac{E_x}{c}, \quad \bar{B}_z = B_z. \tag{114}$$

Second, the density and current will be represented as

$$\begin{bmatrix} \bar{\rho} \\ \bar{J}_x/\bar{c} \\ \bar{J}_y/\bar{c} \\ \bar{J}_z/\bar{c} \end{bmatrix} = \begin{bmatrix} \Gamma & 0 & 0 & -\Gamma V/c \\ 0 & 1 & 0 & 0 \\ 0 & 0 & 1 & 0 \\ -\Gamma V/c & 0 & 0 & \Gamma \end{bmatrix} \begin{bmatrix} \rho \\ J_x/c \\ J_y/c \\ J_z/c \end{bmatrix}. \tag{115}$$

At last, as the chain rule always holds, $\bar{\partial}_\mu$ should satisfy

$$\begin{bmatrix} \frac{1}{\bar{c}} \frac{\partial}{\partial \bar{t}} \\ \frac{\partial}{\partial \bar{z}} \end{bmatrix} = \begin{bmatrix} \Gamma & \Gamma \frac{V}{c} \\ \Gamma \frac{V}{c} & \Gamma \end{bmatrix} \begin{bmatrix} \frac{1}{c} \frac{\partial}{\partial t} \\ \frac{\partial}{\partial z} \end{bmatrix}. \tag{116}$$

Note that it is easy to derive Eq. (74) from the aboves.

4.5.2 Fields of constantly accelerating charged particles

The retarded time t_r for a point charge, whose motion satisfies Eq. (71), is represented as

$$ct_r = ct - |\mathbf{r} - \boldsymbol{\chi}(t_r)|, \tag{117}$$

which can be actully solved as

$$ct_r = \frac{ct\left(c^2 t^2 - r^2 - z_0^2\right) + z\sqrt{\left(c^2 t^2 - r^2 - z_0^2\right)^2 + 4z_0^2\left(c^2 t^2 - z^2\right)}}{2\left(c^2 t^2 - z^2\right)}. \tag{118}$$

Furthermore, the inverse transform of Eq. (72) is written as

$$
\begin{aligned}
ct &= \bar{z}\sinh\left(\frac{c\bar{t}}{z_0}\right), \\
x &= \bar{x}, \\
y &= \bar{y}, \\
z &= \bar{z}\cosh\left(\frac{c\bar{t}}{z_0}\right).
\end{aligned}
\tag{119}
$$

If we substitute Eqs. (114), (118), and (119) for the LiénardWiechert field, which is given by

$$
\mathbf{E}\left(\mathbf{r},t\right) = \frac{q}{4\pi\epsilon_0}\frac{\mathbf{n}_r - \boldsymbol{\beta}_r}{\left|\mathbf{r}-\boldsymbol{\chi}_r\right|^2 \gamma_r^2\left(1-\mathbf{n}_r\cdot\boldsymbol{\beta}_r\right)^3} + \frac{q/c^2}{4\pi\epsilon_0}\frac{\mathbf{n}_r\times\left[\left(\mathbf{n}_r-\boldsymbol{\beta}_r\right)\times\mathbf{a}_r\right]}{\left|\mathbf{r}-\boldsymbol{\chi}_r\right|\left(1-\mathbf{n}_r\cdot\boldsymbol{\beta}_r\right)^3},
\tag{120}
$$

we can finally obtain Eq. (75) [62].

4.6 Lorentz force

The momentum conservation of electrodynamics should satisfy the Maxwell stress formula, which is given by

$$
\rho\mathbf{E} + \mathbf{J}\times\mathbf{B} + \frac{\partial}{\partial t}\left(\epsilon_0\mathbf{E}\times\mathbf{B}\right) + \boldsymbol{\nabla}\left(\frac{\epsilon_0 E^2}{2}+\frac{B^2}{2\mu_0}\right) = \boldsymbol{\nabla}\cdot\left(\epsilon_0\mathbf{E}\mathbf{E}+\frac{1}{\mu_0}\mathbf{B}\mathbf{B}\right).
\tag{121}
$$

The integral for this equation over infinite intervals will yields

$$
\int_\infty \rho\mathbf{E} + \mathbf{J}\times\mathbf{B}\,\mathrm{d}^3r + \epsilon_0\frac{\partial}{\partial t}\int_\infty \mathbf{E}\times\mathbf{B}\,\mathrm{d}^3r = 0,
\tag{122}
$$

because none of signals can reach the edge of this interval. Hence, Lorentz realized the particle motion should satisfy

$$
\begin{aligned}
\int_\infty \rho\mathbf{E} + \mathbf{J}\times\mathbf{B}\,\mathrm{d}^3r &= \frac{\mathrm{d}}{\mathrm{d}t}\sum_i^\infty \mathbf{p}_i, \\
\therefore M_q\frac{\mathrm{d}\gamma\mathbf{v}}{\mathrm{d}t} &= q\mathbf{E} + q\mathbf{v}\times\mathbf{B} \\
&\neq q\mathbf{E}_{\mathrm{ext}} + q\mathbf{v}\times\mathbf{B}_{\mathrm{ext}}.
\end{aligned}
\tag{123}
$$

so that the total momentum of systems is conserved. Since Lorentz found the self-force of point charges is not zero, Dirac suggested the modified motion equation, which is written as

$$
M_q\frac{\mathrm{d}u^\mu}{\mathrm{d}\tau} = qu_\nu F_{\mathrm{ext}}^{\mu\nu} - \frac{\mu_0 q^2}{N\pi R_0}\frac{\mathrm{d}u^\mu}{\mathrm{d}\tau} + \frac{\mu_0 q^2}{6\pi c}\left(\frac{\mathrm{d}^2 u^\mu}{\mathrm{d}\tau^2}-\frac{u^\mu}{c^2}\frac{\mathrm{d}u_\nu}{\mathrm{d}\tau}\frac{\mathrm{d}u^\nu}{\mathrm{d}\tau}\right) + O\left(R_0\right),
\tag{124}
$$

where N is six or eight. The problem was that the second term of the right side diverges as $R_0 \to 0$. Dirac tried to renormalize the mass by defining a new mass m_q $(\equiv M_q + \mu_0 q^2/N\pi R_0)$, and neglected the high-order terms;

$$
\therefore m_q\frac{\mathrm{d}u^\mu}{\mathrm{d}\tau} = qu_\nu F_{\mathrm{ext}}^{\mu\nu} + \frac{\mu_0 q^2}{6\pi c}\left(\frac{\mathrm{d}^2 u^\mu}{\mathrm{d}\tau^2}-\frac{u^\mu}{c^2}\frac{\mathrm{d}u_\nu}{\mathrm{d}\tau}\frac{\mathrm{d}u^\nu}{\mathrm{d}\tau}\right),
\tag{125}
$$

whose last term represents the Larmor formula. Unfortunately, Dirac's formula has some problems, and Landau and Lifshitz [63] changed Eq. (125) slightly as follows:

$$
\begin{aligned}
\frac{\mathrm{d}u^\mu}{\mathrm{d}\tau} &\approx \frac{q}{m_q} u_\nu F_{\text{ext}}^{\mu\nu}, \\
\frac{\mathrm{d}^2 u^\mu}{\mathrm{d}\tau^2} &\approx \frac{q}{m_q} \frac{\mathrm{d}u_\nu}{\mathrm{d}\tau} F_{\text{ext}}^{\mu\nu} + \frac{q}{m_q} u_\nu \frac{\mathrm{d}F_{\text{ext}}^{\mu\nu}}{\mathrm{d}\tau} \\
&\approx \frac{q^2}{m_q^2} u^\lambda F_{\nu\lambda}^{\text{ext}} F_{\text{ext}}^{\mu\nu} + \frac{q}{m_q} u_\nu u_\lambda \partial^\lambda F_{\text{ext}}^{\mu\nu}, \\
\Rightarrow m_q \frac{\mathrm{d}u^\mu}{\mathrm{d}\tau} &= q u_\nu F_{\text{ext}}^{\mu\nu} + \frac{\mu_0 q^2}{6\pi c} \left(\frac{\mathrm{d}^2 u^\mu}{\mathrm{d}\tau^2} - \frac{u^\mu}{c^2} \frac{\mathrm{d}u_\nu}{\mathrm{d}\tau} \frac{\mathrm{d}u^\nu}{\mathrm{d}\tau} \right) \\
&\approx q u_\nu F_{\text{ext}}^{\mu\nu} + \frac{\mu_0 q^3}{6\pi m_q c} \left(\frac{q}{m_q} u^\lambda F_{\nu\lambda}^{\text{ext}} F_{\text{ext}}^{\mu\nu} + u_\nu u_\lambda \partial^\lambda F_{\text{ext}}^{\mu\nu} - \frac{q u^\mu}{m_q c^2} u_\lambda F_{\text{ext}}^{\nu\lambda} u^\sigma F_{\nu\sigma}^{\text{ext}} \right).
\end{aligned}
\tag{126}
$$

As far as we know, this equation solves most problems of Eq. (125), *except for the energy conservation of a constantly accelerating charged particle* [64].

V   Appendix: Interpolation theory

Suppose a sequence f_n and a function $f(x)$ whose relation is represented as

$$f(n\Delta x) = f_n. \tag{127}$$

The practical purpose of the interpolation would be to predict $f(x)$ from given f_n. In this document an interpolation method, which uses the cardinal basis spline (CBS), will be introduced.

5.1   Cardinal Basis Spline (CBS)

This method assumes that $f(x)$ is an analytic function. By definition, analytic functions must satisfy the Taylor series which is given by

$$\begin{aligned} f(x+h) &= f(x) + h\dot{f}(x) + \frac{h^2}{2}\ddot{f}(x) + \cdots \\ &= \sum_{l=0}^{\infty} \frac{h^l}{l!}\frac{\partial^l}{\partial x^l}f(x). \end{aligned} \tag{128}$$

From the above formula, we can obtain

$$\begin{aligned} f_0 &= f(x-x) \\ &= f(x) - x\dot{f}(x) + \frac{x^2}{2}\ddot{f}(x) + \cdots, \\ f_1 &= f(x+\Delta x - x) \\ &= f(x) + (\Delta x - x)\dot{f}(x) + \frac{(\Delta x - x)^2}{2}\ddot{f}(x) + \cdots, \end{aligned} \tag{129}$$

and their combination yields

$$(\Delta x - x)f_0 + xf_1 = \Delta x\left[f(x) + \frac{x(\Delta x - x)}{2}\ddot{f}(x) + \cdots\right]. \tag{130}$$

If we neglect the second and higher order derivatives, the final result will be written as

$$f(x) \simeq \left(1 - \frac{x}{\Delta x}\right)f_0 + \frac{x}{\Delta x}f_1. \tag{131}$$

This equation indicates a first-order interpolation for $f(x)$ where $0 < x < \Delta x$. In the same way, if we consider every derivatives, we can obtain the infinite-order result called WhittakerShannon interpolation;

$$\therefore f(x) = \sum_{n=-\infty}^{\infty} \text{sinc}\left(\pi\left(\frac{x}{\Delta x} - n\right)\right)f_n. \tag{132}$$

$\text{sinc}(x)$ is the sinc function, defined as $\text{sinc}(x) \equiv \sin(x)/x$ and $\text{sinc}(0) \equiv 1$. Furthermore, the sinc function is called the infinite-order CBS when it is used as a spline (like Eq. (132) shows).

5.1.1 Perfect reconstruction

The sinc function (or the infinite-order CBS) has an interesting characteristic, which is similar to the orthogonality and given by

$$\sum_{n=-\infty}^{\infty} \operatorname{sinc}\left(\pi\left(n-a\right)\right)\operatorname{sinc}\left(\pi\left(n-b\right)\right) = \operatorname{sinc}\left(\pi\left(a-b\right)\right),$$

$$\int_{-\infty}^{\infty} \operatorname{sinc}\left(\pi\left(\frac{x}{\Delta x}-a\right)\right)\operatorname{sinc}\left(\pi\left(\frac{x}{\Delta x}-b\right)\right)\mathrm{d}x = \operatorname{sinc}\left(\pi\left(a-b\right)\right)\Delta x, \qquad (133)$$

where a and b are arbitrary real numbers. Accordingly if we calculate another sequence f'_m, which satisfies $f\left(m\Delta x + h\right) = f'_m$, from f_n by considering

$$f'_m = \sum_{n=-\infty}^{\infty} \operatorname{sinc}\left(\pi\left(m+\frac{h}{\Delta x}-n\right)\right)f_n, \qquad (134)$$

it is possible to obtain f_n inversely from f'_m as well;

$$\sum_{m=-\infty}^{\infty} \operatorname{sinc}\left(\pi\left[l-\frac{h}{\Delta x}-m\right]\right)f'_m = \sum_{n=-\infty}^{\infty}\sum_{m=-\infty}^{\infty} \operatorname{sinc}\left(\pi\left[l-\frac{h}{\Delta x}-m\right]\right)\operatorname{sinc}\left(\pi\left[m+\frac{h}{\Delta x}-n\right]\right)f_n$$

$$= \sum_{n=-\infty}^{\infty} \operatorname{sinc}\left(\pi\left(l-n\right)\right)f_n,$$

$$\Rightarrow f_n = \sum_{m=-\infty}^{\infty} \operatorname{sinc}\left(\pi\left(n-\frac{h}{\Delta x}-m\right)\right)f'_m. \qquad (135)$$

This characteristic is also called the perfect reconstruction, and it implies that sequences do not lose their information when they are interpolated by the infinite-order CBS.

5.1.2 Finite-order CBS

Although Eq. (132) prevent a loss of the information, unfortunately, it is not practical because it requires every f_n in the space. In this section we present the finite-order CBS which enables practical interpolations.

Suppose that $S_N(x)$ is N-order CBS, which is represented as

$$
\begin{aligned}
S_0(x) &= \begin{cases} 1 & (|x| < 1/2), \\ 0 & (|x| > 1/2), \end{cases} \\[2mm]
S_1(x) &= \begin{cases} 1 - |x| & (|x| \leq 1), \\ 0 & (|x| > 1), \end{cases} \\[2mm]
S_2(x) &= \begin{cases} (1 - |x|)(1 + |x|) & (|x| < 1/2), \\ (2 - |x|)(1 - |x|)/2 & (1/2 < |x| < 3/2), \\ 0 & (|x| > 3/2), \end{cases} \\[2mm]
S_3(x) &= \begin{cases} (2 - |x|)(1 - |x|)(1 + |x|)/2 & (|x| \leq 1), \\ (3 - |x|)(2 - |x|)(1 - |x|)/6 & (1 < |x| \leq 2), \\ 0 & (|x| > 2), \end{cases} \\[2mm]
S_\infty(x) &= \operatorname{sinc}(\pi x). \tag{136}
\end{aligned}
$$

An approximation of the function $f(x)$ can be obtained from $S_N(x)$ except for $S_\infty(x)$ as follows:

$$
f(x) \simeq \sum_{n=-\infty}^{\infty} S_N\left(\frac{x}{\Delta x} - n\right) f_n. \tag{137}
$$

This equation is a more general expression for the CBS interpolation. The information loss decreases as the order N increases, but the number of required f_n is also raised to $N + 1$ in order to determine $f(x)$ within Δx range. The best practical way would be matching orders of CBS and differential equations to solve. For example, $S_2(x)$ will be the appropriate spline to solve the numerical Poisson equation.

5.1.3 Multi-dimension

The previous derivation could be applied to f_{nm}, which satisfies $f(n\Delta x, m\Delta y) = f_{nm}$. The two-dimensional (2D) Taylor series for $f(x, y)$ is given by

$$
\begin{aligned}
f(x + h_x, y + h_y) &= \sum_{l=0}^{\infty} \frac{1}{l!}\left(h_x \frac{\partial}{\partial x} + h_y \frac{\partial}{\partial y}\right)^l f(x, y) \\
&= f(x, y + h_y) + h_x \left.\frac{\partial f}{\partial x}\right|_{x, y+h_y} + \frac{h_x^2}{2} \left.\frac{\partial^2 f}{\partial x^2}\right|_{x, y+h_y} + \cdots \\
&= f(x + h_x, y) + h_y \left.\frac{\partial f}{\partial y}\right|_{x+h_x, y} + \frac{h_y^2}{2} \left.\frac{\partial^2 f}{\partial y^2}\right|_{x+h_x, y} + \cdots. \tag{138}
\end{aligned}
$$

Owing to the independence of x and y in this 2D series, we can easily obtain

$$
\begin{aligned}
f(x, y + h_y) &= \sum_{n=-\infty}^{\infty} \operatorname{sinc}\left(\pi\left(\frac{x}{\Delta x} - n\right)\right) f(n\Delta x, y + h_y), \\
f(x + h_x, y) &= \sum_{m=-\infty}^{\infty} \operatorname{sinc}\left(\pi\left(\frac{y}{\Delta y} - m\right)\right) f(x + h_x, m\Delta y), \tag{139}
\end{aligned}
$$

and a combination of the both leads to

$$\therefore f(x,y) = \sum_{n=-\infty}^{\infty} \sum_{m=-\infty}^{\infty} \mathrm{sinc}\left(\pi\left(\frac{x}{\Delta x} - n\right)\right) \mathrm{sinc}\left(\pi\left(\frac{y}{\Delta y} - m\right)\right) f_{nm}. \qquad (140)$$

Moreover, such as Eq. (137), this result could be also generalized as

$$f(x,y) \simeq \sum_{n=-\infty}^{\infty} \sum_{m=-\infty}^{\infty} S_N\left(\frac{x}{\Delta x} - n\right) S_M\left(\frac{y}{\Delta y} - m\right) f_{nm}. \qquad (141)$$

For 2D, accordingly, the number of required f_{nm} will be $(N+1)\times(M+1)$ to determine $f(x,y)$ within $\Delta x \Delta y$ range.

5.2 Numerical Analysis

Once we assume that it is possible to use the infinite-order CBS ideally, every numerical problems become analytic. It is because we can just focus on $f(x)$ without considering f_n. From now on 'derivatives of sequences,' which were not supposed to be defined, will be represented as

$$\dot{f}(x) = \sum_{n=-\infty}^{\infty} \frac{\partial}{\partial x}\left[\mathrm{sinc}\left(\pi\left(\frac{x}{\Delta x} - n\right)\right)\right] f_n,$$

$$\dot{f}_n \equiv \dot{f}(n\Delta x),$$

$$\Rightarrow \dot{f}(x) = \sum_{n=-\infty}^{\infty} \mathrm{sinc}\left(\pi\left(\frac{x}{\Delta x} - n\right)\right) \dot{f}_n, \qquad (142)$$

and summations and integrals become equivalent as follows:

$$\int_{-\infty}^{\infty} f(x)\,\mathrm{d}x = \sum_{n=-\infty}^{\infty} f_n \Delta x,$$

$$\int_{-\infty}^{\infty} f(x)\,g(x)\,\mathrm{d}x = \sum_{n=-\infty}^{\infty} f_n g_n \Delta x. \qquad (143)$$

Furthermore, there are other (physical) advantages of using $f(x)$ rather than f_n. Just one example will be presented.

5.2.1 Point charge

Normally, It is quite difficult to define a point charge in the simulation domain. It is because the simulation can not suppose something smaller than Δx, even though the actual size of a point charge is zero. Besides, the position of the charge does not have to be discontinuous. To get straight to the point: the density of a point charge in the domain should satisfies

$$\rho_{\mathrm{single}}(x) = \frac{q}{\Delta x}\,\mathrm{sinc}\left(\pi\left(\frac{x}{\Delta x} - \frac{X}{\Delta x}\right)\right), \qquad (144)$$

(where X is the position of the charge). Obviously, the integral of this equation yields the total charge q. Now we need the total electric field $\mathbf{E}$ induced by $\mathbf{E}_n$ of the domain;

$$\mathbf{E}(x) = \sum_{n=-\infty}^{\infty} \mathrm{sinc}\left(\pi\left(\frac{x}{\Delta x} - n\right)\right) \mathbf{E}_n. \qquad (145)$$

Accordingly, the total force on the charge distribution can be written as

$$\mathbf{F}_{\text{single}} = \int_{-\infty}^{\infty} \rho_{\text{single}}(x) \mathbf{E}(x) \, dx, \tag{146}$$

and the orthogonality (133) will lead to

$$
\begin{aligned}
\int_{-\infty}^{\infty} \rho_{\text{single}}(x) \mathbf{E}(x) \, dx &= \sum_{n=-\infty}^{\infty} \frac{q}{\Delta x} \mathbf{E}_n \int_{-\infty}^{\infty} \text{sinc}\left(\pi\left(\frac{x}{\Delta x} - \frac{X}{\Delta x}\right)\right) \text{sinc}\left(\pi\left(\frac{x}{\Delta x} - n\right)\right) dx \\
&= \sum_{n=-\infty}^{\infty} \frac{q}{\Delta x} \mathbf{E}_n \, \text{sinc}\left(\pi\left(\frac{X}{\Delta x} - n\right)\right) \Delta x, \\
\therefore \mathbf{F}_{\text{single}} &= q\mathbf{E}(X). \tag{147}
\end{aligned}
$$

It means the numerical point charge, defined as Eq. (144), feels the same force as the actual point charge at X does. In fact, it is not coincident because the density of the actual charge is represented as $\rho(x) = q\delta(x - X)$, and it is reasonable that $\delta(x) = \text{sinc}(\pi x/\Delta x)/\Delta x$ when $\Delta x \to 0$.

5.2.2 Finite-order

Unfortunately, practical problems should consider finite-order CBS. In this case, Eq. (136) will be substituted to the previous equations;

$$
\begin{aligned}
\dot{f}(x) &\simeq \sum_{n=-\infty}^{\infty} \frac{\partial}{\partial x}\left[S_N\left(\frac{x}{\Delta x} - n\right)\right] f_n, \\
\dot{f}_n &\equiv \dot{f}(n\Delta x). \tag{148}
\end{aligned}
$$

For instance, it is easy to show that $S_2(x)$ yields $\ddot{f}_n$, written as

$$\ddot{f}_n \simeq \frac{f_{n+1} - 2f_n + f_{n-1}}{\Delta x^2}. \tag{149}$$

In the same way, the distributions of a point charge and an electric field can be approximated by

$$
\begin{aligned}
\rho_{\text{single}}(x) &\simeq \frac{q}{\Delta x} S_N\left(\frac{x}{\Delta x} - \frac{X}{\Delta x}\right), \\
\mathbf{E}(x) &\simeq \sum_{n=-\infty}^{\infty} S_N\left(\frac{x}{\Delta x} - n\right) \mathbf{E}_n. \tag{150}
\end{aligned}
$$

However, the above approximation can not ensure that

$$\int_{-\infty}^{\infty} \rho_{\text{single}}(x) \mathbf{E}(x) \, dx \stackrel{?}{\simeq} q\mathbf{E}(X), \tag{151}$$

because the orthogonality for $S_N(x)$ is not equal to Eq. (133), but given by

$$\frac{1}{\Delta x}\int_{-\infty}^{\infty} S_0\left(\frac{x}{\Delta x}-a\right) S_0\left(\frac{x}{\Delta x}-b\right) dx = \begin{cases} 1-|a-b| & (|a-b|\le 1),\\ 0 & (|a-b|>1), \end{cases}$$

$$\frac{1}{\Delta x}\int_{-\infty}^{\infty} S_0\left(\frac{x}{\Delta x}-a\right) S_1\left(\frac{x}{\Delta x}-b\right) dx = \begin{cases} 3/4-|a-b|^2 & (|a-b|\le 1/2),\\ (3-2|a-b|)^2/8 & (1/2<|a-b|\le 3/2),\\ 0 & (|a-b|>3/2), \end{cases}$$

$$\frac{1}{\Delta x}\int_{-\infty}^{\infty} S_1\left(\frac{x}{\Delta x}-a\right) S_1\left(\frac{x}{\Delta x}-b\right) dx = \begin{cases} 2/3-|a-b|^2+|a-b|^3/2 & (|a-b|\le 1),\\ (2-|a-b|)^3/6 & (1<|a-b|\le 2),\\ 0 & (|a-b|>2). \end{cases}$$

$$(152)$$

This result implies a necessity of another spline $s_{N,M}(x)$, which satisfies

$$\int_{-\infty}^{\infty} S_N\left(\frac{x}{\Delta x}-a\right) S_M\left(\frac{x}{\Delta x}-b\right) = s_{N,M}(a-b)\,\Delta x, \tag{153}$$

so that the integral of $\rho_{\text{single}}(x)\,\mathbf{E}(x)$ could be expressed as

$$\int_{-\infty}^{\infty} \rho_{\text{single}}(x)\,\mathbf{E}(x)\,dx \simeq \sum_{n=-\infty}^{\infty} s_{N,N}\left(\frac{X}{\Delta x}-n\right) q\mathbf{E}_n. \tag{154}$$

Note that $s_{\infty,\infty}(x)=S_\infty(x)$. Now we need to decide which equation is going to be $\mathbf{F}_{\text{single}}$:

$$\mathbf{F}_{\text{single}} \overset{?}{\simeq} \sum_{n=-\infty}^{\infty} S_N\left(\frac{X}{\Delta x}-n\right) q\mathbf{E}_n, \tag{155}$$

$$\mathbf{F}_{\text{single}} \overset{?}{\simeq} \sum_{n=-\infty}^{\infty} s_{N,N}\left(\frac{X}{\Delta x}-n\right) q\mathbf{E}_n. \tag{156}$$

Unfortunately, it might not be clear to determine the finite-order force. Normally, Eq. (155) would be right as ρ_{single} (originally) represented the actual point charge. On the other hand, however, if ρ_{single} just represented a point-like volume charge, Eq. (156) could be more appropriate.

VI   Appendix: Dispersion relation of Raman scattering

In one-dimensional (1D) non-relativistic laser-plasma interactions, Lorentz force and Maxwell's equations can be written as

$$m_e n_e \frac{\partial \langle v_{xe} \rangle}{\partial t} + m_e n_e \langle v_{xe} \rangle \frac{\partial \langle v_{xe} \rangle}{\partial x} = -e n_e E_x - \frac{e^2 n_e}{2 m_e} \frac{\partial A_\perp^2}{\partial x} - 3 k_B T_e \frac{\partial n_e}{\partial x}, \qquad (157)$$

$$c^2 \frac{\partial^2 \mathbf{A}_\perp}{\partial x^2} - \frac{\partial^2 \mathbf{A}_\perp}{\partial t^2} = \frac{e^2 n_e}{m_e \epsilon_0} \mathbf{A}_\perp, \qquad (158)$$

$$\frac{\partial n_e}{\partial t} + \frac{\partial}{\partial x} \left(n_e \langle v_{xe} \rangle \right) = 0, \qquad (159)$$

where $\langle v_{xe} \rangle$ is the fluid velocity of electrons, and $\mathbf{A}_\perp \equiv A_y \hat{\mathbf{y}} + A_z \hat{\mathbf{z}}$. Suppose that each quantity is consist of constant and perturbed parts;

$$
\begin{aligned}
n_e &= n_0 + \delta n_e, \\
\langle v_{xe} \rangle &= \delta v_{xe}, \\
E_x &= \delta E_x, \\
T_e &= T_0 + \delta T_e,
\end{aligned}
\qquad (160)
$$

and the total electromagnetic (EM) wave includes laser and scattered waves ($\mathbf{A}_\perp = \mathbf{A}_L + \mathbf{A}_S$).

We also assume that EM waves are circularly polarized (CP), and represented as

$$
\begin{aligned}
\mathbf{A}_L &\simeq \frac{A_L}{2} \left(\hat{\mathbf{y}} + i\hat{\mathbf{z}} \right) \exp \left(i k_L x - i \omega_L t + i \phi_L \right) + \text{c.c.}, \\
\mathbf{A}_S &\simeq \frac{A_S}{2} \left(\hat{\mathbf{y}} + i\hat{\mathbf{z}} \right) \exp \left(i k_S x - i \omega_S t + i \phi_S \right) + \text{c.c.}.
\end{aligned}
\qquad (161)
$$

This limited assumption could yield general results, because CP waves are just linear combinations of linear polarized (LP) waves. By substituting Eqs. (160) and (161) with Eq. (158), we obtain

$$\left(-c^2 k_L^2 + \omega_L^2 \right) \mathbf{A}_L + \left(-c^2 k_S^2 + \omega_S^2 \right) \mathbf{A}_S \simeq \frac{e^2 \left(n_0 + \delta n_e \right)}{m_e \epsilon_0} \left(\mathbf{A}_L + \mathbf{A}_S \right). \qquad (162)$$

It is reasonable to assume $A_L \gg A_S$, and this dominance will leads to

$$
\begin{aligned}
\left(n_0 + \delta n_e \right) \left(\mathbf{A}_L + \mathbf{A}_S \right) &\simeq n_0 \mathbf{A}_L + n_0 \mathbf{A}_S + \delta n_e \mathbf{A}_L, \\
c^2 k_L^2 + \omega_{pe}^2 &\simeq \omega_L^2,
\end{aligned}
\qquad (163)
$$

where $\omega_{pe} \equiv \sqrt{e^2 n_0 / m_e \epsilon_0}$. According to Eq. (163), equation (165) can be rewritten as

$$\left(-c^2 k_S^2 + \omega_S^2 \right) \mathbf{A}_S \simeq \frac{e^2}{m_e \epsilon_0} \left(n_0 \mathbf{A}_S + \delta n_e \mathbf{A}_L \right), \qquad (164)$$

and by multiplying $\mathbf{A}_L$ to the above equation, we obtain

$$\left(\omega_S^2 - c^2 k_S^2 - \omega_{pe}^2 \right) \mathbf{A}_L \cdot \mathbf{A}_S \simeq \frac{e^2 A_L^2}{m_e \epsilon_0} \delta n_e. \qquad (165)$$

Furthermore, according to Eq. (160), equations (157) and (159) can be represented by

$$m_e n_0 \frac{\partial \delta v_{xe}}{\partial t} \simeq -en_0 \delta E_x - \frac{e^2 n_0}{m_e} \frac{\partial}{\partial x} \left(\mathbf{A}_L \cdot \mathbf{A}_S \right) - 3k_B T_0 \frac{\partial \delta n_e}{\partial x}, \tag{166}$$

$$0 \simeq \frac{\partial \delta n_e}{\partial t} + n_0 \frac{\partial \delta v_{xe}}{\partial x}, \tag{167}$$

because $|\mathbf{A}_L|^2$ and $|\mathbf{A}_S|^2$ are constant. If the positive ion density is assumed $n_i \simeq n_0$, Gauss's law is given by

$$\frac{\partial \delta E_x}{\partial x} \simeq -\frac{e \delta n_e}{\epsilon_0}, \tag{168}$$

and Eqs. (166)–(168) yield

$$\frac{3k_B T_0}{m_e} \frac{\partial^2 \delta n_e}{\partial x^2} - \frac{\partial^2 \delta n_e}{\partial t^2} - \omega_{pe}^2 \delta n_e \simeq -\frac{\omega_{pe}^2 \epsilon_0}{m_e} \frac{\partial^2}{\partial x^2} \left(\mathbf{A}_L \cdot \mathbf{A}_S \right). \tag{169}$$

As we assumed Eq. (161), the inner product $\mathbf{A}_L \cdot \mathbf{A}_S$ satisfies

$$\mathbf{A}_L \cdot \mathbf{A}_S \simeq \frac{A_L A_S}{2} \exp \left(i \left(k_L - k_S \right) x - i \left(\omega_L - \omega_S \right) t + i\phi_L - i\phi_S \right) + \text{c.c.}, \tag{170}$$

and by substituting Eqs. (165) and (170) with Eq. (169) we obtain

$$\left[-\frac{3k_B T_0}{m_e} \left(k_L - k_S \right)^2 + \left(\omega_L - \omega_S \right)^2 - \omega_{pe}^2 \right] \delta n_e \simeq \frac{\omega_{pe}^2 \epsilon_0}{m_e} \left(k_L - k_S \right)^2 \mathbf{A}_L \cdot \mathbf{A}_S$$

$$\simeq \frac{e^2 A_L^2}{m_e^2} \frac{\omega_{pe}^2 \left(k_L - k_S \right)^2}{\omega_S^2 - c^2 k_S^2 - \omega_{pe}^2} \delta n_e. \tag{171}$$

Finally, owing to Eq. (163), the dispersion relation between ω_S and k_S can be given as

$$\left(\omega_L - \omega_S \right)^2 - 3\beta_{\text{th}}^2 \left(\sqrt{\omega_L^2 - \omega_{pe}^2} - ck_S \right)^2 - \omega_{pe}^2 \simeq a_L^2 \frac{\omega_{pe}^2 \left(\sqrt{\omega_L^2 - \omega_{pe}^2} - ck_S \right)^2}{\omega_S^2 - c^2 k_S^2 - \omega_{pe}^2}, \tag{172}$$

where $\beta_{\text{th}} \equiv \sqrt{k_B T_0 / m_e c^2}$ and $a_L \equiv eA_L / m_e c$. Equation (172) is exactly equal to Eq. (7.21) of William's book except for a_L (due to the polarization).

6.1 Scattered waves in cold plasmas

Now we will suppose cold plasmas, which change Eq. (172) to

$$\left[\left(W_L - W_S \right)^2 - 1 \right] \left(W_S^2 - K_S^2 - 1 \right) = a_L^2 \left(\sqrt{W_L^2 - 1} - K_S \right)^2, \tag{173}$$

where $W \equiv \omega / \omega_{pe}$ and $K \equiv ck / \omega_{pe}$. Note that we used the equality sign for later approximations. Figure 11 shows Eq. (173) when $W_L = 4$ and $a_L = 0.25$. Interestingly, it has complex solutions when $-4 \lesssim K_S \lesssim -2$ and $2.5 \lesssim K_S \lesssim 3$ (Fig. 12). The imaginary part of W_S yields the growth wave due to Eq. (161). Therefore, the complex solutions represent Raman scattered waves.
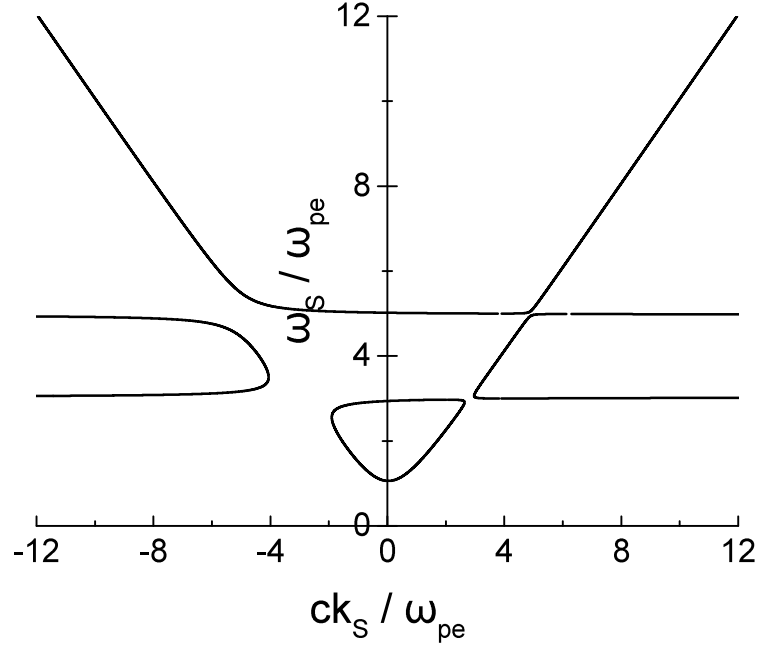
Figure 11: Equation (173) when $W_L = 4$ and $a_L = 0.25$. Note that the wavenumber K_S become infinity when $W_S = W_L \mp \sqrt{1 - a_L^2}$.

In order to derive the complex solutions, the real and imaginary parts of W_S need to be defined;

$$W_S = W_r + iW_i. \tag{174}$$

Accordingly, equation (173) will become

$$\left(W_r^2 - W_i^2 - K_S^2 - 1 \right) \left((W_L - W_r)^2 - W_i^2 - 1 \right) + 4W_r W_i^2 \left(W_L - W_r \right)$$
$$+ 2iW_i \left[W_r \left((W_L - W_r)^2 - W_i^2 - 1 \right) - (W_L - W_r) \left(W_r^2 - W_i^2 - K_S^2 - 1 \right) \right]$$
$$= a_L^2 \left(\sqrt{W_L^2 - 1} - K_S \right)^2. \tag{175}$$

The terms with $2i$ must be zero because all symbols $(W_L, W_r, W_r, K_S, a_L)$ represent real numbers. Therefore, equation (173) will be rewritten as

$$\left(W_r^2 - W_i^2 - K_S^2 - 1 \right) \left((W_L - W_r)^2 - W_i^2 - 1 \right) + 4W_r W_i^2 \left(W_L - W_r \right)$$
$$= a_L^2 \left(\sqrt{W_L^2 - 1} - K_S \right)^2, \tag{176}$$

49
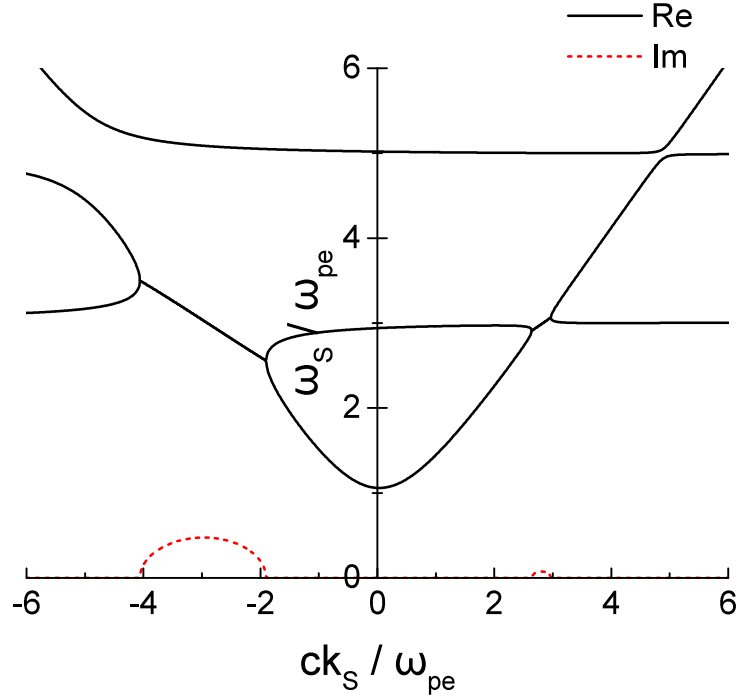
Figure 12: The complex solution of Eq. (173) when $W_L = 4$ and $a_L = 0.25$. The frequency W_S has the imaginary part when $-4 \lesssim K_S \lesssim -2$ and $2.5 \lesssim K_S \lesssim 3$.

and W_i satisfies

$$
W_i^2 = \begin{cases} 0 & (W_i^2 \leq 0), \\ \left[1 - (W_L - W_r)^2 + (W_L/W_r - 1)\left(W_r^2 - K_S^2 - 1\right)\right] / (W_L/W_r - 2) & (W_i^2 > 0). \end{cases}
\tag{177}
$$

Unfortunately, it is difficult to solve Eqs. (176) and (177) exactly. At least, however, we can find the intersection between Eq. (176) and $W_r^2 = K_S^2 + 1$ (Fig. 13). Note that we only consider the negative K_S even though there are two intersections. By substituting $W_r^2 = K_S^2 + 1$, equations (176)–(177) will be represented as

$$
W_r^3 \left(W_L - W_r\right) \frac{(W_L - W_r)^2 - 1}{W_r (W_L - 2W_r)} \left[\frac{(W_L - W_r)^2 - 1}{W_r (W_L - 2W_r)} - 4\right] = a_L^2 \left(\sqrt{W_L^2 - 1} + \sqrt{W_r^2 - 1}\right)^2
\tag{178}
$$

and if we suppose that $W_r = W_L - C$, we obtain

$$
(W_L - C)^3 C \frac{C^2 - 1}{(W_L - C)(2C - W_L)} \left[\frac{C^2 - 1}{(W_L - C)(2C - W_L)} - 4\right]
$$
$$
= a_L^2 \left(\sqrt{W_L^2 - 1} + \sqrt{(W_L - C)^2 - 1}\right)^2
\tag{179}
$$

50
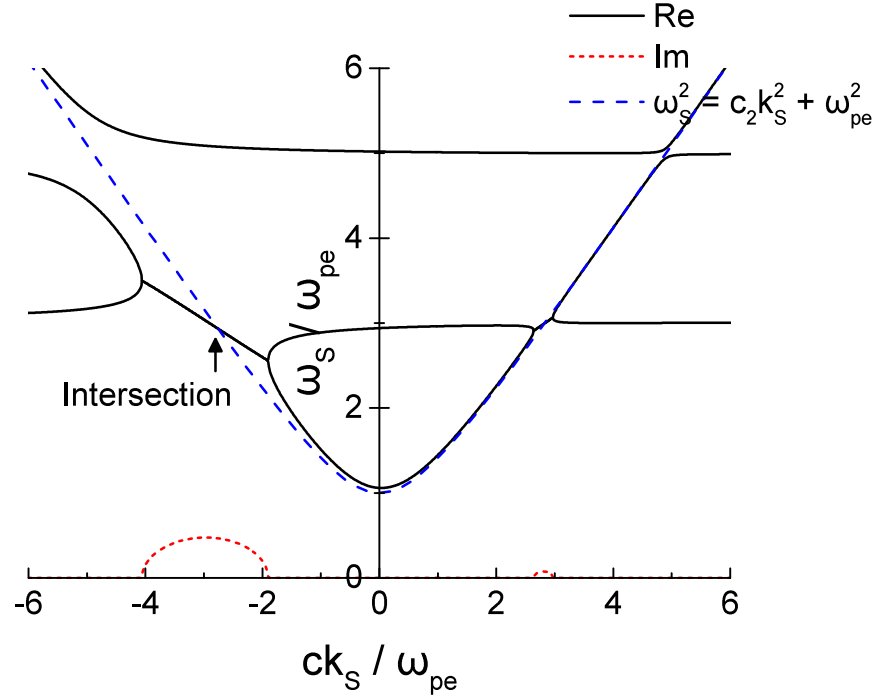
Figure 13: Dispersion relations of scattered and ordinary waves. There are intersection points which have the imaginary part.

Fortunately, assuming $W_L \gg 1$ can yield

$$C\left(C^2 - 1\right) \;\simeq\; a_L^2 W_L, \tag{180}$$

which leads to

$$C \approx \sqrt{1 + a_L^2 W_L}, \tag{181}$$

because in non-relativistic regime we can assume $a_L \ll 1$ (actually it requires $a_L^2 W_L \ll 1$). Therefore, when $W_r \approx W_L - \sqrt{1 + a_L^2 W_L}$, it satisfies $W_r^2 \approx K_S^2 + 1$. According to this result, now Eq. (177) can be written as

$$
\begin{aligned}
W_i^2\big|_{W_r^2 \approx K_S^2 + 1} &\approx \frac{W_L - \sqrt{1 + a_L^2 W_L}}{W_L - 2\sqrt{1 + a_L^2 W_L}} a_L^2 W_L \\
&\sim a_L^2 W_L.
\end{aligned}
\tag{182}
$$

Therefore, the growth rate γ will be given by

$$\gamma \sim a_L \sqrt{\omega_{pe}\omega_L}. \tag{183}$$

51

6.1.1 Group velocities of scattered waves

Interestingly, figure 13 shows the group velocity of the scattered wave is much smaller than the speed of light. It could be fatal for the amplification because the velocity of the seed pulse is approximately c.

As we assumed $a_L \ll 1$, equation (176) can be approximated as

$$\left(W_r^2 - W_i^2 - K_S^2 - 1\right)\left((W_L - W_r)^2 - W_i^2 - 1\right) + 4W_r W_i^2 \left(W_L - W_r\right) \quad \simeq \quad 0, \quad (184)$$

and Eqs. (177) and (184) yield

$$W_r \simeq \begin{cases} \left(\sqrt{1 + K_S^2} + W_L - 1\right)/2 & \left(K_S^2 \le W_L^2 + 2W_L\right) \\ W_L & \left(K_S^2 > W_L^2 + 2W_L\right) \end{cases} \quad \left(W_i^2 > 0\right). \quad (185)$$

According to this solution, it is possible to know that $K_S \sim -\sqrt{W_L^2 - 2W_L}$ when $W_r \approx W_L - \sqrt{1 + a_L^2 W_L} \sim W_L - 1$. By considering this results, the derivative of W_r can be given by

$$\frac{\partial W_r}{\partial K_S} \quad \simeq \quad \frac{1}{2}\frac{K_S}{\sqrt{1 + K_S^2}},$$

$$\left.\frac{\partial W_r}{\partial K_S}\right|_{W_r \sim W_L - 1} \quad \sim \quad \frac{1}{2}\frac{\sqrt{W_L^2 - 2W_L}}{W_L - 1}. \quad (186)$$

Therefore, we can conclude that the group velocity of the scattered wave is $0.5c$ when $W_L \gg 1$ [65].

VII Appendix: Maxwell equation in non-inertial frames

7.1 Chain rule

As we suppose that $\mathrm{d}\bar{r}^2 - \bar{c}^2\mathrm{d}\bar{t}^2 = \mathrm{d}r^2 - c^2\mathrm{d}t^2$ is the axiom-like condition [66], the Lorentz boost will be given by

$$
\begin{bmatrix} \bar{c}\mathrm{d}\bar{t} \\ \mathrm{d}\bar{x} \\ \mathrm{d}\bar{y} \\ \mathrm{d}\bar{z} \end{bmatrix}
=
\begin{bmatrix} \Gamma & 0 & 0 & -\Gamma V/c \\ 0 & 1 & 0 & 0 \\ 0 & 0 & 1 & 0 \\ -\Gamma V/c & 0 & 0 & \Gamma \end{bmatrix}
\begin{bmatrix} c\mathrm{d}t \\ \mathrm{d}x \\ \mathrm{d}y \\ \mathrm{d}z \end{bmatrix}.
\tag{187}
$$

Therefore, as the chain rule for the spacetime satisfies

$$
\mathrm{d}t\frac{\partial}{\partial t} + \mathrm{d}x\frac{\partial}{\partial x} + \mathrm{d}y\frac{\partial}{\partial y} + \mathrm{d}z\frac{\partial}{\partial z} = \mathrm{d}\bar{t}\frac{\partial}{\partial \bar{t}} + \mathrm{d}\bar{x}\frac{\partial}{\partial \bar{x}} + \mathrm{d}\bar{y}\frac{\partial}{\partial \bar{y}} + \mathrm{d}\bar{z}\frac{\partial}{\partial \bar{z}},
\tag{188}
$$

the transform for ∂^μ is also given by

$$
\begin{bmatrix} \dfrac{1}{\bar{c}}\dfrac{\partial}{\partial \bar{t}} \\ \dfrac{\partial}{\partial \bar{z}} \end{bmatrix}
=
\begin{bmatrix} \Gamma & \Gamma\dfrac{V}{c} \\ \Gamma\dfrac{V}{c} & \Gamma \end{bmatrix}
\begin{bmatrix} \dfrac{1}{c}\dfrac{\partial}{\partial t} \\ \dfrac{\partial}{\partial z} \end{bmatrix},
$$

$$
\begin{bmatrix} \dfrac{1}{c}\dfrac{\partial}{\partial t} \\ \dfrac{\partial}{\partial z} \end{bmatrix}
=
\begin{bmatrix} \Gamma & -\Gamma\dfrac{V}{c} \\ -\Gamma\dfrac{V}{c} & \Gamma \end{bmatrix}
\begin{bmatrix} \dfrac{1}{\bar{c}}\dfrac{\partial}{\partial \bar{t}} \\ \dfrac{\partial}{\partial \bar{z}} \end{bmatrix}.
\tag{189}
$$

Note that V also satisfies

$$
\begin{aligned}
\frac{\partial V}{\partial \bar{t}} &= \frac{c}{\Gamma^2}\frac{\partial \bar{c}}{\partial \bar{z}}, \\
\frac{\partial V}{\partial \bar{z}} &= 0.
\end{aligned}
\tag{190}
$$

7.1.1 Continuity equation

Another axiom would be that the number of total particles must be conserved, which leads to

$$
\frac{\partial \rho}{\partial t} + \frac{\partial J_x}{\partial x} + \frac{\partial J_y}{\partial y} + \frac{\partial J_z}{\partial z} = 0.
\tag{191}
$$

by substituting Eqs. (189) and (190), we can obtain

$$
\frac{\partial}{\partial \bar{t}}\left(\Gamma\rho - \Gamma\frac{V}{c}\frac{J_z}{c}\right) + \frac{\partial}{\partial \bar{x}}\left(\frac{J_x}{c}\bar{c}\right) + \frac{\partial}{\partial \bar{y}}\left(\frac{J_y}{c}\bar{c}\right) + \frac{\partial}{\partial \bar{z}}\left(\Gamma\frac{J_z}{c}\bar{c} - \Gamma\frac{V}{c}\rho\bar{c}\right) = 0.
\tag{192}
$$

Accordingly, we **defined** $\bar{j}^\mu$ as

$$
\begin{bmatrix} \bar{\rho} \\ \bar{J}_x/\bar{c} \\ \bar{J}_y/\bar{c} \\ \bar{J}_z/\bar{c} \end{bmatrix}
\equiv
\begin{bmatrix} \Gamma & 0 & 0 & -\Gamma V/c \\ 0 & 1 & 0 & 0 \\ 0 & 0 & 1 & 0 \\ -\Gamma V/c & 0 & 0 & \Gamma \end{bmatrix}
\begin{bmatrix} \rho \\ J_x/c \\ J_y/c \\ J_z/c \end{bmatrix},
\tag{193}
$$

so that the continuity equation in non-inertial frames could be given by

$$
\frac{\partial \bar{\rho}}{\partial \bar{t}} + \frac{\partial \bar{J}_x}{\partial \bar{x}} + \frac{\partial \bar{J}_y}{\partial \bar{y}} + \frac{\partial \bar{J}_z}{\partial \bar{z}} = 0.
\tag{194}
$$

7.1.2 Homogeneous Maxwell equation

The homogeneous Maxwell equation is given by

$$
\begin{aligned}
\frac{\partial B_x}{\partial x} + \frac{\partial B_y}{\partial y} + \frac{\partial B_z}{\partial z} &= 0, \\
\frac{\partial B_x}{\partial t} + \frac{\partial E_z}{\partial y} - \frac{\partial E_y}{\partial z} &= 0, \\
\frac{\partial B_y}{\partial t} - \frac{\partial E_z}{\partial x} + \frac{\partial E_x}{\partial z} &= 0, \\
\frac{\partial B_z}{\partial t} + \frac{\partial E_y}{\partial x} - \frac{\partial E_x}{\partial y} &= 0.
\end{aligned} \tag{195}
$$

By substituting Eq. (189), we obtain

$$
\begin{aligned}
-\Gamma\frac{V}{c}\frac{1}{\bar{c}}\frac{\partial B_z}{\partial \bar{t}} + \frac{\partial B_x}{\partial \bar{x}} + \frac{\partial B_y}{\partial \bar{y}} + \Gamma\frac{\partial B_z}{\partial \bar{z}} &= 0, \\
\Gamma\frac{c}{\bar{c}}\frac{\partial B_x}{\partial \bar{t}} + \Gamma\frac{V}{c}\frac{1}{\bar{c}}\frac{\partial E_y}{\partial \bar{t}} + \frac{\partial E_z}{\partial \bar{y}} - \Gamma\frac{\partial E_y}{\partial \bar{z}} - \Gamma V\frac{\partial B_x}{\partial \bar{z}} &= 0, \\
\Gamma\frac{c}{\bar{c}}\frac{\partial B_y}{\partial \bar{t}} - \Gamma\frac{V}{c}\frac{1}{\bar{c}}\frac{\partial E_x}{\partial \bar{z}} - \frac{\partial E_z}{\partial \bar{x}} + \Gamma\frac{\partial E_x}{\partial \bar{z}} - \Gamma V\frac{\partial B_y}{\partial \bar{z}} &= 0, \\
\Gamma\frac{c}{\bar{c}}\frac{\partial B_z}{\partial \bar{t}} + \frac{\partial E_y}{\partial \bar{x}} - \frac{\partial E_x}{\partial \bar{y}} - \Gamma V\frac{\partial B_z}{\partial \bar{z}} &= 0.
\end{aligned} \tag{196}
$$

According to Eq. (190), the above equations can be rewritten as

$$
\begin{aligned}
\frac{\partial}{\partial \bar{x}}\left(\Gamma B_x + \Gamma\frac{V}{c}\frac{E_y}{c}\right) + \frac{\partial}{\partial \bar{y}}\left(\Gamma B_y - \Gamma\frac{V}{c}\frac{E_x}{c}\right) + \frac{\partial B_z}{\partial \bar{z}} &= 0, \\
\frac{\partial}{\partial \bar{t}}\left(\Gamma B_x + \Gamma\frac{V}{c}\frac{E_y}{c}\right) + \frac{\partial}{\partial \bar{y}}\left(\frac{E_z}{c}\bar{c}\right) - \frac{\partial}{\partial \bar{z}}\left(\Gamma\frac{E_y}{c}\bar{c} + \Gamma\frac{V}{c}B_x\bar{c}\right) &= 0, \\
\frac{\partial}{\partial \bar{t}}\left(\Gamma B_y - \Gamma\frac{V}{c}\frac{E_x}{c}\right) - \frac{\partial}{\partial \bar{x}}\left(\frac{E_z}{c}\bar{c}\right) + \frac{\partial}{\partial \bar{z}}\left(\Gamma\frac{E_x}{c}\bar{c} - \Gamma\frac{V}{c}B_y\bar{c}\right) &= 0, \\
\frac{\partial B_z}{\partial \bar{t}} + \frac{\partial}{\partial \bar{x}}\left(\Gamma\frac{E_y}{c}\bar{c} + \Gamma\frac{V}{c}B_x\bar{c}\right) - \frac{\partial}{\partial \bar{y}}\left(\Gamma\frac{E_x}{c}\bar{c} - \Gamma\frac{V}{c}B_y\bar{c}\right) &= 0.
\end{aligned} \tag{197}
$$

Therefore, we **defined** $\bar{F}^{\mu\nu}$ as

$$
\begin{aligned}
\frac{\bar{E}_x}{\bar{c}} &\equiv \Gamma\frac{E_x}{c} - \Gamma\frac{V}{c}B_y, \quad \frac{\bar{E}_y}{\bar{c}} \equiv \Gamma\frac{E_y}{c} + \Gamma\frac{V}{c}B_x, \quad \frac{\bar{E}_z}{\bar{c}} \equiv \frac{E_z}{c}, \\
\bar{B}_x &\equiv \Gamma B_x + \Gamma\frac{V}{c}\frac{E_y}{c}, \quad \bar{B}_y \equiv \Gamma B_y - \Gamma\frac{V}{c}\frac{E_x}{c}, \quad \bar{B}_z \equiv B_z,
\end{aligned} \tag{198}
$$

so that the homogeneous equation in the non-inertial frame could be given by

$$
\begin{aligned}
\bar{\boldsymbol{\nabla}} \cdot \bar{\mathbf{B}} &= 0, \\
\bar{\boldsymbol{\nabla}} \times \bar{\mathbf{E}} &= -\frac{\partial \bar{\mathbf{B}}}{\partial \bar{t}},
\end{aligned} \tag{199}
$$

which also satisfy

$$
\begin{aligned}
\bar{\mathbf{E}} &= -\bar{\boldsymbol{\nabla}}\bar{\Phi} - \frac{\partial \bar{\mathbf{A}}}{\partial \bar{t}}, \\
\bar{\mathbf{B}} &= \bar{\boldsymbol{\nabla}} \times \bar{\mathbf{A}}.
\end{aligned} \tag{200}
$$

7.1.3 Inhomogeneous Maxwell equation

The inhomogeneous Maxwell equation is given by

$$
\begin{aligned}
\frac{\partial E_x}{\partial x} + \frac{\partial E_y}{\partial y} + \frac{\partial E_z}{\partial z} &= \frac{\rho}{\epsilon_0}, \\
-\frac{1}{c}\frac{\partial E_x}{\partial t} + \frac{\partial cB_z}{\partial y} - \frac{\partial cB_y}{\partial z} &= \frac{J_x}{\epsilon_0 c}, \\
-\frac{1}{c}\frac{\partial E_y}{\partial t} - \frac{\partial cB_z}{\partial x} + \frac{\partial cB_x}{\partial z} &= \frac{J_y}{\epsilon_0 c}, \\
-\frac{1}{c}\frac{\partial E_z}{\partial t} + \frac{\partial cB_y}{\partial x} - \frac{\partial cB_x}{\partial y} &= \frac{J_z}{\epsilon_0 c}.
\end{aligned}
\tag{201}
$$

In the similar way including Eq. (193), we obtain

$$
\begin{aligned}
-\Gamma\frac{V}{c}\frac{1}{\bar{c}}\frac{\partial E_z}{\partial \bar{t}} + \frac{\partial E_x}{\partial \bar{x}} + \frac{\partial E_y}{\partial \bar{y}} + \Gamma\frac{\partial E_z}{\partial \bar{z}} &= \frac{1}{\epsilon_0}\left(\Gamma\bar{\rho} + \Gamma\frac{V}{c}\frac{\bar{J}_z}{\bar{c}}\right), \\
-\frac{\Gamma}{\bar{c}}\frac{\partial E_x}{\partial \bar{t}} + \Gamma\frac{V}{c}\frac{1}{\bar{c}}\frac{\partial cB_y}{\partial \bar{t}} + \frac{\partial cB_z}{\partial \bar{y}} - \Gamma\frac{\partial cB_y}{\partial \bar{z}} + \Gamma\frac{V}{c}\frac{\partial E_x}{\partial \bar{z}} &= \frac{\bar{J}_x}{\epsilon_0 \bar{c}}, \\
-\frac{\Gamma}{\bar{c}}\frac{\partial E_y}{\partial \bar{t}} - \Gamma\frac{V}{c}\frac{1}{\bar{c}}\frac{\partial cB_x}{\partial \bar{t}} - \frac{\partial cB_z}{\partial \bar{x}} + \Gamma\frac{\partial cB_x}{\partial \bar{z}} + \Gamma\frac{V}{c}\frac{\partial E_y}{\partial \bar{z}} &= \frac{\bar{J}_y}{\epsilon_0 \bar{c}}, \\
-\frac{\Gamma}{\bar{c}}\frac{\partial E_z}{\partial \bar{t}} + \frac{\partial cB_y}{\partial \bar{x}} - \frac{\partial cB_x}{\partial \bar{y}} + \Gamma\frac{V}{c}\frac{\partial E_z}{\partial \bar{z}} &= \frac{1}{\epsilon_0}\left(\Gamma\frac{\bar{J}_z}{\bar{c}} + \Gamma\frac{V}{c}\bar{\rho}\right),
\end{aligned}
\tag{202}
$$

which can be also rewritten as

$$
\begin{aligned}
\frac{\partial}{\partial \bar{x}}\left(\Gamma\frac{E_x}{c} - \Gamma\frac{V}{c}B_y\right) + \frac{\partial}{\partial \bar{y}}\left(\Gamma\frac{E_y}{c} + \Gamma\frac{V}{c}B_x\right) + \frac{\partial}{\partial \bar{z}}\left(\frac{E_z}{c}\right) &= \frac{\bar{\rho}}{\epsilon_0 c}, \\
-\frac{\partial}{\partial \bar{t}}\left(\Gamma\frac{E_x}{c} - \Gamma\frac{V}{c}B_y\right) + \frac{\partial}{\partial \bar{y}}\left(B_z\bar{c}\right) - \frac{\partial}{\partial \bar{z}}\left(\Gamma B_y\bar{c} - \Gamma\frac{V}{c}\frac{E_x}{c}\bar{c}\right) &= \frac{\bar{J}_x}{\epsilon_0 c}, \\
-\frac{\partial}{\partial \bar{t}}\left(\Gamma\frac{E_y}{c} + \Gamma\frac{V}{c}B_x\right) - \frac{\partial}{\partial \bar{x}}\left(B_z\bar{c}\right) + \frac{\partial}{\partial \bar{z}}\left(\Gamma B_x\bar{c} + \Gamma\frac{V}{c}\frac{E_y}{c}\bar{c}\right) &= \frac{\bar{J}_y}{\epsilon_0 c}, \\
-\frac{\partial}{\partial \bar{t}}\left(\frac{E_z}{c}\right) + \frac{\partial}{\partial \bar{x}}\left(\Gamma B_y\bar{c} - \Gamma\frac{V}{c}\frac{E_x}{c}\bar{c}\right) - \frac{\partial}{\partial \bar{y}}\left(\Gamma B_x\bar{c} + \Gamma\frac{V}{c}\frac{E_y}{c}\bar{c}\right) &= \frac{\bar{J}_z}{\epsilon_0 c}.
\end{aligned}
\tag{203}
$$

Finally, by the definition (198), the inhomogeneous equation is represented as

$$
\begin{aligned}
\bar{\boldsymbol{\nabla}} \cdot \left(\frac{\bar{\mathbf{E}}}{\bar{c}}\right) &= \mu_0 c\bar{\rho}, \\
\bar{\boldsymbol{\nabla}} \times \left(\bar{c}\bar{\mathbf{B}}\right) &= \mu_0 c\bar{\mathbf{J}} + \frac{\partial}{\partial \bar{t}}\left(\frac{\bar{\mathbf{E}}}{\bar{c}}\right)
\end{aligned}
\tag{204}
$$

VIII   Appendix: Advanced Boris method

8.1   Lorentz's force

Lorentz force formula is given by

$$\frac{\mathrm{d}}{\mathrm{d}t}\left(m\gamma\mathbf{v}\right) \;=\; q\mathbf{E} + q\mathbf{v}\times\mathbf{B}, \tag{205}$$

where γ is Lorentz factor. By defining $\mathbf{u}\equiv\gamma\mathbf{v}$, This formula can be rewritten as

$$\frac{\mathrm{d}\mathbf{u}}{\mathrm{d}t} \;=\; \frac{q}{m}\mathbf{E} + \frac{q}{\gamma m}\mathbf{u}\times\mathbf{B}. \tag{206}$$

8.1.1   Boris's method

Numerically discretized Lorentz force would be given by

$$\frac{\mathbf{u}^{n+\frac{1}{2}}-\mathbf{u}^{n-\frac{1}{2}}}{\Delta t} \;\approx\; \frac{q}{m}\mathbf{E}^n + \frac{q}{\gamma^n m}\frac{\mathbf{u}^{n+\frac{1}{2}}+\mathbf{u}^{n-\frac{1}{2}}}{2}\times\mathbf{B}^n, \tag{207}$$

and its simplified expression can be

$$\frac{\mathbf{u}^+-\mathbf{u}^-}{\Delta t} \;\approx\; \frac{q}{2\gamma^n m}\left(\mathbf{u}^++\mathbf{u}^-\right)\times\mathbf{B}^n, \tag{208}$$

where $\mathbf{u}^+$ and $\mathbf{u}^-$ are defined as follows:

$$\begin{aligned}
\mathbf{u}^+ &\equiv \mathbf{u}^{n+\frac{1}{2}} - \frac{q\Delta t}{2m}\mathbf{E}^n, \\
\mathbf{u}^- &\equiv \mathbf{u}^{n-\frac{1}{2}} + \frac{q\Delta t}{2m}\mathbf{E}^n.
\end{aligned} \tag{209}$$

The final goal is to determine $\mathbf{u}^{n+\frac{1}{2}}$, which is equivalent to calculate $\mathbf{u}^+$. In order to this, Eq. (208) needs to be changed to

$$\left(|\mathbf{B}^n|^2 + \left|\frac{2\gamma^n m}{q\Delta t}\right|^2\right)\frac{\mathbf{u}^+-\mathbf{u}^-}{2} \;\approx\; \left(\frac{2\gamma^n m}{q\Delta t}\mathbf{u}^- + \mathbf{u}^-\times\mathbf{B}^n\right)\times\mathbf{B}^n, \tag{210}$$

so that $\mathbf{u}^+$ become a function of the given variables $(\mathbf{E}^n, \mathbf{B}^n, \gamma^n, \mathbf{u}^-)$.

8.1.2   Lorentz's factor

The remaining problem is how to calculate γ^n, which is defined as

$$\begin{aligned}
\gamma^n &\equiv \sqrt{1 + \frac{|\mathbf{u}^n|^2}{c^2}} \\
&\approx \left(1 + \frac{\left|\mathbf{u}^{n+\frac{1}{2}}+\mathbf{u}^{n-\frac{1}{2}}\right|^2}{4c^2}\right)^{1/2}.
\end{aligned} \tag{211}$$

By substituting Eq. (209) for this, we obtain

$$\gamma^n \quad \approx \quad \left(1 + \frac{|\mathbf{u}^+ + \mathbf{u}^-|^2}{4c^2} \right)^{1/2}. \tag{212}$$

As γ^n has $\mathbf{u}^+$ term, Eq. (210) is actually unsolvable now.

To solve this problem we multiplied $\mathbf{u}^+ + \mathbf{u}^-$ and Eq. (208), which yields

$$\frac{|\mathbf{u}^+|^2 - |\mathbf{u}^-|^2}{\Delta t} \quad \approx \quad 0. \tag{213}$$

This equation implies that the magnitudes of $\mathbf{u}^+$ and $\mathbf{u}^-$ are equivalent. Accordingly γ^n can be rewritten by

$$\gamma^n \quad \approx \quad \left(1 + \frac{|\mathbf{u}^-|^2 + \mathbf{u}^+ \cdot \mathbf{u}^-}{2c^2} \right)^{1/2}. \tag{214}$$

$\mathbf{u}^+ \cdot \mathbf{u}^-$ term could be replaced by multiplying $\mathbf{u}^-$ and Eq. (208);

$$\left(|\mathbf{B}^n|^2 + \left| \frac{2\gamma^n m}{q\Delta t} \right|^2 \right) \frac{\mathbf{u}^+ \cdot \mathbf{u}^- - |\mathbf{u}^-|^2}{2} \quad \approx \quad - |\mathbf{u}^-|^2 |\mathbf{B}^n|^2 + \left(\mathbf{u}^- \cdot \mathbf{B}^n \right)^2. \tag{215}$$

Eventually, by substituting Eq. (215) for Eq. (214), we obtain

$$\left(|\mathbf{B}^n|^2 + \left| \frac{2\gamma^n m}{q\Delta t} \right|^2 \right) \left(|\gamma^n|^2 - 1 - \frac{|\mathbf{u}^-|^2}{c^2} \right) + \frac{|\mathbf{u}^-|^2}{c^2} |\mathbf{B}^n|^2 - \left(\frac{\mathbf{u}^-}{c} \cdot \mathbf{B}^n \right)^2 \quad \approx \quad 0, \tag{216}$$

whose another expression is given by

$$\begin{aligned} 2|\gamma^n|^2 \quad = \quad & \left(1 + \frac{|\mathbf{u}^-|^2}{c^2} - \frac{q^2\Delta t^2}{4m^2} |\mathbf{B}^n|^2 \right) \\ & + \left[\left(1 + \frac{|\mathbf{u}^-|^2}{c^2} - \frac{q^2\Delta t^2}{4m^2} |\mathbf{B}^n|^2 \right)^2 + \frac{q^2\Delta t^2}{m^2} \left(|\mathbf{B}^n|^2 + \left(\frac{\mathbf{u}^-}{c} \cdot \mathbf{B}^n \right)^2 \right) \right]^{1/2}. \end{aligned} \tag{217}$$

Therefore, finally $\mathbf{u}^{n+\frac{1}{2}}$ become solvable by substituting Eq. (217) for Eq. (210). This result is expected to give much more accurate calculations than the conventional Boris method does [67–69]. Note that the old method assumes that

$$\gamma^n \quad = \quad \sqrt{1 + \frac{|\mathbf{u}^-|^2}{c^2}}. \tag{218}$$

IX Appendix: Lagrangian and radiation reaction

9.1 Lagrange mechanics in the electrodynamics

It is well-known that the Lagrangian of a point charge in electrodynamics is given by

$$L\left(\mathbf{r}, \mathbf{v}; t\right) = -\frac{mc^2}{\gamma} + q\mathbf{v} \cdot \mathbf{A} - q\Phi. \tag{219}$$

In this section, an equation of motion for a point charge is derived based on Eq. (219). Especially, how the radiation reaction can be involved in the obtained equation is deeply investigated.

9.2 Potential of a point charge

Mathematically, a point charge is defined as a volume charge whose distribution satisfies

$$\rho_{\mathrm{pt}}\left(\mathbf{r}, t\right) = q\delta^3\left(\mathbf{r} - \boldsymbol{\chi}\left(t\right)\right), \tag{220}$$

where $\delta^3\left(\mathbf{r}\right)$ is the Dirac-delta function, and $\boldsymbol{\chi}\left(t\right)$ is the position of point charge. In addition, for later derivation some quantities are defined as follows:

$$
\begin{aligned}
\mathbf{R}\left(\mathbf{r}, t\right) &\equiv \mathbf{r} - \boldsymbol{\chi}\left(t\right), \\
\mathbf{n}\left(\mathbf{r}, t\right) &\equiv \frac{\mathbf{R}\left(\mathbf{r}, t\right)}{R\left(\mathbf{r}, t\right)}, \\
\boldsymbol{\beta}\left(t\right) &\equiv \frac{1}{c}\frac{\mathrm{d}\boldsymbol{\chi}\left(t\right)}{\mathrm{d}t}, \\
\mathbf{a}\left(t\right) &\equiv \frac{\mathrm{d}^2\boldsymbol{\chi}\left(t\right)}{\mathrm{d}t^2}.
\end{aligned}
\tag{221}
$$

Retarded expressions for the above quantities also can be given by

$$
\begin{aligned}
t_r &\equiv t - \frac{R\left(\mathbf{r}, t_r\right)}{c}, \\
\mathbf{R}_r &\equiv \mathbf{R}\left(\mathbf{r}, t_r\right), \\
\mathbf{n}_r &\equiv \mathbf{n}\left(\mathbf{r}, t_r\right), \\
\boldsymbol{\beta}_r &\equiv \boldsymbol{\beta}\left(t_r\right), \\
\mathbf{a}_r &\equiv \mathbf{a}\left(t_r\right).
\end{aligned}
\tag{222}
$$

By these definitions, we obtain the electric field of point charge,

$$\mathbf{E}_{\mathrm{pt}}\left(\mathbf{r}, t\right) = \frac{q}{4\pi\epsilon_0}\frac{\mathbf{n}_r - \boldsymbol{\beta}_r}{R_r^2\gamma_r^2\left(1 - \mathbf{n}_r \cdot \boldsymbol{\beta}_r\right)^3} + \frac{q/c^2}{4\pi\epsilon_0}\frac{\mathbf{n}_r \times \left[\left(\mathbf{n}_r - \boldsymbol{\beta}_r\right) \times \mathbf{a}_r\right]}{R_r\left(1 - \mathbf{n}_r \cdot \boldsymbol{\beta}_r\right)^3}. \tag{223}$$

In particular, the first and second terms in the right side are called 'velocity' and 'acceleration' fields, which lead to the other definitions of new fields;

$$
\begin{aligned}
\mathbf{E}_v\left(\mathbf{r}, t\right) & \equiv \frac{q}{4\pi\epsilon_0} \frac{\mathbf{n}_r - \boldsymbol{\beta}_r}{R_r^2 \gamma_r^2 \left(1 - \mathbf{n}_r \cdot \boldsymbol{\beta}_r\right)^3}, \\
\mathbf{E}_a\left(\mathbf{r}, t\right) & \equiv \frac{q/c^2}{4\pi\epsilon_0} \frac{\mathbf{n}_r \times \left[\left(\mathbf{n}_r - \boldsymbol{\beta}_r\right) \times \mathbf{a}_r\right]}{R_r \left(1 - \mathbf{n}_r \cdot \boldsymbol{\beta}_r\right)^3}, \\
\mathbf{B}_v\left(\mathbf{r}, t\right) & \equiv \frac{\mathbf{n}_r}{c} \times \mathbf{E}_v\left(\mathbf{r}, t\right), \\
\mathbf{B}_a\left(\mathbf{r}, t\right) & \equiv \frac{\mathbf{n}_r}{c} \times \mathbf{E}_a\left(\mathbf{r}, t\right).
\end{aligned}
\tag{224}
$$

Furthermore, the potentials which can yield these fields are now required.

As expected, the most well-known gauge must be the Lorentz gauge, whose potentials are written by

$$
\begin{aligned}
\Phi_{\mathrm{LG}}\left(\mathbf{r}, t\right) & = \frac{q}{4\pi\epsilon_0} \frac{1}{R_r \left(1 - \mathbf{n}_r \cdot \boldsymbol{\beta}_r\right)}, \\
\mathbf{A}_{\mathrm{LG}}\left(\mathbf{r}, t\right) & = \frac{\boldsymbol{\beta}_r}{c} \Phi_{\mathrm{LG}}\left(\mathbf{r}, t\right).
\end{aligned}
\tag{225}
$$

However, these potentials are not divided between velocity and acceleration terms like Eq. (224) was. As the final goal is to investigate 'radiation' reaction in Lagrangian, the potentials also need to be divided. In this regard, I'd like to suggest new potentials,

$$
\begin{aligned}
\Phi_v\left(\mathbf{r}, t\right) & = \frac{q}{4\pi\epsilon_0} \frac{1}{R_r \gamma_r^2 \left(1 - \mathbf{n}_r \cdot \boldsymbol{\beta}_r\right)^2}, \\
\Phi_a\left(\mathbf{r}, t\right) & = \frac{q/c^2}{4\pi\epsilon_0} \left[\frac{\mathbf{n}_r \cdot \mathbf{a}_r}{\left(1 - \mathbf{n}_r \cdot \boldsymbol{\beta}_r\right)^2} - \frac{\gamma_r^2 \boldsymbol{\beta}_r \cdot \mathbf{a}_r}{\left(1 - \mathbf{n}_r \cdot \boldsymbol{\beta}_r\right)}\right], \\
\mathbf{A}_v\left(\mathbf{r}, t\right) & = \frac{\mathbf{n}_r}{c} \Phi_v\left(\mathbf{r}, t\right), \\
\mathbf{A}_a\left(\mathbf{r}, t\right) & = \frac{\mathbf{n}_r}{c} \Phi_a\left(\mathbf{r}, t\right),
\end{aligned}
\tag{226}
$$

whose gauge is undetermined yet. Interestingly, the new potentials satisfy $\mathbf{A}_{v,a} = \mathbf{n}_r \Phi_{v,a}/c$, while the Lorentz gauge yields $\mathbf{A}_{\mathrm{LG}} = \boldsymbol{\beta}_r \Phi_{\mathrm{LG}}/c$.

9.3 Energy conservation

Maxwell equation has a lot of its expressions, and the Lagrangian is closely connected to one of them,

$$
\epsilon_0 E^2 - \frac{B^2}{\mu_0} + \frac{\partial}{\partial t}\left(\epsilon_0 \mathbf{A} \cdot \mathbf{E}\right) + \boldsymbol{\nabla} \cdot \left(\epsilon_0 \Phi \mathbf{E} + \frac{\mathbf{A} \times \mathbf{B}}{\mu_0}\right) = \rho\Phi - \mathbf{J} \cdot \mathbf{A}.
\tag{227}
$$

It is a kind of continuity equation which is related to the conservation of something. This relation become much more visible if we consider only one point charge. For instance, by substituting $\mathbf{B}_{v,a} = \mathbf{n}_r \times \mathbf{E}_{v,a}/c$ and $\mathbf{A}_{v,a} = \mathbf{n}_r \Phi_{v,a}/c$ for Eq. (227), we obtain

$$
\epsilon_0 \left(\mathbf{n}_r \cdot \mathbf{E}_{\mathrm{pt}}\right)^2 + \frac{\epsilon_0}{c} \frac{\partial}{\partial t}\left[\Phi_{\mathrm{pt}}\left(\mathbf{n}_r \cdot \mathbf{E}_{\mathrm{pt}}\right)\right] + \epsilon_0 \boldsymbol{\nabla} \cdot \left[\mathbf{n}_r \Phi_{\mathrm{pt}}\left(\mathbf{n}_r \cdot \mathbf{E}_{\mathrm{pt}}\right)\right] = \rho_{\mathrm{pt}} \Phi_{\mathrm{pt}} - \mathbf{J}_{\mathrm{pt}} \cdot \mathbf{A}_{\mathrm{pt}}
\tag{228}
$$

where $\mathbf{E}_{\text{pt}} = \mathbf{E}_v + \mathbf{E}_a$ and $\Phi_{\text{pt}} = \Phi_v + \Phi_a$. If $c\mathbf{n}_r$ is considered as velocities of $\Phi_{\text{pt}}(\mathbf{n}_r \cdot \mathbf{E}_{\text{pt}})$, Eventually Eq. (228) become equivalent to the continuity equation. Moreover, regarding the self-potential, we could assume that

$$q\Phi_{\text{self}} - q\mathbf{v} \cdot \mathbf{A}_{\text{self}} \quad = \quad \int_{\mathcal{V}} (\rho_{\text{pt}}\Phi_{\text{pt}} - \mathbf{J}_{\text{pt}} \cdot \mathbf{A}_{\text{pt}}) \, \mathrm{d}^3 r. \tag{229}$$

Accordingly, as $\mathbf{n}_r \cdot \mathbf{E}_{\text{pt}} = \mathbf{n}_r \cdot \mathbf{E}_v$, Eq. (228) is rewritten by

$$\epsilon_0 \int_{\mathcal{V}} (\mathbf{n}_r \cdot \mathbf{E}_v)^2 \, \mathrm{d}^3 r + \frac{\epsilon_0}{c} \frac{\partial}{\partial t} \int_{\mathcal{V}} (\Phi_v + \Phi_a) (\mathbf{n}_r \cdot \mathbf{E}_v) \, \mathrm{d}^3 r + \epsilon_0 \oint_{\mathcal{S}} (\Phi_v + \Phi_a) (\mathbf{n}_r \cdot \mathbf{E}_v) \, \mathbf{n}_r \cdot \mathrm{d}\mathbf{S}$$

$$= q\Phi_{\text{self}} - q\mathbf{v} \cdot \mathbf{A}_{\text{self}}. \tag{230}$$

It shows the advantage of the new potentials; in Eq. (230), Φ_a is the only term affected by the acceleration (while the Lorentz gauge leaves more complicated $\mathbf{E}_a$).

9.4 Example: A reflected point charge

Suppose an extremely simple example about a point charge, whose motion satisfies $\boldsymbol{\chi}(t) = \beta c |t| \hat{\mathbf{z}}$. It means this charge is elastically collided at the location $\mathbf{r} = 0$ when $t = 0$. The solutions of potentials and fields for this motion can be given by

$$\mathbf{n}_r \cdot \mathbf{E}_v|_{\mathbf{r},t} \quad = \quad \frac{q}{4\pi\epsilon_0} \frac{1 - \beta^2}{(1 - \beta^2)(x^2 + y^2) + (z \mp \beta ct)^2},$$

$$\Phi_v(\mathbf{r}, t) \quad = \quad \frac{q}{4\pi\epsilon_0} \frac{\sqrt{(1 - \beta^2)(x^2 + y^2) + (z \mp \beta ct)^2} \pm \beta(z \mp \beta ct)}{(1 - \beta^2)(x^2 + y^2) + (z \mp \beta ct)^2},$$

$$\Phi_a(\mathbf{r}, t) \quad = \quad \frac{q}{4\pi\epsilon_0} \frac{2\beta \cos\theta}{1 \mp \beta \cos\theta} \delta(r - ct), \tag{231}$$

where $r < ct$ leads to the upper sign, while $r > ct$ leads to the bottom one. Apparently, these solutions is undefinable at $r = ct$. Moreover, in case of Φ_a, the coefficient of the Dirac-delta function has no value. However, sooner we will prove that these suspicious solutions can yield meaningful results.

9.4.1 Integration results

The third integral term of Eq. (230) can be easily vanished. According to Eq. (231), the potentials satisfy $\Phi_v(\mathbf{n}_r \cdot \mathbf{E}_v) \propto r^{-3}$ and $\Phi_a(\mathbf{n}_r \cdot \mathbf{E}_v) = 0$ where $r \gg ct$, so that the third term could be vanished;

$$\therefore \epsilon_0 \oint_{\mathcal{S}} (\Phi_v + \Phi_a) (\mathbf{n}_r \cdot \mathbf{E}_v) \, \mathbf{n}_r \cdot \mathrm{d}\mathbf{S} \quad = \quad 0. \tag{232}$$

On the other hands, solving the second integral term requires a little difficult skill. Suppose the Dirac-delta function can be written by

$$\delta(x) \quad = \quad \frac{1}{2} \frac{\partial}{\partial x} \left(\frac{x}{|x|} \right). \tag{233}$$

60

which eventually yields

$$\left(1 + \alpha \frac{x}{|x|}\right)^n \delta(x) = \begin{cases} \dfrac{(1+\alpha)^{n+1} - (1-\alpha)^{n+1}}{2\alpha(n+1)} \delta(x) & (n \neq -1) \\ \dfrac{1}{2\alpha} \ln\left(\dfrac{1+\alpha}{1-\alpha}\right) \delta(x) & (n = -1) \end{cases} \tag{234}$$

where α is an arbitrary constant. Owing to this, $\Phi_a \mathbf{n}_r \cdot \mathbf{E}_v$ of the second term will be rewritten by

$$
\begin{aligned}
(\Phi_a \mathbf{n}_r \cdot \mathbf{E}_v)|_{\mathbf{r},t} &= \left(\frac{q}{4\pi\epsilon_0}\right)^2 \frac{2\beta\cos\theta\left(1-\beta^2\right)}{r^2\left(1 \mp \beta\cos\theta\right)^3} \delta(r - ct) \\
&= \left(\frac{q}{4\pi\epsilon_0}\right)^2 \frac{2\beta\cos\theta\left(1-\beta^2\right)}{r^2} \left(1 + \beta\cos\theta \frac{r - ct}{|r - ct|}\right)^{-3} \delta(r - ct) \\
&= \left(\frac{q}{4\pi\epsilon_0}\right)^2 \frac{2\beta\cos\theta\left(1-\beta^2\right)}{r^2\left(1 - \beta^2\cos^2\theta\right)} \delta(r - ct),
\end{aligned} \tag{235}
$$

and its integration is

$$\therefore \frac{\epsilon_0}{c} \int_{\mathcal{V}} \Phi_a\left(\mathbf{n}_r \cdot \mathbf{E}_v\right) \mathrm{d}^3 r = 0. \tag{236}$$

Furthermore, $\Phi_v \mathbf{n}_r \cdot \mathbf{E}_v$ of the second term can be also vanished because of its symmetry as follows:

$$
\begin{aligned}
\int_{\mathcal{V}} (\Phi_v \mathbf{n}_r \cdot \mathbf{E}_v)|_{\mathbf{r},t}\, \mathrm{d}^3 r &= \iiint_{r<ct} (\Phi_v \mathbf{n}_r \cdot \mathbf{E}_v)|_{x,y,z,t}\, \mathrm{d}z\mathrm{d}y\mathrm{d}x + \iiint_{r>ct} (\Phi_v \mathbf{n}_r \cdot \mathbf{E}_v)|_{x,y,z,t}\, \mathrm{d}z\mathrm{d}y\mathrm{d}x \\
&= \iiint_{r<ct} (\Phi_v \mathbf{n}_r \cdot \mathbf{E}_v)|_{x,y,z,t}\, \mathrm{d}z\mathrm{d}y\mathrm{d}x + \iiint_{r>ct} (\Phi_v \mathbf{n}_r \cdot \mathbf{E}_v)|_{x,y,-z,t}\, \mathrm{d}z\mathrm{d}y\mathrm{d}x \\
&= \int_{\mathcal{V}} \left(\frac{q}{4\pi\epsilon_0}\right)^2 (1-\beta^2) \frac{\sqrt{(1-\beta^2)(x^2+y^2) + (z-\beta ct)^2} + \beta(z - \beta ct)}{\left[(1-\beta^2)(x^2+y^2) + (z-\beta ct)^2\right]^2} \mathrm{d}^3 r,
\end{aligned} \tag{237}
$$

and as the result is time-independent we obtain

$$\therefore \frac{\epsilon_0}{c} \frac{\partial}{\partial t} \int_{\mathcal{V}} \Phi_v\left(\mathbf{n}_r \cdot \mathbf{E}_v\right) \mathrm{d}^3 r = 0. \tag{238}$$

At last, Eq. (230) can be simplified by

$$\epsilon_0 \int_{\mathcal{V}} \left(\mathbf{n}_r \cdot \mathbf{E}_v\right)^2 \mathrm{d}^3 r = q\Phi_{\text{self}} - q\mathbf{v} \cdot \mathbf{A}_{\text{self}} \tag{239}$$

If we assume that R_0 is the radius of the particle, from Eq. (239) we will obtain

$$\frac{\mu_0 q^2}{4\pi R_0} \frac{c^2}{\gamma} = q\Phi_{\text{self}} - q\mathbf{v} \cdot \mathbf{A}_{\text{self}}, \tag{240}$$

which does not include any accelerations. Therefore, we can conclude that in the Lagrange mechanics the radiation reaction does not exist.

$$\therefore L(\mathbf{r}, \mathbf{v}; t) = -\frac{mc^2}{\gamma} + q\mathbf{v} \cdot \mathbf{A}_{\text{ext}} - q\Phi_{\text{ext}} - \frac{\mu_0 q^2}{4\pi R_0} \frac{c^2}{\gamma}. \tag{241}$$

X Conclusion

10.1 Envelope-PIC hybrid method for the simulation of microwave reflectometry

Microwave reflectometry, the plasma diagnostics method, uses reflected signal from cut-off layer to analyze density profile. The simulation study for this method usually solves wave equation assuming linear medium, however, extremely complex turbulent plasma couldn't be linear. Therefore we developed 2D hybrid code using PIC algorithm, which is widely used for nonlinear plasma study. This code solves PIC in high density region including cut-off layer, and paraxial approximation in the rest region. With this ways, we got the signal data, three times faster than pure PIC keeping the accuracy of PIC.

10.2 Unstable expansion of plasma foils accelerated by circularly-polarized laser pulses in non-transparent regimes

Relativistic opaqueness has been considered to be a sufficient condition for the stable compression and acceleration of a negligibly thin plasma foil by a circularly-polarized (CP) laser pulse. However, in our simulations, we observed that finite-thick plasma foils, which are still relativistically non-transparent to the laser pulse, can be subject to sudden and rapid expansion of the foil even when the pulse intensity is high enough to suppress the electrostatic Coulomb expansion. Analyzing the *distribution* of the ponderomotive force over the finite thickness of a slab-like foil, we found a theoretical condition to avoid the new expansion instability;

$$\frac{a_I}{\zeta_e} \leq \frac{1}{\sqrt{1 + k_L^2 l_e^2/4}}, \tag{242}$$

where l_e is the foil's thickness, which has been neglected in the conventional condition. Furthermore, relations between the new instability and the relativistic electron heating and self-induced transparency are discussed.

10.3 Radiation reaction from a constantly accelerating point-like rigid conductor

We present a very special charge distribution which is not only *rigid* in a constantly accelerating non-inertial frame, but also *conductive* so that the inside fields are vanished. Moreover, the most important characteristic of this distribution is that its outside fields are completely equal to the fields of *a point charge.* Therefore, we would like to define a material named 'point-like rigid conductor (PRC)' whose charge distribution satisfies the above conditions that we mentioned.

PRC can not be distinguished from the actual point charge even by extremely precise measurements (unless the inside can be observed). It means PRC would be the best alternative to investigate the dynamics of the ideal point charge. As we mentioned, in this document we are only interested in a constantly accelerating PRC.

10.3.1 Self-force of PRC

The radiation reaction is predicted to be included in the self-force of a charged particle. The self-force of the PRC can be obtained as follows:

$$
\begin{aligned}
\int \rho_{\text{prc}} \mathbf{E}_{\text{prc}} + \mathbf{J}_{\text{prc}} \times \mathbf{B}_{\text{prc}}\, \mathrm{d}^3 r &= -\frac{\mu_0 q^2}{6\pi R_0} \frac{c^2}{z_0} \sqrt{1 + \frac{R_0^2}{z_0^2}} \hat{\mathbf{z}} \\
&= -\frac{\mu_0 q^2}{6\pi R_0} \frac{\mathrm{d}\mathbf{u}}{\mathrm{d}t} \sqrt{1 + \left|\frac{\mathrm{d}\mathbf{u}}{\mathrm{d}t}\right|^2 \frac{R_0^2}{c^4}},
\end{aligned}
\tag{243}
$$

where $\mathbf{u} \equiv \mathrm{d}\boldsymbol{\chi}/\mathrm{d}\tau$, and τ is the proper time. As far as we know, this force has not been published yet. Probably it is because, most of researchers previously supposed that $R_0 \to 0$, before they calculate the self-force. In contrast, here we would like to suggest an interesting assumption, that R_0 might be quite longer than we thought;

$$
\begin{aligned}
\left|\frac{\mathrm{d}\mathbf{u}}{\mathrm{d}t}\right| \frac{R_0}{c^2} &\gg 1, \\
\rightarrow \int \rho_{\text{prc}} \mathbf{E}_{\text{prc}} + \mathbf{J}_{\text{prc}} \times \mathbf{B}_{\text{prc}}\, \mathrm{d}^3 r &= -\frac{\mu_0 q^2}{6\pi R_0} \frac{\mathrm{d}\mathbf{u}}{\mathrm{d}t} \left|\frac{\mathrm{d}\mathbf{u}}{\mathrm{d}t}\right| \frac{R_0}{c^2} \\
&= -\frac{\mu_0 q^2 \gamma^6 |\mathbf{a}|^2}{6\pi c^2} \hat{\mathbf{z}},
\end{aligned}
\tag{244}
$$

where $\gamma^2 = 1 + u^2/c^2$, and $\mathbf{a} = \mathrm{d}^2\boldsymbol{\chi}/\mathrm{d}t^2$. Surprisingly, the force became equivalent to Larmor formula. (Actually, this result can be also induced even when R_0 is infinitesimal, if the acceleration is high enough.) Definitely it implies that *the self-force of Eq. (243) includes the radiation reaction.*

References

[1] Y. Lin, R. Nazikian, J. H. Irby, and E. S. Marmar, "Plasma curvature effects on microwave reflectometry fluctuation measurements," *Plasma Phys. Controlled Fusion*, vol. 43, pp. L1–L8, 2001.

[2] F. Simonet, "Measurement of electron density profile by microwave reflectometry on tokamaks," *Plasma Phys. Controlled Fusion*, vol. 56, pp. 664–669, 1985.

[3] E. Mazzucato and R. Nazikian, "Microwave reflectometry for the study of density fluctuations in tokamak plasmas," *Plasma Phys. Controlled Fusion*, vol. 33, pp. 261–274, 1991.

[4] R. Nazikian, G. J. Kramer, and E. Valeo, "A tutorial on the basic principles of microwave reflectometry applied to fluctuation measurements in fusion plasmas," *Phys. Plasmas*, vol. 8, pp. 1840–1855, 2001.

[5] I. H. Hutchinson, "One-dimensional full-wave analysis of reflectometry sensitivity and correlations," *Plasma Phys. Controlled Fusion*, vol. 37, pp. 1225–1251, 1992.

[6] J. H. Irby, S. Horne, I. H. Hutchinson, and P. C. Stek, "2D full-wave simulation of ordinary mode reflectometry," *Plasma Phys. Controlled Fusion*, vol. 35, pp. 601–618, 1993.

[7] E. J. Valeo, G. J. Kramer, and R. Nazikian, "Two-dimensional simulations of correlation reflectometry in fusion plasmas," *Plasma Phys. Controlled Fusion*, vol. 44, pp. L1–L10, 2002.

[8] L. Shi, A. Diallo, G. Kramer, S.-H. Ku, W. Tang, and E. Valeo, "http://meetings.aps.org/link/BAPS.2014.DPP.GO3.6," *Bul. Am. Phys. Soc.*, 2014.

[9] T. Kang, K. B. Kwon, M. Cho, Y. Kim, M. S. Hur, H. K. Park, and W. Lee, "Envelope-PIC hybrid method for the simulation of microwave reflectometry," *IEEE Trans. Plasma Sci*, vol. 46, no. 3, pp. 577–582, 2018.

[10] K. S. Yee, "Numerical solution of initial boundary value problems involving Maxwell's equations in isotropic media," *IEEE Trans. Antennas Propagat.*, vol. 14, pp. 302–307, 1966.

[11] J. Villasenor and O. Buneman, "Rigorous charge conservation for local electromagnetic field solvers," *Comput. Phys. Commun.*, vol. 69, pp. 306–316, 1992.

[12] V. I. Veksler, "The principle of coherent acceleration of charged particles," *Sov. J. Atomic Energy*, vol. 2, p. 525, 1957.

[13] K. Landecker, "Possibility of frequency multiplication and wave amplification by means of some relativistic effects," *Phys. Rev.*, vol. 86, p. 852, 1952.

[14] U. Teubner and P. Gibbon, "High-order harmonics from laser-irradiated plasma surfaces," *Rev. Mod. Phys.*, vol. 81, p. 445, 2009.

[15] A. Macchi, M. Borghesi, and M. Passoni, "Ion acceleration by superintense laser-plasma interaction," *Rev. Mod. Phys.*, vol. 85, p. 751, 2013.

[16] V. Yu. Bychenkov, V. T. Tikhonchuk, and S. V. Tolokonnikov, "Nuclear reactions triggered by laser-accelerated high-energy ions," *Sov. Phys. JETP*, vol. 88, p. 1137, 1999.

[17] V. Yu. Bychenkov, Y. Sentoku, S. V. Bulanov, K. Mima, G. Mourou, and S. V. Tolokonnikov, "Pion production under the action of intense ultrashort laser pulse on a solid target," *JETP Lett.*, vol. 74, p. 586, 2001.

[18] A. M. Koehler, "Proton radiography," *Science*, vol. 160, p. 303, 1968.

[19] A. J. Mackinnon, P. K. Patel, R. P. Town, M. J. Edwards, T. Phillips, S. C. Lerner, D. W. Price, D. Hicks, M. H. Key, S. Hatchett, S. C. Wilks, M. Borghesi, L. Romagnani, S. Kar, T. Toncian, G. Pretzler, O. Willi, M. Koenig, E. Martinolli, S. Lepape, A. Benuzzi-Mounaix, P. Audebert, J. C. Gauthier, J. King, R. Snavely, R. R. Freeman, and T. Boehlly, "Proton radiography as an electromagnetic field and density perturbation diagnostic (invited)," *Rev. Sci. Instrum.*, vol. 75, p. 3531, 2004.

[20] S. V. Bulanov, T. Zh. Esirkepov, V. S. Khoroshkov, A. V. Kuznetsov, and F. Pehoraro, "Oncological hadrontherapy with laser ion accelerators," *Phys. Lett. A*, vol. 299, p. 240, 2002.

[21] H. Wabnitz, L. Bittner, A. R. B. de Castro, R. Döhrmann, P. Gürtler, T. Laarmann, W. Laasch, J. Schulz, A. Swiderski, K. von Haeften, T. Möller, B. Faatz, A. Fateev, J. feldhaus, C. Gerth, U. Hahn, E. Saldin, E. Schneidmiller, K. Sytchev, K. Tiedtke, R. Treusch, and M. Yurkov, "Multiple ionization of atom clusters by intense soft X-rays from a free-electron laser," *Nature (London)*, vol. 420, p. 482, 2002.

[22] S. A. Aseyev, Y. Ni, L. J. Frasinski, H. G. Muller, and M. J. J. Vrakking, "Attosecond angle-resolved photoelectron spectroscopy," *Phys. Rev. Lett.*, vol. 91, p. 223902, 2003.

[23] S. Dobosz, G. Doumy, H. Stabile, P. D'Oliveira, P. Monot, F. Réau, S. Hüller, and Ph. Martin, "Probing hot and dense laser-induced plasmas with ultrafast XUV pulses," *Phys. Rev. Lett.*, vol. 95, p. 025001, 2005.

[24] D. Strickland and G. Mourou, "Compression of amplified chirped optical pulses," *Opt. Coummun*, vol. 55, p. 447, 1985.

[25] M. D. Perry and G. Mourou, "Terawatt to petawatt subpicosecond lasers," *Science*, vol. 264, p. 917, 1994.

[26] G. A. Mourou, T. Tajima, and S. V. Bulanov, "Optics in the relativistic regime," *Rev. Mod. Phys.*, vol. 78, p. 309, 2006.

[27] V. Yanovsky, V. Shvykov, G. Kalinchenko, P. Rousseau, T. Planchon, T. Matsuoka, A. Maksimchuk, J. Nees, G. Cheriaux, G. Mourou, and K. Krushelnick, "Ultra-high intensity- 300-TW laser at 0.1 Hz repetition rate," *Opt. Express*, vol. 16, p. 2109, 2008.

[28] A. V. Korzhimanov, A. A. Gonoskov, E. A. Khazanov, and A. M. Sergeev, "Horizons of petawatt laser technology," *Phys. Usp.*, vol. 54, p. 9, 2011.

[29] A. Di Piazza, C. Müller, K. Z. Hatsagortsyan, and C. H. Keitel, "Extremely high-intensity laser interactions with fundamental quantum systems," *Rev. Mod. Phys.*, vol. 84, p. 1177, 2012.

[30] S. V. Bulanov, T. Esirkepov, and T. Tajima, "Light intensification towards the schwinger limit," *Phys. Rev. Lett.*, vol. 91, p. 085001, 2003.

[31] T. Esirkepov, M. Borghesi, S. V. Bulanov, G. Mourou, and T. Tajima, "Highly efficient relativistic-ion generation in the laser-piston regime," *Phys. Rev. Lett.*, vol. 92, p. 175003, 2004.

[32] Y.-K. Kim, M.-H. Cho, H. S. Song, T. Kang, H. J. Park, M. Y. Jung, and M. S. Hur, "Shock ion acceleration by an ultrashort circularly polarized laser pulse via relativistic transparency in an exploded target," *Phys. Rev. E*, vol. 92, p. 043102, 2015.

[33] D. N. Gupta, P. Yadav, D. G. Jang, M. S. Hur, H. Suk, and K. Avinash, "Onset of stimulated Raman scattering of a laser in a plasma in the presence of hot drifting electrons," *Phys. Plasmas*, vol. 22, p. 052101, 2015.

[34] X. Q. Yan, C. Lin, Z. M. Sheng, Z. Y. Guo, B. C. Liu, Y. R. Lu, J. X. Fang, and J. E. Chen, "Generating high-current monoenergetic proton beams by a circularly polarized laser pulse in the phase-stable acceleration regime," *Phys. Rev. Lett.*, vol. 100, p. 135003, 2008.

[35] L. Ji, B. Shen, X. Zhang, F. Wang, Z. Jin, M. Wen, W. Wang, and J. Xu, "Comment on "Generating high-current monoenergetic proton beams by a circularly polarized laser pulse in the phase-stable acceleration regime"," *Phys. Rev. Lett.*, vol. 102, p. 239501, 2009.

[36] V. A. Vshivkov, N. M. Naumova, F. Pegoraro, and S. V. Bulanov, "Nonlinear electrodynamics of the interaction of ultra-intense laser pulses with a thin foil," *Phys. Plasmas*, vol. 5, p. 2727, 1998.

[37] A. S. Pirozhkov, S. V. Bulanov, T. Zh. Esirkepov, M. Mori, A. Sagisaka, and H. Daido, "Attosecond pulse generation in the relativistic regime of the laser-foil interaction: The sliding mirror model," *Phys. Plasmas*, vol. 13, p. 013107, 2006.

[38] B. Qiao, M. Zepf, M. Borghesi, and M. Geissler, "Stable GeV ion-beam acceleration from thin foils by circularly polarized laser pulses," *Phys. Rev. Lett.*, vol. 102, p. 145002, 2009.

[39] A. Pukhov, "Strong field interaction of laser radiation," *Rep. Prog. Phys.*, vol. 66, p. 47, 2002.

[40] L. Yin, B. J. Albright, K. J. Bowers, D. Jung, J. C. Fernández, and B. M. Hegelich, "Three-dimensional dynamics of breakout afterburner ion acceleration using high-contrast short-pulse laser and nanoscale targets," *Phys. Rev. Lett.*, vol. 107, p. 045003, 2011.

[41] S. Palaniyappan, B. M. Hegelich, H.-C. Wu, D. Jung, D. C. Gautier, L. Yin, B. J. Albright, R. P. Johnson, T. Shimada, S. Letzring, D. T. Offermann, J. Ren, C. Huang, R. Hörlein, B. Dromey, J. C. Fernandez, and R. C. Shah, "Dynamics of relativistic transparency and optical shuttering in expanding overdense plasmas," *Nat. Phys.*, vol. 8, p. 763, 2012.

[42] S. Palaniyappan, C. Huang, D. C. Gautier, C. E. Hamilton, M. A. Santiago, C. Kreuzer, A. B. Sefkow, R. C. Shah, and J. C. Fernández, "Efficient quasi-monoenergetic ion beams from laser-driven relativistic plasmas," *Nat. Commun*, vol. 6, p. 10170, 2015.

[43] S. Steinke, P. Hilz, M. Schnürer, G.Priebe, J. Bränzel, F. Abicht, D. Kiefer, C. Kreuzer, T. Ostermayr, J. Schreiber, A. A. Andreev, T. P. Yu, A. Pukhov, and W. Sandner, "Stable laser-ion acceleration in the light sail regime," *Phys. Rev. ST Accel. Beams*, vol. 16, p. 011303, 2013.

[44] M. Schollmeier, A. B. Sefkow, M. Geissel, A. V. Arefiev, K. A. Flippo, S. A. Gaillard, R. P. Johnson, M. W. Kimmel, D. T. Offermann, P. K. Rambo, and J. Schwarz, "Laser-to-hot-electron conversion limitations in relativistic laser matter interactions due to multi-picosecond dynamics," *Phys. Plasmas*, vol. 22, p. 043116, 2015.

[45] A. V. Arefiev, A. P. L. Robinson, and V. N. Khudik, "Novel aspects of direct laser acceleration of relativistic electrons," *J. Plasma Phys.*, vol. 81, p. 475810404, 2015.

[46] A. I. Akhiezer and R. V. Polovin, "Theory of wave motion of an electron plasma," *Sov. Phys. JETP*, vol. 3, p. 696, 1956.

[47] P. Kaw and J. Dawson, "Relativistic nonlinear propagation of laser beams in cold overdense plasmas," *Phys. Fluids*, vol. 13, p. 472, 1970.

[48] C. S. Lai, "Strong transverse electromagnetic waves in overdense plasmas," *Phys. Rev. Lett.*, vol. 36, p. 966, 1976.

[49] A. Macchi, S. Veghini, T. V. Liseykina, and F. Pegoraro, "Radiation pressure acceleration of ultrathin foils," *New J. Phys.*, vol. 12, p. 045013, 2010.

[50] B. Eliasson, C. S. Liu, X. Shao, R. Z. Sagdeev, and P. K. Shukla, "Laser acceleration of monoenergetic protons via a double layer emerging from an ultra-thin foil," *New J. Phys.*, vol. 11, p. 073006, 2009.

[51] T. Kang, Y.-K. Kim, and M. S. Hur, "Unstable expansion of plasma foils accelerated by circularly-polarized laser pulses in non-transparent regimes," *Phys. Rev. E*, 2019, in press.

[52] J. H. Marburger and R. F. Tooper, "Nonlinear optical standing waves in overdense plasmas," *Phys. Rev. Lett.*, vol. 35, p. 1001, 1975.

[53] F. Cattani, A. Kim, D. Anderson, and M. Lisak, "Threshold of induced transparency in the relativistic interaction of an electromagnetic wave with overdense plasmas," *Phys. Rev. E*, vol. 62, p. 1234, 2000.

[54] V. V. Goloviznin and T. J. Schep, "Threshold of induced transparency in the relativistic interaction of an electromagnetic wave with overdense plasmas," *Phys. Plasmas*, vol. 7, p. 1564, 2000.

[55] W. Yu, Z. M. Sheng, M. Y. Yu, J. Zhang, Z. M. Jiang, and Z. Xu, "Model for transmission of ultrastrong laser pulses through thin foil targets," *Phys. Rev. E*, vol. 59, p. 3583, 1999.

[56] Y.-K. Kim, T. Kang, M. Y. Jung, and M. S. Hur, "Effects of laser polarizations on shock generation and shock ion acceleration in overdense plasmas," *Phys. Rev. E*, vol. 94, p. 033211, 2016.

[57] P. A. M. Dirac, "Classical theory of radiating electrons," *Proc. R. Soc. Lond. A.*, vol. 167, pp. 148–169, 1938.

[58] R. P. Feynman, "Relativistic cut-off for quantum electrodynamics," *Phys. Rev.*, vol. 74, pp. 1430–1438, 1948.

[59] D. A. Burton and A. Noble, "Aspects of electromagnetic radiation reaction in strong fields," *Contemp. Phys*, vol. 55, no. 2, pp. 110–121, 2014.

[60] A. M. Steane, "Self-force of a rigid ideal fluid, and a charged sphere in hyperbolic motion," *Phys. Rev. D*, vol. 91, p. 065008, 2015.

[61] E. Eriksen and Ø. Grøn, "Electrodynamics of hyperbolically accelerated charges V. the field of a charge in the Rindler space and the Milne space," *Ann. Phys*, vol. 313, no. 1, pp. 147–196, 2004.

[62] E. Eriksen and Ø. Grøn, "Electrodynamics of hyperbolically accelerated charges: I. the electromagnetic field of a charged particle with hyperbolic motion," *Ann. Phys*, vol. 286, no. 2, pp. 320–342, 2000.

[63] L. D. Landau and E. Lifshitz, *The Classical Theory of Fields.* Oxford: Elsevier, 1975.

[64] T. Fulton and F. Rohrlich, "Classical radiation from a uniformly accelerated charge," *Ann. Phys*, vol. 9, no. 4, pp. 499–517, 1960.

[65] V. M. Malkin, G. Shvets, and N. J. Fisch, "Ultra-powerful compact amplifiers for short laser pulses," *Phys. Plasmas*, vol. 7, no. 5, pp. 2232–2240, 2000.

[66] W. Rindler, "Kruskal space and the uniformly accelerated frame," *Am. J. Phys.*, vol. 34, no. 12, pp. 1174–1178, 1966.

[67] J. P. Boris, "Relativistic plasma simulation-optimization of a hybrid code," *Proceeding of Fourth Conference on Numerical Simulations of Plasmas*, pp. 3–67, 1970.

[68] J.-L. Vay, "Simulation of beams or plasmas crossing at relativistic velocity," *Phys. Plasmas*, vol. 15, no. 5, p. 056701, 2008.

[69] A. V. Higuera and J. R. Cary, "Structure-preserving second-order integration of relativistic charged particle trajectories in electromagnetic fields," *Phys. Plasmas*, vol. 24, no. 5, p. 052104, 2017.